Investigation of deposition-pressure-dependent photochromism, band gap tuning and photodarkening model for yttrium oxyhydride thin films

by

Jelle Stap

in partial fulfilment of the requirements for the degree of

Master of Science
in Materials Science and Engineering

at Delft University of Technology,
to be defended publicly on Monday 25 September 2017 at 9.30 am.

supervisors:	dr. S. Cornelius
	prof. dr. B. Dam
assessment committee:	dr. A. J. Böttger
	dr. S. Cornelius
	prof. dr. B. Dam
	dr. T. J. Savenije

This thesis is to remain confidential until 1 October 2018.

TU Delft

Abstract

Photochromic smart windows form a promising class of energy-saving technologies for the built environment. In recent years, sputter-deposited yttrium oxyhydride (YO_xH_y) coatings have been gaining attention due to their desirable photochromic properties such as colour-neutral darkening, high contrast, and apparent durability. For commercial application in smart windows several issues remain to be addressed, e.g their yellowish colour and bleaching time scales of the order of hours. Tailoring these photochromic properties is difficult because the mechanisms involved are largely unknown.

In this thesis, the influence of deposition pressure on photochromic contrast and film stability is linked to film microstructure to optimise the photochromic properties for smart window applications. Both contrast and stability are improved by obtaining a densest-possible microstructure. As a first step towards achieving colourless transparency, proof of concept is provided for the ability to tune the band gap by co-sputtering with dysprosium.

A metallic yttrium dihydride (YH_y) domain growth darkening model is introduced to describe the photochromic behaviour of YO_xH_y. The model appears to be consistent with observations on film porosity, contrast, kinetics, and irreversible darkening of YH_y. This might introduce possibilities to limiting bleaching times, as well as giving better insights into the photochromic mechanisms for YO_xH_y.

Contents

1 Introduction

In the widely acknowledged need to reduce our energy consumption due to limited resources and large environmental and societal risks associated with the use of fossil fuels in meeting ever increasing energy demands, vast savings are to be gained in the built environment, accounting for 30–40% of total energy consumption [1, 2]. Although the global share of the cooling of buildings in these figures is currently around 3.3%, this number is increasing rapidly—by the end of the century a rise in total residential energy consumption of up to 83% is projected due to air conditioning alone, mainly driven by global warming and increasing prosperity in unsaturated markets in developing countries with warm climates [2, 3].

A promising class of energy-saving technologies for the built environment have emerged in the form of chromogenic coatings for smart windows, i.e. coatings with switchable optical properties through interaction with their environment. The key characteristic of the energy-saving potential of such coatings is a reduction in transmittance of electromagnetic (EM) radiation from the sun, typically the main heat source in buildings requiring air conditioning [4].

Chromogenic materials for smart window applications can be categorised as *electro*chromic, *thermo*chromic, and *photo*chromic. Well known are electrochromic windows, which have adjustable optical properties by applying a voltage and thus allow for direct control of the desired appearance. They do however require an electrical input and some dynamic control system, increasing cost, complexity and energy demand. The optical properties of thermochromic materials are determined by temperature, and their operation is therefore limited to specific temperature ranges [5].

More promising in terms of energy-saving potential and simplicity (cost) are photochromic coatings, which exhibit a reversible transformation between two states with different optical properties upon absorption of EM radiation of sufficient energy. In practice this means that a photochromic smart window darkens upon sunlight exposure, passively reducing the amount of energy entering a building, and returning to its transparent state as the irradiation ceases. A wide range of photochromic materials exist, organic and inorganic, several of which have found commercial use such as in self-darkening sunglasses. Limitations in cost, strength, colour, kinetics, cyclability, durability, or dependency on ultraviolet (UV) radiation, however, have so far inhibited large-scale implementation in commercial smart windows [5, 6].

Over the past couple of years, thin films of rare earth oxyhydrides (REO_xH_ys) have been gaining attention as a novel class of photochromic coatings due to their desirable properties such as strong, colour-neutral darkening, sensitivity to visible light, and apparent durability [7]. It follows earlier work on comparable switchable optical transitions observed in yttrium and lanthanum hydrides at low temperature or high pressure, but with the major advantage of oxygen-containing films being stable at ambient conditions [8, 9, 10, 11].

X-ray diffraction (XRD), neutron reflectometry (NR) and Rutherford backscattering spectrometry (RBS) studies have shown that black metallic yttrium dihydride (YH_y) thin films reactively sputtered at sufficient deposition pressures oxidise in air to form semiconducting, yellowish transparent, photochromic yttrium oxyhydride (YO_xH_y), due to a sufficiently porous film microstructure [7, 12].

Illumination of YO_xH_y is characterised by strong absorption of blue/violet and UV radiation with photon energies above its band gap, leading to a reduction in transmittance of visible and near-infrared radiation which is reversed as the material is left in the dark [7, 12]. X-ray photoelectron spectroscopy (XPS) studies have revealed that this photochromic darkening is accompanied by a resistivity reduction and a slight lowering of the work function, implying photoexcitation of valence electrons across the band gap and subsequent trapping at deep donor defect levels [13]. Additionally, solid-state nuclear magnetic resonance (NMR) spectroscopy experiments show the presence of highly mobile hydrogen species in the vicinity of oxygen ions in YO_xH_y which disappear upon illumination, and it has been speculated that this might be related to the migration of hydrogen species away from oxygen to form YH_y clusters in the semiconducting matrix [14]. Moreover, XRD studies have shown that the photochromic effect is accompanied by a lattice contraction, possibly due to the formation of YH_y phases [15]. These suggestions are supported by Raman spectroscopy (RS) studies and effective medium approximations, showing that the formation of volume fractions of metallic YH_y phases is consistent with the observed darkening behaviour of the films [16].

Also attributed to thin films of YO_xH_y are some kind of *memory effect*—a second illumination cycle invokes faster darkening than the first [7, 17, 18], and *optical bleaching*—enhanced bleaching of darkened material by illumination with photon energies below the band gap [17, 18].

Similar structural, electronic, and photochromic properties have been reported for several other types of REO_xH_y thin films, with yttrium replaced by gadolinium, dysprosium, or erbium [17, 18, 19].

Photochromic YO_xH_y has a yellowish appearance due to its 2.6 eV band gap, absorbing higher energy blue and violet photons while transmitting the remaining part of the visible spectrum.

Although implementation of REO_xH_y thin films in photochromic smart windows is promising, there are several issues that need to be addressed, regarding their (yellowish) colour, darkening and bleaching times in the order of hours, and long-term uncertainties concerning cyclability and ageing. Altering these properties is difficult because the structural, electronic, and optical processes involved in the photochromic effect are largely unknown and additional research is therefore required. Better understanding of these mechanisms could also pave the way for potential application of photochromic REO_xH_ys in e.g. sunglasses, optical switches, or memory storage.

In this thesis, the effect of film growth conditions on the structural and optical characteristics of reactively sputtered YO_xH_y thin films is investigated using XRD and photospectrometry, to optimise the photochromic properties for smart window applications. Through variation of deposition pressures microstructural requirements for the spontaneous YH_y–YO_xH_y transition upon air exposure are established. Studies on the optical response to UV irradiance are conducted to link these morphological properties to photochromic performance, i.e. darkening potential under illumination. For film durability purposes, gains in UV transparency resulting from ageing are monitored to quantify oxidation susceptibility due to the formation of non-photochromic UV-transparent yttria. The observations clearly indicate the prospect of optimising both photochromic contrast and film stability simultaneously by obtaining a densest possible microstructure.

Possibilities for tuning of the band gap are explored to alter the yellowish film colour. By widening the band gap to over 3.1 eV, the entire visible spectrum would be transmitted and the film would appear colourless. The limited impact of deposition pressure on the band gap is addressed, and proof of concept is provided for tuning of the band gap through co-sputtering with dysprosium.

A metallic YH_y domain growth darkening model is introduced to describe the photochromic behaviour of YO_xH_y, in an attempt to clarify the mechanisms responsible for photochromism in REO_xH_ys. Film porosity, contrast, the memory effect, irreversible darkening of pre-existing YH_y phases, and kinetics, appear to support domain-growth-induced darkening.

Additional observations are presented in the appendices. The limited influence of ever-increasing illumination intensities on darkening potential is discussed, and evidence for UV-induced oxidation is provided. The disturbing effect of soda lime glass substrates on band gap determination using the Tauc plot method for thin, porous films is analysed.

2 Theoretical

2.1 Material — *The Y–O–H system*

2.1.1 Yttrium hydrides

Yttrium (Y) is a trivalent silver-metallic element with atomic number 39 [20]. It is both a transition metal and a rare earth element, and is found in group 3 and period 5 of the periodic table of elements (see Figure 2.1).

Like all rare earth elements Y can absorb up to three hydrogen (H) atoms per metal atom such that yttrium hydrides (YH_y) exist in a range $0 \leq y \leq 3$ [22]. As shown in the Y–H phase diagram in Figure 2.2, three equilibrium phases of YH_y are distinguished—the α, β, and γ phases—depending on H content, temperature, and pressure.

Pure Y has an hcp crystal structure with lattice parameters $a = 3.65$ Å and $c = 5.73$ Å, referred to as the α phase of the Y–H system (Figure 2.3) [22]. It is metallic with a resistivity of $\rho \sim 10^{-4}$ Ω cm [7]. It accommodates for H species through occupation of tetrahedral interstitial sites (as for γ-YH_3), forming an *ordered* α*-Y solid solution up to a solubility limit of $y^{\alpha}_{\max} = [\mathrm{H}]{:}[\mathrm{Y}] \approx 0.24$ at room temperature and atmospheric pressure

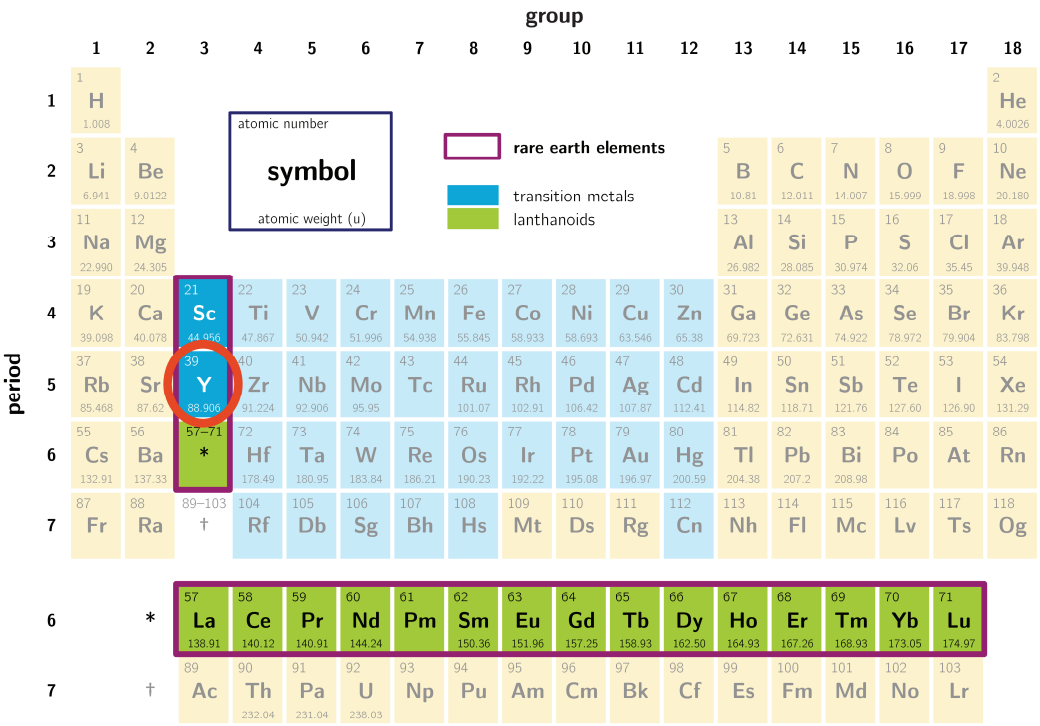

Figure 2.1. The rare earth metals in the periodic table of elements. Yttrium (Y) is found in group 3 and period 5 [21].

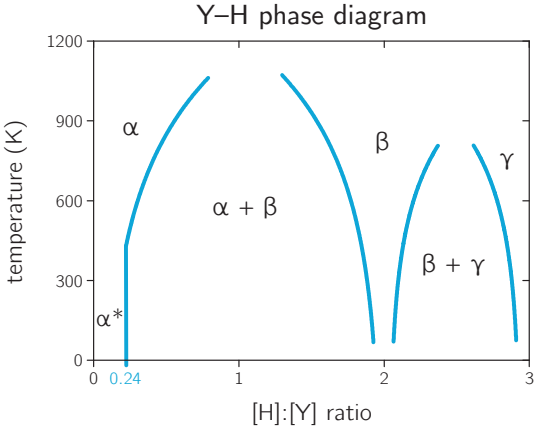

Figure 2.2. The Y–H equilibrium phase diagram at atmospheric pressure. Three phases are distinguished, i.e. α-Y, β-YH_2, and γ-YH_3 for increasing H content up to a maximum [H]:[Y] ratio of 3:1 [22, 24].

[23]. Solution of H into α-Y requires expansion of the crystal lattice and additional H insertion leads to the formation of β-YH_2 instead.

Yttrium dihydride (YH_2) is referred to as β-YH_2 and has an fcc structure with $a = 5.21$ Å, with its lattice points occupied by Y and the tetrahedral interstitial sites by H [22]. It is metallic with a resistivity of $\rho \sim 10^{-3}$ Ω cm, one order of magnitude above that of α-Y. β-YH_y allows for non-stoichiometric H content of $1.90 \leq y^{\beta} \leq 2.23$ through tetrahedral vacancies or H occupation of octahedral interstitial sites. H uptake is accompanied by an increase in resistivity due to localisation of electrons by H species and hence a reduction in free charge carriers [14, 22, 24].

Yttrium trihydride (YH_3) comprises the γ phase of the yttrium hydrides and has an hcp structure with $a = 3.68$ Å and $c = 6.62$ Å. Like in β-YH_2 the tetrahedral interstital sites are occupied by H species, accounting for two-thirds of H in γ-YH_3. The remaining third of H are located at octahedral interstitial sites [22, 25, 26, 27]. γ-YH_y exists in a range $2.77 \leq y^{\gamma} \leq 3$, again increasing the resistivity with H content to such an extent that there is a metal–semiconductor transition between the β and γ phases [10]. It is yellowish transparent with a band gap of 2.63 eV [8], and has been reported to exhibit photochromic behaviour at low temperatures and high H_2 pressures [7, 9, 11].

2.1.2 Yttria

Like all rare earth elements at ambient conditions α-Y readily oxidises in air, forming a passive yttria (Y_2O_3) layer:

$$2\,\mathrm{Y\,(s)} + \frac{3}{2}\mathrm{O_2\,(g)} \longrightarrow \mathrm{Y_2O_3\,(s)}.$$

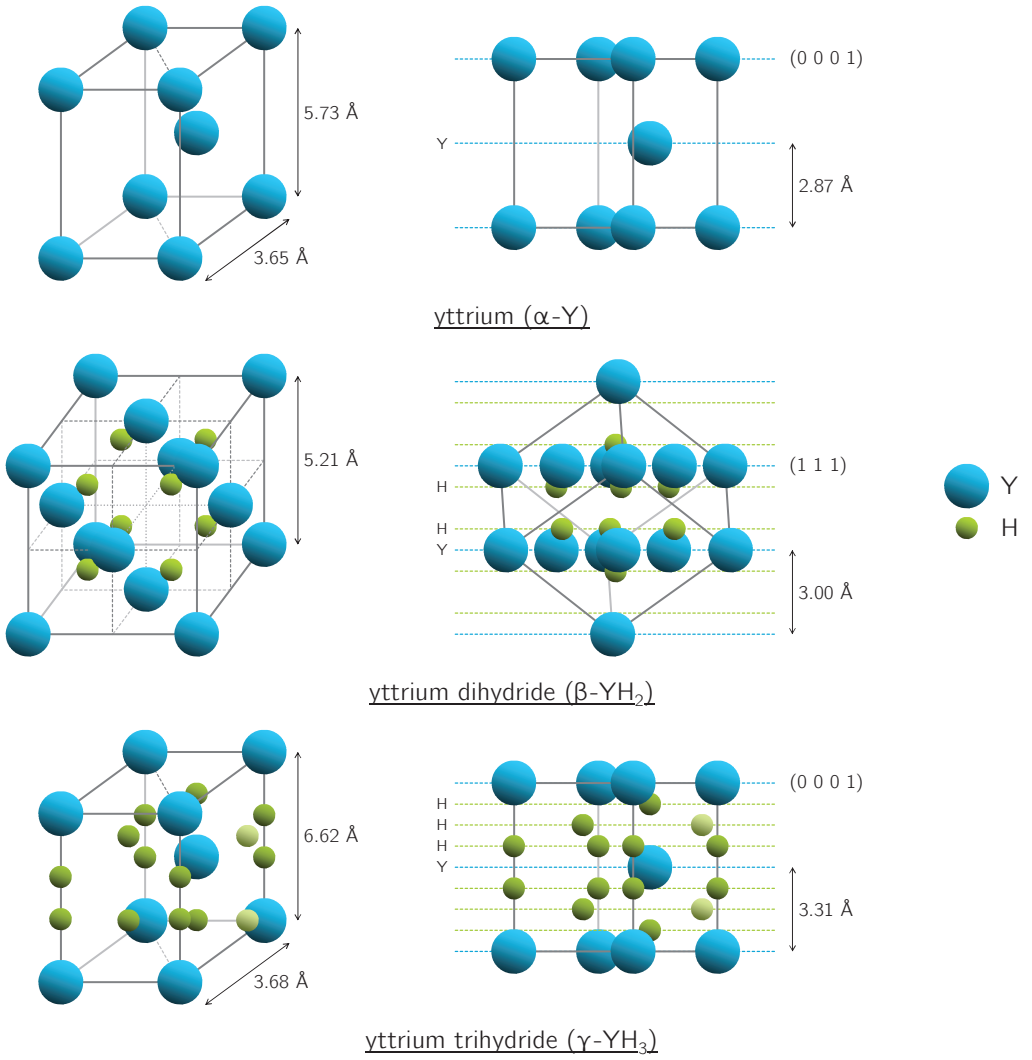

Figure 2.3. The crystal structures of the α (hcp), β (fcc), and γ (hcp) phases of the Y–H system, and side views of their highest-density crystallographic planes [22, 26].

β-YH_2 has also been shown to oxidise to form a 5–10 nm yttria layer upon air exposure [31]. Yttria has a *bixbyite* structure; a cubic unit cell with a lattice parameter of $a = 10.596$ Å, basically comprising $2^3 = 8$ fcc unit cells with the lattice points occupied by Y

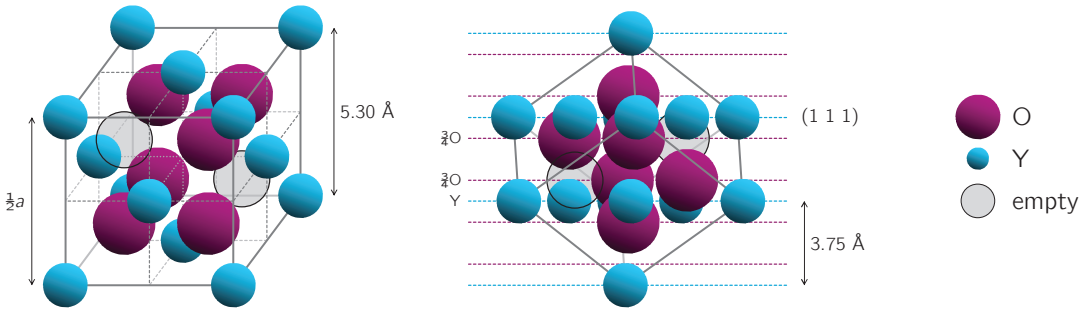

Figure 2.4. The crystal structure of $\left(\frac{1}{2}\right)^3 = \frac{1}{8}$ of a *bixbyite* yttria (Y_2O_3) unit cell, and side view of its highest-density (1 1 1) planes. O species occupy three-quarters of the tetrahedral interstitial sites [28, 29, 30].

and three-quarters of the tetrahedral sites occupied by O (Figure 2.4) [28, 29, 30]. It is an insulator with a band gap of 5.6 eV [32].

2.1.3 Yttrium oxyhydride

Yttrium oxyhydride (YO_xH_y) has an fcc crystal structure with reported lattice parameters of 5.27–5.39 Å [12, 17, 33]. Apparently similar to γ-YH_y, it is semiconducting with band gaps in the range 2.5–2.7 eV and, moreover, photochromic, with the main advantage of YO_xH_y being stable at ambient conditions [7, 17]. Photochromic YO_xH_y coatings are typically formed by air exposure of reactively sputtered β-YH_y thin films (from now on referred to as YH_y), leading to incorporation of oxygen by the crystal lattice [7, 17]. For YH_y to transform to photochromic YO_xH_y a sufficiently porous microstructure is required to allow for a full YH_y–YO_xH_y transition.

2.2 Electronic band structure

When two atoms are in close proximity, their outer atomic orbitals overlap. This interaction between the valence electrons of the respective atoms leads to a potential violation of Pauli's exclusion principle, which demands that no two electrons can occupy the same quantum state. To prevent this, their energy levels split into two separate levels, progressively introducing new energy levels as the number of atoms involved are increased. For dense, macroscopic sets of atoms such as crystals, the density of allowed states is so high that their energy distribution is basically a continuum—an *energy band* is formed, defining the allowed electron states in a material [34].

The highest occupied energy band is referred to as the *valence* band (of energy E_v). Electrons in the valence band are electrostatically bound to their atoms, separated from the *conduction* band (of energy E_c) in which they are free to move throughout the crystal. The energy difference between the valence and conduction bands are referred to as the *band gap* $E_\mathrm{g} = E_\mathrm{c} - E_\mathrm{v}$ (Figure 2.5c).

If the valence and conduction bands overlap, valence electrons can readily gain some energy to occupy a higher-energy state within the conduction band, so that they are confined to the crystal rather than a single atom. Such a material is referred to as a conductor, i.e. a metal (Figure 2.5a). Alternatively, in the presence of a band gap between the valence and conduction bands, valence electrons need to gain at least the band gap energy to be excited to the conduction band. For an insulator, the band gap is so wide that the probability for this to happen is negligible and electrons thus remain bound to their atoms (Figure 2.5c).

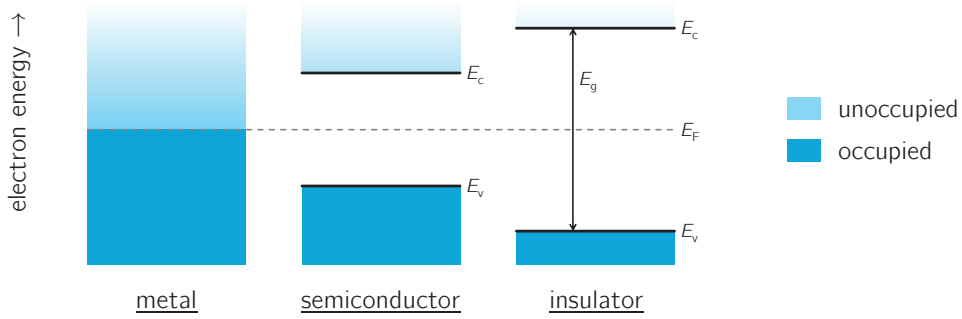

Figure 2.5. The energy band diagrams of a metal, a semiconductor, and an insulator, and indications of the occupied and unoccupied energy levels [34]. The Fermi level (E_F) marks the energy level for which the occupation probability is 50%. In metals, the valence (E_v) and conduction bands (E_c) overlap, allowing for conduction of electrons. In semiconductors and insulators, the valence and conduction bands are separated by a band gap E_g. By excitation of valence electrons across the band gap these materials become conducting.

Intermediate band gap materials are referred to as *semiconductors* (Figure 2.5b), in which valence electrons have a reasonable probability to be excited to the conduction band if they gain sufficient energy. This may be induced by e.g. absorption of photons of energies exceeding the band gap.

A distinction is made between *direct* and *indirect* band gaps. For a direct band gap the momentum of valence and conduction electrons is the same and excitation of valence electrons therefore only requires the transfer of energy. In an indirect band gap the valence and conduction electrons have a different momentum and an additional momentum transfer to the crystal is required for excitation. REO_xH_ys are indirect semiconductors [12, 17].

2.3 Photochromism

Photochromism refers to the *reversible* transformation of a material through absorption of photons, thereby changing its optical properties [35]. It was first reported in the 19th century and has since been utilised in many commercial applications, including photo-responsive sunglasses, optical data storage and switches, cosmetics, and smart windows [36, 37]. Both organic and inorganic compounds can exhibit photochromism, showing a variety of photochromic properties and underlying mechanisms.

2.3.1 The photochromic effect

Photochromism in YO_xH_y coatings is characterised by a reversible transformation between *bleached*, transparent states B and a *darkened*, opaque states D (Figure 2.6):

$$\mathrm{B} \rightleftarrows \mathrm{D}.$$

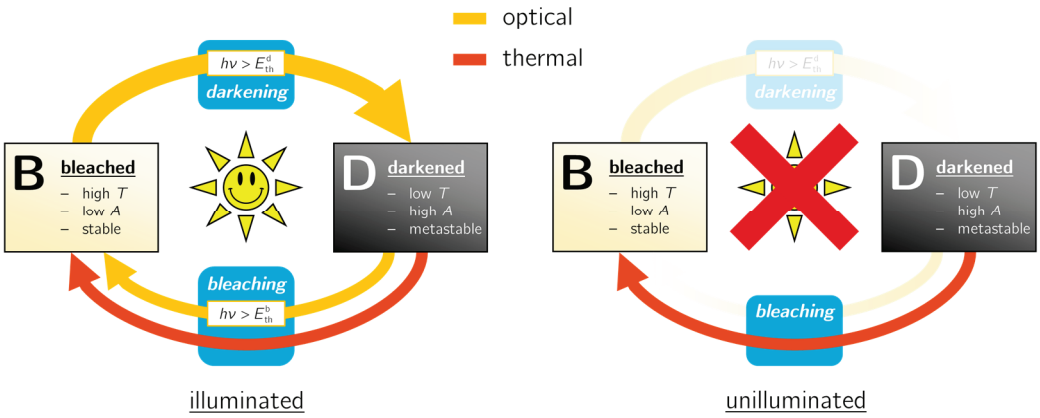

Figure 2.6. The darkening and bleaching processes associated with the photochromic effect in YO_xH_y, inducing a reversible transformation between a stable bleached state B (high transmittance T, low absorptance A) and a metastable, darkened state D (low transmittance T, high absorptance A). Photodarkening is the transformation of B to form D by absorption of photon energies $h\nu > E_{\mathrm{th}}^{\mathrm{d}}$. Optical bleaching a weaker, reverse reaction from D to B by absorption of photons of energies $h\nu > E_{\mathrm{th}}^{\mathrm{b}}$. Omnipresent is thermal bleaching of D to form B [17, 38].

Illumination of the transparent state B by EM radiation of sufficient energy results in darkening of the films to form D, leading to a reduced transmittance and an increased absorptance of visible (VIS) and near-infrared (NIR) radiation [7]. As the illumination ceases, the darkened state D returns to its original transparent state B.

Three processes are distinguished, i.e. *photodarkening*, *thermal bleaching*, and *photobleaching* [17]. Photodarkening is a result of absorption of EM radiation of energies exceeding some threshold value $E_{\mathrm{th}}^{\mathrm{d}}$, thereby darkening the material. For photochromic REO_xH_ys the darkening threshold is the electronic band gap [7, 17]. This photodarkening is counteracted by thermal bleaching, referring to ongoing thermally activated relaxation of the metastable darkened state D to the stable bleached state B. Additionally, photobleaching induces a transformation of D to B by absorption of photon energies above some optical bleaching threshold $E_{\mathrm{th}}^{\mathrm{b}} < E_{\mathrm{th}}^{\mathrm{d}}$.

2.3.2 Kinetics

When YO_xH_y is illuminated by photon energies above the darkening threshold energy $h\nu > E_{\mathrm{th}}^{\mathrm{d}}$, photodarkening initially prevails over bleaching. As the concentration of darkened state x_{D} increases a larger fraction x_{D} is susceptible to bleaching and a smaller fraction of remaining bleached state $x_{\mathrm{B}} = 1 - x_{\mathrm{D}}$ to photodarkening. This enhances the bleaching process and reduces the photodarkening rate until ultimately an equilibrium $x_{\mathrm{D}}^{\mathrm{eq}}$ is reached (Figure 2.7). Correspondingly, the averaged VIS–NIR transmittance $\bar{T}$ decreases with x_{D} down to a *saturation* transmittance $\bar{T}_{\mathrm{sat}}$, corresponding to a *saturation*

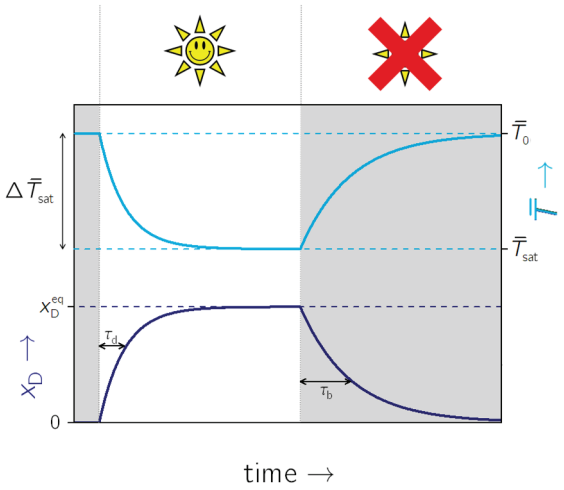

Figure 2.7. Development of the darkened concentrations $x_D(t)$ and average VIS–NIR transmittance $\bar{T}(t)$ during darkening and bleaching. Illumination of fully bleached YO_xH_y yields an increasing $x_D(t)$ until an equilibrium concentration x_D^{eq} is reached. Consequently, $\bar{T}(t)$ drops from an initial transmittance $\bar{T}_0$ down to a saturation value $\bar{T}_{sat}$. As illumination ceases, $x_D(t)$ drops exponentially down to zero while the transmittance returns to $\bar{T}_0$.

contrast $\Delta\bar{T}_{sat} = \bar{T}_0 - \bar{T}_{sat}$. As the irradiation ceases, x_D returns to zero under the influence of thermal bleaching while the transmittance returns to its initial value $\bar{T}_0$.

The exact kinetics and shapes of the darkening and bleaching curves are yet unknown. What *is* known is that photodarkening of REO_xH_ys is initially fast, followed by an elongated, increasingly slow darkening tail which does not seem to saturate [17, 18, 39]. Depending on film thickness, substantial contrasts of 20–30% are typically achieved within one or two hours. Thermal bleaching appears to follow a single exponential with a characteristic bleaching time constant τ_b, but is even slower at characteristic time scales of $\tau_b \sim 6$ h [18]. Furthermore, it has been shown that repetitive illumination cycles induce (i) faster darkening, and (ii) slower bleaching [7, 17, 18, 33, 39], referred to as the memory effect.

2.3.3 Proposed mechanisms

Improving the photochromic properties of YO_xH_y such as increasing darkening and bleaching rates and altering the yellowish film colour is difficult as the mechanisms involved in photodarkening are yet unknown. Better knowledge of the photochromic mechanism is therefore required. Two possible darkening models have, however, been proposed [17].

Plasmonic model

Photochromic silver halide (AgCl) glasses have been commercially available since the 1960s in e.g. self-darkening sunglasses [6, 17, 40]. The mechanism involved in the photo-

darkening of such species is based on the photo-induced diffusion of defects to form metallic Ag colloids or nanoparticles, inducing *surface plasmon resonance* and increasing film absorption. It could be a model for photochromism in REO_xH_ys.

Photochromic silver halide glasses consist of a suspension of ~10 nm AgCl crystallite inclusions in glass, containing several Cu^+ impurities (Figure 2.8a). Due to the limited size of these inclusions the scattering of light is minute and the glasses appear transparent. Incident UV radiation of energies higher than the 3.2 eV AgCl band gap induces the photoexcitation of a valence electron from a Cl^- anion towards the conduction band, subsequently transferred to a Ag^+ cation:

$$Cl^- \xrightarrow{h\nu} Cl^0 + e^-,$$
$$e^- + Ag^+ \longrightarrow Ag^0.$$

Now, the conduction electron of the Ag^0 atom may be transferred to successive neighbouring Ag^+ cations until it gets trapped at a low-energy grain boundary site or void marked by the 'T' in Figure 2.8a. Clustering of Ag^0 atoms at these positions in turn attracts more mobile Ag^+ species and electrons to form a metallic Ag^0 nanoparticle (Figure 2.8b).

In pure AgCl, the *hole* in the valence band of the electron-deprived Cl^0 atom would freely move between the Cl^- anions in the crystallite until it encounters a Ag^0 atom, but

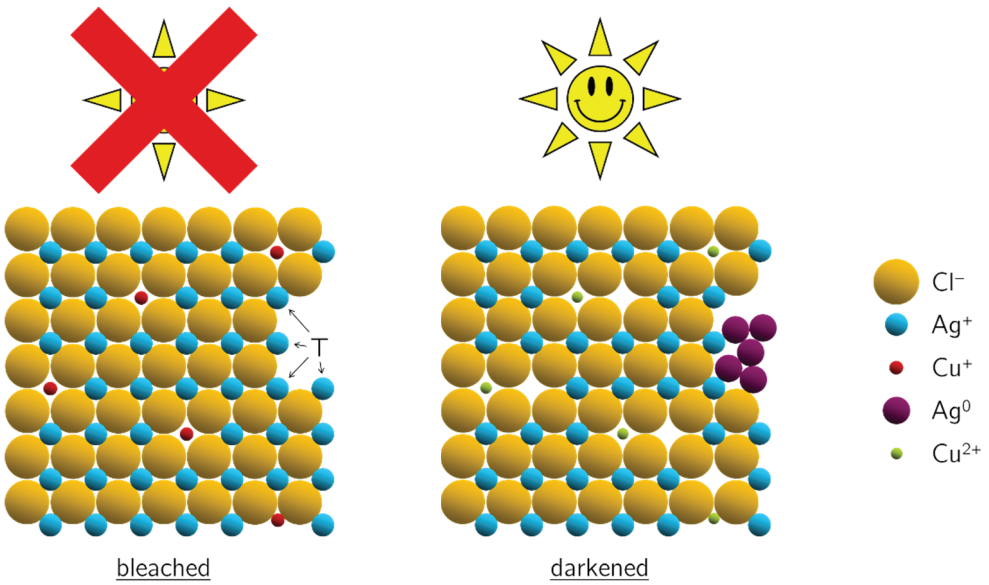

Figure 2.8. Darkening mechanism in photochromic silver halide (AgCl) glasses. UV illumination of the bleached state yields the electron transfer of Cl^- species towards Ag^+ to form neutral Ag^0 atoms. These additional electrons can readily migrate between Ag^+ ions throughout the crystal until they are trapped at low-energy surface sites marked by the 'T'. These neutral Ag^0 atoms in turn attract more Ag^+ ions from the crystal to form a neutral Ag^0 cluster by Ag^+ and electron diffusion. The resulting metallic nanoparticles act as plasmons to absorb light, effectively darkening the glasses. The Cu^+ ions act as traps for holes formed in the electron-deprived Cl^0 atoms to prevent recombination with electrons in Ag^0 [6].

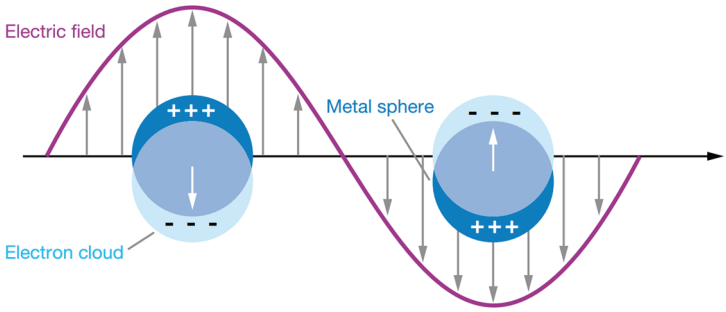

Figure 2.9. Absorption of EM radiation due to surface plasmon resonance. Surface electrons in metallic nanoparticles are displaced by the electrodynamic field imposed by incident light, effectively cancelling the field and hence absorbing the radiation [41].

the presence of Cu^+ impurities prevents this through *entrapment* of the hole and electron transfer from Cu^+ towards Cl^0:

$$Cl^0 + Cu^+ \longrightarrow Cl^- + Cu^{2+},$$

such that the net effect of UV irradiance is given by the reaction:

$$Ag^+ + Cu^+ \xrightarrow{h\nu} Ag^0 + Cu^{2+}. \tag{2.1}$$

The Ag^0 cluster acts as a metallic nanoparticle which is susceptible to *surface plasmon resonance*—the excitation of conduction electrons on the cluster surface by incident light, causing an in-phase oscillation and absorption of EM radiation as shown in Figure 2.9 [17, 41]. As a result the material appears darker.

The darkening process is similar to that observed in a photographic film [6]. What makes AgCl glasses photo*chromic*, however, is that as the irradiation ceases, the (not-so-deeply) trapped holes in Cu^{2+} are returned to the Ag^0 particles to reverse reaction 2.1. The metallic nanoparticles are once again absent from the material and it appears transparent.

Silver halide glasses are, just like REO_xH_ys, sensitive to photobleaching by excitation of conduction electrons from the Ag^0 nanoparticles to the conduction band of AgCl, requiring an energy of half the AgCl band gap of 3.2. eV [42]], although optical bleaching of REO_xH_ys occurs at much lower energies [17]. Very different from photochromic REO_xH_ys are the photodarkening rates of silver halides, which are orders of magnitude higher with considerable darkening within the order of seconds [43]. Also different is the darkening spectrum—due to the generally homogeneous size distribution of silver colloids the absorption of darkened silver halides is typically concentrated around several wavelengths [40], whereas absorption of darkened REO_xH_ys is colour-neutral and apparently distributed evenly over a wide wavelength range [7].

Multivalent defect model

An alternative mechanism proposed for photochromism in REO_xH_ys is the *multivalent defect model*, based on point defects of valence n in the crystal [17]. These defects introduce deep donor levels D^{n+} within the band gap as illustrated in Figure 2.10. Photoexcitation of valence electrons to the conduction band yields free electrons in the crystal which can be trapped at these deep donor levels (Figure 2.10b). The resulting hydrogen-like system is a slightly higher-energy donor level $D^{(n-1)+}$ with the electron loosely bound to its positively charged $D^{(n-1)+}$ core as the core is shielded from the electron by the entire crystal (Figure 2.10c). Consequently, the electron can readily occupy an excited state D^*, where it may reside for some time. The latter stage is somehow associated with the darkened state of the material.

For the electron to return to the valence band it is to be excited to the conduction band prior to electron–hole recombination (Figure 2.10d–e). The required energy can be provided for thermally or optically, and is considerably lower than the band gap energy. As more and more electrons are re-excited to the conduction band and subsequently recombined the material gradually returns to its original, transparent state.

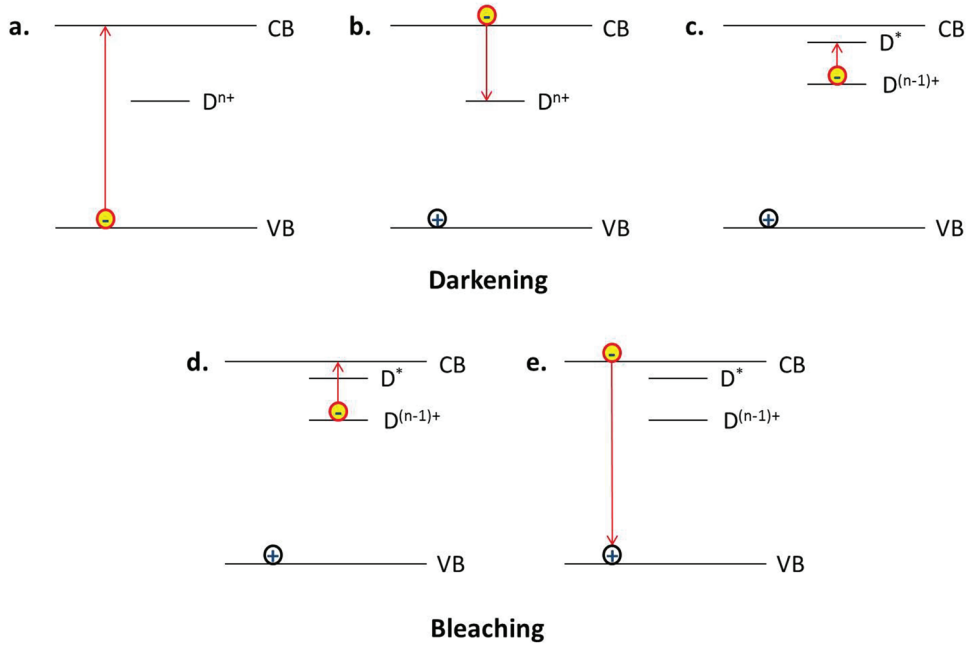

Figure 2.10. Darkening and bleaching processes of the multivalent defect model [17]. Darkening consists of three stages; **(a)** photoexcitation of a valence electron to the conduction band, **(b)** entrapment of a free electron at a deep donor level, and **(c)** excitation to excited state D^*, associated with the darkened state of the material. Bleaching occurs by **(d)** re-excitation to the conduction band, and **(e)** recombination with the hole in the valence band.

2.4 Electrodynamics

2.4.1 Electromagnetic radiation

Electromagnetic (EM) radiation can be characterised as both a propagating wave of wavelengths λ or particle-like energy quanta (*photons*), referred to as the *wave–particle duality* [44]. The relation between photon energy E_p and wavelength λ is defined by the Planck–Einstein relation:

$$E_\mathrm{p} = h\nu = \frac{hc}{\lambda},$$

where h is Planck's constant, ν is the photon frequency, and c is the speed of light. Characterisation of EM radiation in terms of energy E_p or wavelength λ is thus directly interchangeable.

2.4.2 Transmittance, reflectance and absorptance

When propagating EM radiation of intensity I_0 encounters an object (Figure 2.11a) it is either transmitted, reflected, or absorbed, the extents of which are quantified by the transmittance T, reflectance R, and absorptance A. All three are a function of wavelength λ. For conservation of energy the three quantities are preserved:

$$T + R + A = 1.$$

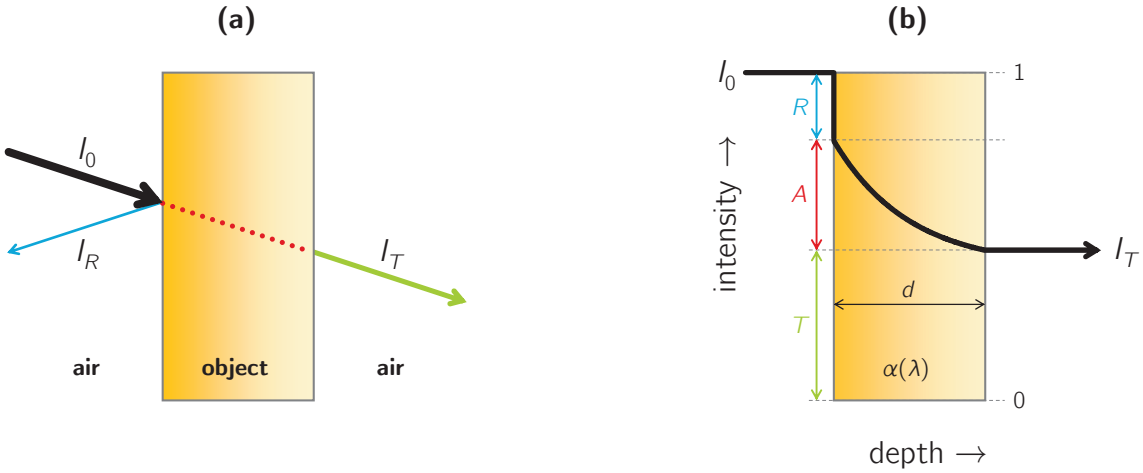

Figure 2.11. Transmittance T, reflectance R and absorptance A of incident EM radiation of intensity I_0 onto an absorbing medium.*
(a) Incident radiation I_0 is partly reflected at the surface (I_R), partly absorbed by the object, and partly transmitted (I_T).
(b) The intensity–depth profile of incident radiation I_0 onto a medium of thickness d and absorption coefficient $\alpha(\lambda)$.

* Refraction due to varying refractive indexes are neglected as the incident radiation involved in the photospectrometry studies in this research is solely normal to the considered surfaces.

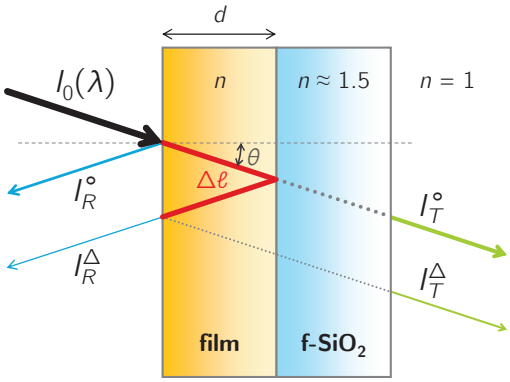

Figure 2.12. Example of thin-film interference in an absorbing film on a f-SiO_2 substrate. Incident EM radiation of intensity I_0 is reflected from two separate interfaces, i.e. the front film surface and the film–substrate interface. As a result the phases of the two reflected beams I_R° and I_R^Δ are mutually shifted by an optical path length difference of $\Delta\ell$, which leads to interference of the two reflected beams. The same accounts for the two transmitted beams I_T° and I_T^Δ—the first of which is not reflected at all while the latter is reflected twice; from the film–substrate interface and the front film surface.

The intensities of the transmitted and reflected waves are given by

$$I_T = TI_0,$$
$$I_R = RI_0.$$

The absorptance by an absorbing medium of width d and an absorption coefficient $\alpha(\lambda)$ is given by $A = e^{-\alpha d}$, implied by the Lambert–Beer law [44]:

$$I_T = (1 - R)I_0 e^{-\alpha d} \tag{2.2}$$

such that the 'absorbed intensity' I_A is

$$I_A = AI_0.$$

The resulting intensity–depth profile of radiation of intensity I_0 incident on an absorbing object of width d and an absorption coefficient $\alpha(\lambda)$ is depicted in Figure 2.11b.

2.4.3 Interference

Typical of thin films on a substrate is the occurrence of *thin-film interference* due to reflection from multiple surfaces and interfaces and film thicknesses of the order of visible wavelengths [45]. Incident radiation of intensity I_0 might, for instance, be reflected at the film–substrate interface rather than at the film surface, as indicated by I_R^Δ in Figure 2.12. As this beam is parallel to a beam I_R° directly reflected from the film surface the two beams are subject to interference.

For radiation in a film propagating at an angle θ relative to the surface normal, this means the internally reflected beam I_R^Δ has traversed an additional optical path length $\Delta\ell = 2nd/\cos\theta$, where n is the refractive index of the film, and d is the film thickness. If

$\Delta\ell$ is equal to an integer number of wavelengths $m\lambda$, this leads to *constructive interference* for:

$$2nd = m\lambda \cos\theta,$$

whereas *destructive interference* occurs for a phase shift corresponding to half a wavelength:

$$2nd = \left(m + \frac{1}{2}\right)\lambda \cos\theta.$$

The same accounts for two (in)directly transmitted waves; one directly transmitted beam I_T°, and one beam I_T^{Δ} reflected twice—once at the film–substrate interface and subsequently at the film surface.

Because of thin-film interference, the spectral transmittances $T(\lambda)$ and reflectances $R(\lambda)$ exhibit an oscillating behaviour, as shown in Figure 2.13 for a 100 nm-thick YO_xH_y film. The optical path length difference between the transmitted and reflected beams is $\frac{1}{2}\Delta\ell = \frac{1}{2}m\lambda$, resulting in a phase shift of half a period. A maximum $T(\lambda)$ thus coincides with a minimum $R(\lambda)$ such that the sum of the two cancel out to obtain an interference-free absorptance $A(\lambda) = 1 - T(\lambda) - R(\lambda)$. Larger film thicknesses result in an increasing amount of interferences fringes, as well as a shift of fringe positions towards larger wavelengths.

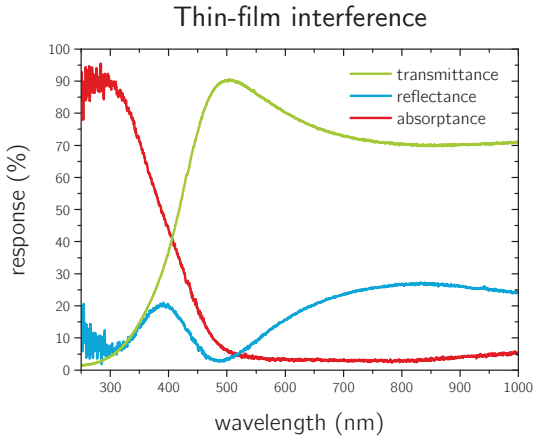

Figure 2.13. Spectral transmittance $T(\lambda)$, reflectance $R(\lambda)$ and absorptance $A(\lambda)$ of a day-old 100 nm-thick YO_xH_y sample sputter-deposited at 0.45 Pa. The transmittance shows a maximum near 500 nm wavelengths due to constructive interference and a minimum in the proximity of 850 nm caused by destructive interference. Destructive and constructive interference for the reflected intensities coincide with these wavelengths, respectively. As a result the spectral absorptance $A(\lambda) = 1 - T(\lambda) - R(\lambda)$ is rid of any oscillations.

2.4.4 Irradiance and photon flux

The intensity of EM radiation is typically quantified by the amount of power P transported per unit area A, i.e. the energy flux, referred to as *irradiance* $I = \partial P / \partial A$. It generally consists of a wide range of *spectral irradiances* $I(\lambda)$ and is found by integration of $I(\lambda)$:

$$I = \int I(\lambda)\, d\lambda.$$

As each photon of wavelength λ has an energy $E_\mathrm{p} = hc/\lambda$, a spectral irradiance $I(\lambda)$ corresponds to a *spectral photon flux* of

$$\Phi_\mathrm{p}(\lambda) = \frac{I(\lambda)}{E_\mathrm{p}(\lambda)} = I(\lambda)\frac{\lambda}{hc}$$

which defines the number of incident photons of wavelength λ per unit area per unit time. This corresponds to a total *photon flux*

$$\Phi_\mathrm{p} = \int I(\lambda)\frac{\lambda}{hc}\, d\lambda,$$

a useful quantity to describe the amount of incident photons on a sample illuminated by a known irradiance spectrum $I(\lambda)$.

3 Methods and procedures

3.1 Sputter deposition

3.1.1 Magnetron sputtering

A conventional technique for the manufacturing of thin films and coatings is through *sputtering*; a process which refers to the ejection of surface atoms from a so-called target resulting from bombardment by energetic ions [46]. This typically involves the ignition of a plasma between two electrodes and the ionisation of argon* (Ar) gas, dissociating Ar molecules into negatively charged (*primary*) electrons and positively charged Ar^+ ions. For the deposition of Y coatings, the Ar^+ ions are accelerated towards a high-purity Y target cathode where they eject Y atoms upon impact. The sputtered Y atoms subsequently condense onto a floating substrate to form an Y film as schematically represented in Figure 3.1.

The plasma is sustained by the emission of *secondary* electrons from the target, also resulting from Ar^+ bombardment. As these electrons are accelerated away from the negatively charged cathode they create new ions upon collision with Ar molecules, which in turn partake in the sputtering process [47].

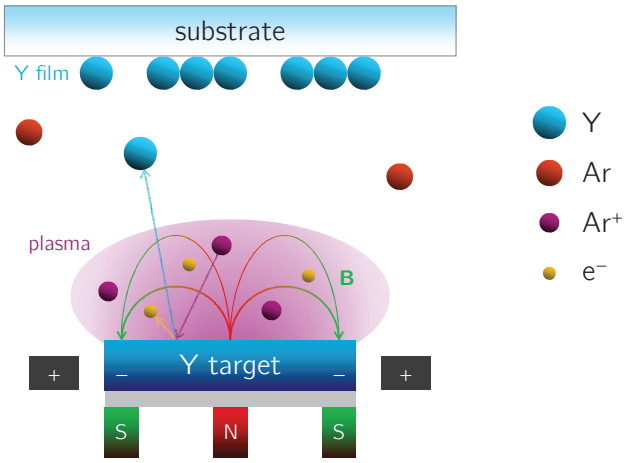

Figure 3.1. Schematic representation of a typical magnetron sputtering configuration. Positive Ar^+ ions from the plasma are accelerated towards a negatively biased Y target, ejecting surface atoms towards a floating substrate where they form an Y film. Secondary electrons also emitted from the target surface ionise Ar atoms in the chamber to sustain the plasma. The magnetic field **B** over the target confines these secondary electrons and the plasma to the target surroundings, greatly enhancing the ionisation efficiency [46].

* Ar is an (abundant) inert gas and therefore non-reactive, required for high-purity films.

The key characteristic of *magnetron sputtering* is the confinement of secondary electrons to a closed loop around the target through the application of a magnetic field. A permanent magnet with its north pole (N) facing the target is placed underneath the target centre, and is surrounded by a series of magnets of opposite magnetisation (S) beneath the outer edges of the target. Consequently, a half-donut-shaped outward-directed radial magnetic field **B** is formed covering the target, as depicted in Figure 3.1. The Lorentz forces acting upon moving secondary electrons within the magnetic field are oriented inwards and hence confine the electrons to the magnetic field, increasing the secondary electron density. This greatly enhances the ionisation probability and consequently the sputtering yield.

To prevent atmospheric gases and other contaminants such as moisture from interfering with the sputtering process and reacting with the film or the sputtering target, the entire process is conducted in a vacuum chamber.

3.1.2 Reactive sputter deposition

Additional to Ar, reactive gases such as oxygen or hydrogen may be injected into the sputtering chamber. Sputtered Y atoms react with these gases, consequently forming a compound film rather than pure Y. This technique is referred to as *reactive sputter deposition*. For the growth of YH_2 films hydrogen gas is to be added to the chamber.

Reactive sputtering involves reaction of the target with reactive species in the chamber, altering the target surface. This might lead to the formation of an insulating layer such as yttria in the case of reactive O_2 sputtering or opening of the chamber. This inhibits the discharge current flowing through the plasma required for sustaining it, thereby stopping the process. To remove the oxide layer from the target, radio frequency (RF) sputtering can be applied rather than direct current (DC) sputtering. In RF sputtering the voltage over the plasma is alternated rapidly, in the order of MHz, removing the need for a conducting target as no net current is imposed.

In the presence of H_2, sputter-ejected Y reacts with H_2 to form YH_y deposits in the chimney surrounding the target (see section 3.1.4). Internal stresses may cause these deposits to flake off the chimney interior and induce a short-circuit between the target and the anode, bypassing the gas discharge and killing the plasma. This might require the physical removal of flakes from the target, yielding the target useless until cleared.

3.1.3 Film morphology

Structure–zone model

Due to the unidirectional growth of sputter-deposited films their principal microstructural feature is a columnar grain structure, oriented parallel to the growth direction. Yet

depending on temperature and the energy of incident Y atoms, four types of film morphologies are distinguished using the *structure–zone model*, as depicted in Figure 3.2 [48, 49].

At low temperatures, sputter-ejected Y *ad*atoms adsorbed onto the film or substrate surface are rather immobile and tend to either nucleate to form new grains or be incorporated by existing grains at the position of impact. Due to the stochastic spatial and angular distribution of incident Y this may lead to *atomic shadowing*, whereby pores remain unfilled as film irregularities leave these unexposed to the somewhat oblique incident Y flux. The resulting microstructure is of a porous and textured fibre-grained type as indicated by *zone I* in Figure 3.2.

For homologous surface temperatures $T_\mathrm{h} \equiv T/T_\mathrm{m} \gtrsim 0.3$, where T_m is the material melting point, surface diffusion is activated, greatly enhancing adatom mobility. Consequently, adatoms may now diffuse over the film surface to be trapped at low-energy sites, i.e. voids or surface irregularities, increasing film density. Moreover, surface energies are lowered by grain growth due to grain boundary diffusion. The resulting microstructure is referred to as zone II.

Higher homologous temperatures of $T_\mathrm{h} \gtrsim 0.5$ result in recrystallisation of the film due to activation of bulk diffusion. This stage involves the loss of any texture and columnar grain morphologies, yielding an amorphous microstructure as indicated by *zone III* in the structure–zone model.

A fourth *transition* zone between zones I and II is identified as zone T, and comprises a dense array of fibrous grains. In temperature ranges of $0.2 \lesssim T_\mathrm{h} \lesssim 0.4$, a lack of sufficient substrate temperatures for notable surface diffusion is compensated for by a local temperature shift caused by high-energy incident Y atoms, inducing surface diffusion and a high film density [50].

Considering an Y melting point of $T_\mathrm{m} \approx 1500$ K, room temperature corresponds to a homologous temperature of $T_\mathrm{h} \approx 0.2$. At these temperatures adatom diffusion is thus neg-

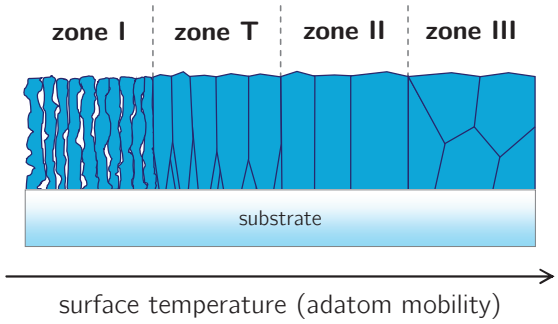

Figure 3.2. The four microstructures of sputter-deposited films as defined by the structure–zone model. Increasing temperatures result in higher-density films due to higher adatom mobilities. Typical microstructures for metallic films at room temperature are zones I and T, mainly depending on deposition pressure [49].

ligible and zones II–III microstructures are unfeasible. Depending on the sputtering geometry and deposition pressure, incident Y energies may however be sufficiently high for high-density zone T or mixed zones I–T films at room temperature.

Pressure–distance product

At room temperature the energy of incident Y atoms at the film surface is mainly governed by collisions with Ar species between the target and substrate. This involves the transfer of energy and momentum from Y towards Ar. For high deposition pressures, collision probabilities are large, and hence Y energies are low. For large target–substrate distances, too, many Ar species are encountered before reaching the substrate, and Y energies are low. The energy of incident Y atoms is therefore roughly determined by the *pressure–distance product*, i.e. the product of the deposition pressure and the target–substrate distance, reducing incident Y energies arriving at the film surface [49, 51].

High pressure–distance products result in porous zone I microstructures. As the pressure–distance product is reduced, Y energies are increased and film morphologies move towards lower-porosity, higher-density, larger-grains zone T microstructures. The lower the deposition pressure, the denser the resulting film.

3.1.4 Film growth

Sputtering system

Sputter deposition of YH_y films is executed using an AJA International ATC 2400 magnetron sputtering system. It consists of a 61 cm-diameter cylindrical ultra-high vacuum (UHV) chamber as depicted in Figure 3.3, connected to a separate load lock vacuum to insert and retrieve the sample while retaining vacuum in the chamber. The system is equipped with a rotatable substrate holder surrounded by six tiltable sputtering guns. Each gun consists of a target, electrodes for ignition and sustainment of the plasma, permanent magnets for confining the plasma, a chimney which aims the sputtered atomic flux towards the substrate, and a shutter which is used to close off the chimney to prevent

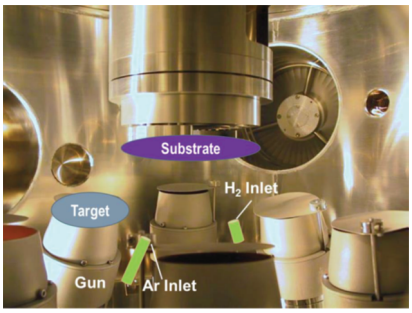

Figure 3.3. AJA International ATC 2400 UHV sputtering chamber interior, with the rotatable substrate holder (top), the six guns symmetrically surrounding the substrate holder, and indications of the Ar and H_2 inlets [17].

contamination of the target from other sputtering targets when idle. The substrate holder also has a shutter to prevent unwanted film growth during *pre-sputtering* (see Procedure). Furthermore, the substrate holder is equipped with two electrodes allowing for radio frequency (RF) sputtering of the substrate or sample to remove any undesirable substrate or film surface layers. For RF sputtering the discharge voltage is alternated rapidly, in the order of MHz, such that no net discharge current is imposed. This allows for sputtering of insulating surfaces such as glass substrates.

To manage the pressure in the chamber it is connected to a UHV pumping system. A pressure valve between the chamber and the pumps allows for direct control of the pressure. A flow-controlled Ar inlet supplies the chamber of Ar, and separate H_2 and O_2 inlets are connected for reactive sputtering purposes.

Procedure

Sputter deposition is a complex process with numerous physical parameters, each affecting the resulting film morphology, composition, and properties. These include temperature, base pressure (prior to sputtering), deposition pressure, Ar and H_2 flows, discharge voltage (target bias), discharge current (current through the plasma), discharge frequency, gun tilt, target–substrate distance, substrate rotation, and substrate surface conditions.

To establish the effects of deposition pressure (and composition) on YO_xH_y (and YO_xH_y–DyO_xH_y) film properties, all other variables are kept constant throughout this research.

Contamination of the sputtering chamber from residual gases is prevented by initiating the deposition procedures at base pressures of 10^{-6} mbar or lower. Prior to deposition, substrate surfaces are RF sputtered at 20 W for approximately 15 minutes in pure Ar at a pressure of 0.30 Pa to remove several nanometres of substrate and ensure a clean, uniform surface. During substrate cleaning the substrate is rotated at a run speed setting of 60 corresponding to an angular velocity of 75°/s (12.5 rpm).

The target is cleared of any reacted surface layers by several minutes of pre-sputtering, under Ar and H_2 pressures identical to deposition conditions. The target shutter is opened to prevent unnecessary flaking. Reacted surface layers are considered removed once the discharge voltage and current have stabilised, i.e. when the discharge resistivity is constant. During pre-sputtering the substrate is shielded by a substrate shutter to prevent premature film deposition.

All depositions are conducted at room temperature. Ar and H_2 gas flows are 35 sccm and 5 sccm, respectively. The discharge power on the Y gun is kept at 100 W DC during sputtering.

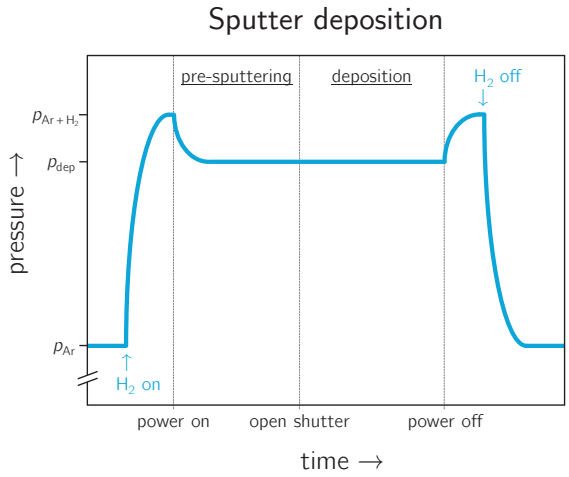

Figure 3.4. Chamber pressure profile during sputtering. Prior to pre-sputtering, the substrate shutter is closed, Ar is added to the chamber, and the pressure valve is set as to obtain the desired Ar pressure p_{Ar}. Adding H_2 now yields an increase in pressure, up to $p_{\mathrm{Ar+H_2}}$. Pre-sputtering is initiated by imposing electric power on the target, igniting the plasma and yielding a slight pressure drop down to p_{dep} due to reaction of H species with sputtered Y. When pre-sputtering is finished the deposition is started simply by opening the substrate shutter. To abort deposition the target power is turned off, yielding a pressure increase back to $p_{\mathrm{Ar+H_2}}$, after which the H_2 flow is stopped, marking the end of the sputtering process [17].

The pressure in the sputtering chamber is monitored during deposition. A typical pressure–time diagram as represented in Figure 3.4 is a good indicator of the sputtering procedure.

Uniform films

To determine the effect of deposition pressure on the structural, optical, and photochromic properties of air-exposed YO_xH_y films, series of 100(3) nm-thick YH_y films are reactively sputtered for 11"54' at varying deposition pressures of 0.27 Pa, 0.40 Pa, 0.45 Pa, and 0.60 Pa. Four 0.5 mm-thick UV grade f-SiO_2 substrates of 10 mm × 10 mm are placed at the centre of the substrate holder and rotated at an angular velocity of 75°/s (12.5 rpm) to obtain four uniform, identical films for each pressure. The Y gun is tilted towards the substrate holder centre at a linear drive setting of 5 mm, corresponding to an inward gun tilt of 31.3°.

Gradient films

Due to the geometry of the sputtering setup (Figure 3.3), the target–substrate distance $s(x)$ varies over the substrate holder, as depicted in Figure 3.5. This implies that sputter deposition of YH_y films onto a *stationary* substrate yields a one-dimensional pressure–distance gradient over the substrate as one end of the substrate is closer to the target than the opposite end, basically the equivalent of a continuous pressure series within a single sample. The resulting film morphology therefore gradually changes from a relatively

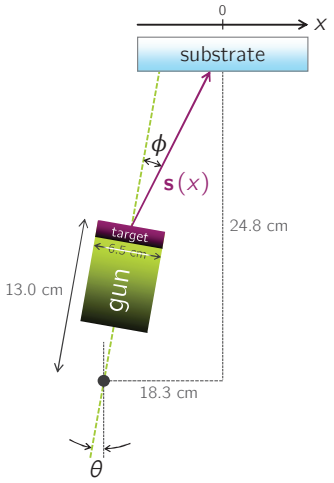

Figure 3.5. Gun–substrate sputter geometry. The target–substrate distance s varies over the length direction x of a stationary, elongated substrate. Additionally, the atomic flux decreases towards higher angles ϕ as the majority of sputtered atoms is directed along the target normal ($\phi = 0$) [49].

dense structure at the substrate end close to the target to a more porous structure at the far end.

Such gradient samples offer possibilities of investigating the effect of pressure–distance product on optical and photochromic properties such as band gaps and contrast, as well as acquiring a wide range of YH_y–YO_xH_y film morphologies. Using these gradients, the effect of high porosity and low film thickness on band gap determination for Menzel glass substrates (Appendix B) and the remarkable irreversible darkening behaviour of the boundary between YH_y and YO_xH_y phases (section 4.3.3) are addressed.

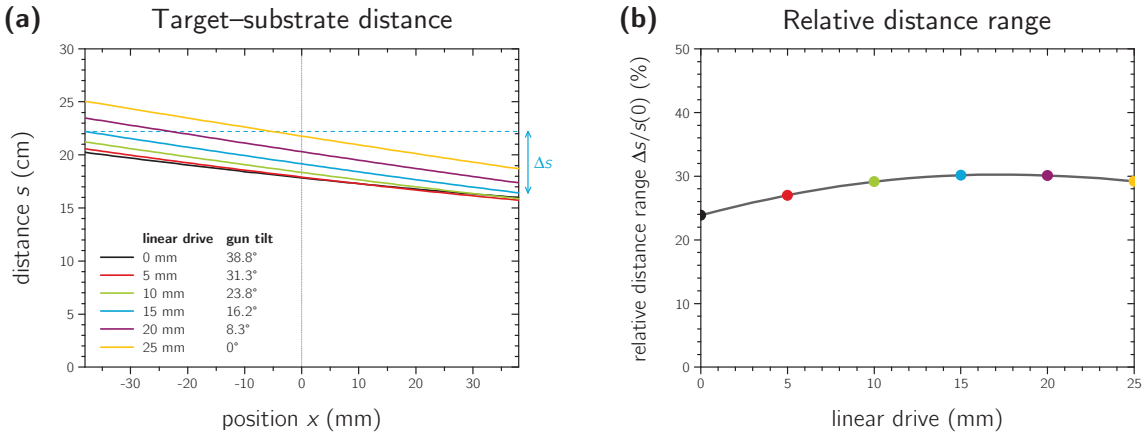

Figure 3.6. Effect of gun tilt θ on the varying target–substrate distances $s(x)$ over a stationary 76 mm-long substrate.
(a) Target–substrate distance $s(x)$ as a function of sample position x for varying gun tilts θ. Note that the x-axis is mirrorred with respect to the x-axis depicted in Figure 3.5.
(b) The resulting target–substrate distance ranges $\Delta s/s(0)$ over a 76 mm-long substrate relative to the sample centre $x = 0$, as a function of linear drive setting (i.e. gun tilt θ).

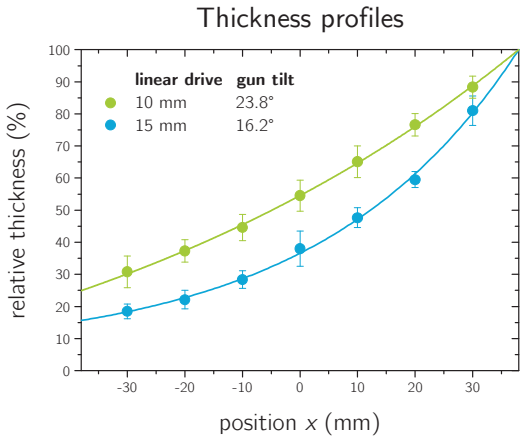

Figure 3.7. Film thickness profiles for stationary substrates and two different gun tilts θ, relative to the film thickness of sample position $x = 38$ mm closest to the target. Note that the depicted x-axis is mirrored with respect to that of Figure 3.5.

To maximise the range of pressure–distance products over gradient samples, elongated substrates of 76 mm × 26 mm are aligned parallel to the target–substrate direction during deposition. For several gun tilts, the resulting target–substrate distances $s(x)$ for different positions x on the substrate relative to the substrate centre at $x = 0$ are computed from the sputtering geometry of Figure 3.5, and shown in Figure 3.6a. The difference in $s(\mp 38\text{ mm})$ between the two substrate ends relative to $s(0)$ as a function of the gun tilt are given by the relative target–substrate distance ranges $\Delta s/s(0)$, as shown in Figure 3.6b. The largest relative target–substrate distance variations over a 76 mm-long substrate are for linear drive settings of 15–20 mm. As a higher linear drive involves the gun being pointed further away from the substrate and hence results in a lower film thickness, a linear drive setting of 15 mm is employed for gradient sputter deposition to obtain a largest possible pressure–distance product range over a single sample.

As the sputtered atom flux is largest in the direction along which a single gun is aimed resulting film thicknesses are highest there. For large substrates, this results in a thickness gradient with lower thicknesses towards higher angles ϕ as indicated in Figure 3.5. Resulting thickness profiles for two different gun tilts θ as a function of position x from the sample centre are shown in Figure 3.7. The thin end corresponds to a high pressure–distance product and hence high film porosity, and the thick end to a low pressure–distance product and high film density.

Co-sputtered gradient films

Rather than using a single target for sputter deposition, multiple targets can be employed simultaneously to grow a compound film, referred to as *co-sputtering*. By tilting two guns of different target materials towards the substrate a dual-compound film is deposited. The

composition of the film depends on the sputtered atomic flux ratios arriving at the substrate.

To study the influence of alloying photochromic YO_xH_y with Dy on the band gap, a DyH_y–YH_y gradient film is reactively co-sputtered, with compositions varying between two ends of the film. This is done by varying the atomic flux ratios arriving at different substrate positions by pointing the two Dy and Y guns at opposite substrate ends.

By tilting two opposite Dy and Y guns towards two opposite ends of a stationary, elongated 76 mm × 26 mm × 1 mm Menzel glass (soda lime glass) substrate, a gradient compound film is deposited. The composition varies gradually from mainly DyH_y at the substrate end closest to the Dy gun to mainly YH_y at the opposite end closest to the Y gun. To obtain a linear composition gradient, the atomic flux gradients of each separate gun should also be linear. As a 10 mm linear drive setting (23.8° gun tilt) yields a roughly linear thickness gradient (Figure 3.7), these settings are used for both guns.

To transform to photochromic DyO_xH_y upon air exposure DyH_y films should be grown at a deposition pressure of at least 0.7 Pa [17]. Deposition of the DyH_y–YH_y film is therefore conducted at a pressure of 0.72 Pa to ensure a full dihydride–oxhydride transition. As Dy has a higher atomic number than Y its atomic flux is larger than for Y [49]. To obtain similar atomic Dy and Y fluxes the discharge power on the Dy gun is kept at 70 W DC rather than 100 W DC on the Y gun.

3.2 X-ray crystallography

3.2.1 X-ray diffraction

A conventional technique for the determination of the structure of crystalline solids is X-ray diffraction (XRD) [52]. Both lattice type and lattice parameter can be established with great accuracy, typically of the order 0.001 Å. To determine the influence of deposition pressure on the lattice size of sputter-deposited YH_y and YO_xH_y films XRD measurements are therefore conducted. As it has been well-documented that both YH_y and YO_xH_y films have an fcc structure [7, 22, 33, 15], the XRD measurements are solely focused on determination of the lattice parameter.

Incident EM radiation may result in the interference of coherent waves scattered from multiple atoms in a crystal, referred to as *diffraction*. For an incident angle θ the difference in optical path length $\Delta\ell$ between two parallel beams reflected by neighbouring atomic planes at an interplanar distance d is given by $\Delta\ell = 2d \sin\theta$, as indicated in Figure 3.8. When $\Delta\ell$ is equal to an integer number m of wavelengths λ, *Bragg's law* is fulfilled and this results in *constructive interference* at angles θ:

$$2d \sin\theta = m\lambda.$$

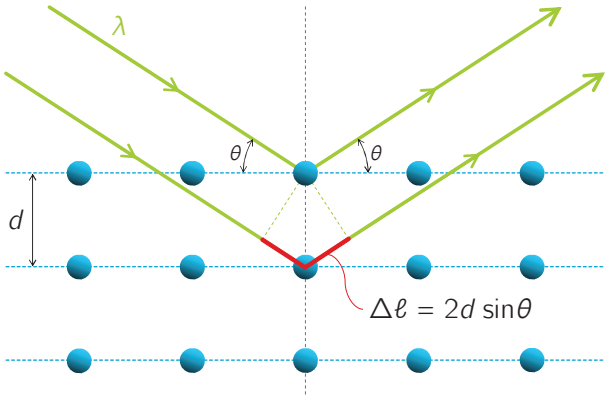

Figure 3.8. Elastic scattering of incident EM radiation by different atoms separated by a distance d in a crystal. The resulting traversed optical path length difference $\Delta\ell = 2d\sin\theta$ between two parallel beams scattered by multiple atomic planes may result in interference (diffraction) [52].

Due to the spatial periodicity of atoms in crystalline solids these conditions are simultaneously fulfilled for all atoms in a crystallite, and the measured intensity of the scattered beam for Bragg angles θ is therefore greatly enhanced. This results in a peak in the *diffraction pattern*, i.e. the diffracted intensity as a function of Bragg angles.

Depending on the crystal structure multiple sets of atomic planes can contribute to constructive interference. As close-packed planes contain the highest periodicity these result in the highest diffraction peaks, e.g. the {1 1 1} and {2 0 0} sets of planes for fcc crystals and {1 1 0} and {2 1 1} for bcc. For cubic lattices, the interplanar distances $d_{hk\ell}$ for different $\{h\ k\ \ell\}$ sets of planes are well-defined as a function of the lattice parameter a:

$$d_{hk\ell} = \frac{a}{\sqrt{h^2 + k^2 + \ell^2}},$$

such that the associated Bragg angles $\theta_{hk\ell} = \arcsin\left(n\lambda\sqrt{h^2 + k^2 + \ell^2}/2a\right)$ are also well-defined. From the relative θ positions of the diffraction peaks one can therefore determine the crystal structure of a material, as well as the lattice parameter.

As lattice parameters a are typically in the order of several Å, so are the interplanar distances $d_{hk\ell}$ and the optical path length differences $\Delta\ell$. To fulfil Bragg's law the wavelength λ of the incident beam should therefore not exceed several Å. Too small a wavelength, however, leads to constructive interference for countless angles θ as $\Delta\ell = n\lambda$, yielding the diffraction pattern useless. Consequently, X-rays of wavelengths $\lambda \sim 1$ Å are employed for crystallography purposes, hence the name X-ray diffraction.

Grazing incidence X-ray diffraction

For typical X-ray energies of $h\nu = 8.05$ eV absorption is generally low. For the YH_y and YO_xH_y film thicknesses of $d = 100(3)$ nm considered in this research, normal X-ray incidence would result in a theoretical film transmittance exceeding 99% [53]. This implies

that the vast majority of radiation is not being scattered by the film but rather by the substrate, yielding a noise-predominant signal.

To maximise the scattering volume in the YO_xH_y films whilst minimising scattering from the substrate a *grazing incidence* (GI) geometry is used, as depicted in Figure 3.9. By fixing the X-ray tube at a small angle ω with respect to the sample surface the optical path length in the film is greatly enhanced as $d_{\text{X-ray}} = d/\sin\omega$. For an angle $\omega = 2.0°$, for instance, the film thickness encountered by the incident wave is increased by a factor of almost 30, now yielding a theoretical X-ray transmittance of less than 1% [53].

By moving the detector over the circumference of a semi-circle centred around the sample surface, a grazing incidence X-ray diffraction (GIXRD) pattern is obtained. The scattering angle is twice the Bragg angle θ (Figure 3.8) and the diffraction pattern is thus a function of 2θ. To maximise the film surface subjected to the beam a slightly divergent incident beam is used, controlled by a slit behind the tube. A 0.02° Soller slit collimator is placed in front of the detector to ensure only X-rays scattered at exactly 2θ contribute to the detected signal.

3.2.2 Diffractometer

The used diffractometer is a Bruker D8 Discover equipped with a ceramic copper (Cu) X-ray tube of type KFL-Cu-2K. X-rays are created by accelerating electrons evaporated from a tungsten (W) filament towards a 60 kV bias Cu target anode, causing excitation of core electrons from the Cu K shell (1s orbital) to the second L shells ($2p_{3/2}$ and $2p_{1/2}$ orbitals). Once they relax they undergo a 2p–1s transition, emitting Cu Kα X-rays of wavelengths $\lambda_{\text{Cu}}^{\text{K}\alpha_1} = 1.5406$ Å and $\lambda_{\text{Cu}}^{\text{K}\alpha_2} = 1.5444$ Å for the $2p_{3/2}$–1s and $2p_{1/2}$–1s transitions, respectively.

Scattered X-rays are converted to a digital signal using a semiconducting silicon strip Lynxeye XE detector. Incident X-rays create a number of electron–hole pairs proportional

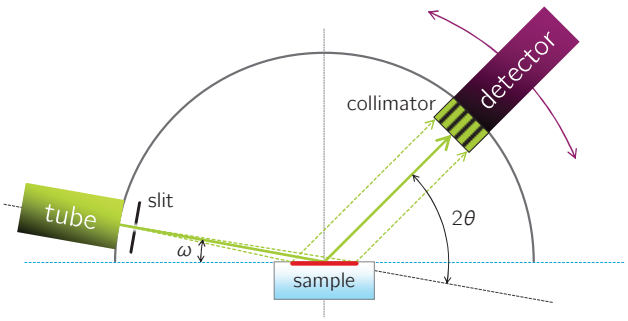

Figure 3.9. Grazing incidence X-ray diffraction (GIXRD) configuration increasing the diffraction yield for thin films. Using small incident X-ray angles ω the film depth encountered by the X-ray beam is greatly enhanced, increasing the signal from the film and reducing substrate noise. The detector is rotated over angles 2θ to obtain the diffraction pattern.

to the X-ray energy, which are separated by an electric field to induce a current between the collector electrodes. The current is a direct measure of the incident intensity.

The tube is kept at an angle of $\omega = 2.0°$. Smaller angles result in a beam wider than the 10 mm × 10 mm substrate and hence a loss of intensity and increased noise, and larger angles lead to decreased film scattering volumes also yielding increased noise from the substrate. The detector is moved by 0.4° increments every 245 seconds between $26.5° \leq 2\theta \leq 36.5°$, to scan the angles surrounding the literature values of 28.7°–29.7° corresponding to YH_y and YO_xH_y Cu Kα$_1$ (1 1 1) reflections [12, 33]. Although a larger 2θ range would give more information on the positions of e.g. the (2 0 0) and (2 2 0) peaks, the single (1 1 1) peak contains sufficient information on the lattice size and the focus is therefore on this single highest-intensity peak to determine the influence of deposition pressure on the lattice size.

3.2.3 Lattice parameter

After subtraction of background noise, the $2\theta_{111}$ peak position values of the (1 1 1) reflections are to be converted to the fcc lattice parameter a using Bragg's law:

$$a = d_{111}\sqrt{3} = \frac{n\lambda\sqrt{3}}{2\sin\theta_{111}}, \tag{3.1}$$

setting $n = 1$ as this corresponds to the largest lattice periodicity and hence the unit cell size for fcc structures. The exact determination of the $2\theta_{111}$ peak position from the diffractogram requires some analysis however (see Figure 3.10).

In perfect monocrystalline solids, two separate peaks resulting from scattering of both Kα$_1$ and Kα$_2$ radiation might be distinguished due to a slight mismatch of the corresponding Bragg angles. A first approximation for the mutual peak centres displacement is $\delta 2\theta_{111} = 2\theta_{111}^{K\alpha_2} - 2\theta_{111}^{K\alpha_1} = 2\arcsin\left(\lambda_{Cu}^{K\alpha_2}\sqrt{3}/2a\right) - 2\arcsin\left(\lambda_{Cu}^{K\alpha_1}\sqrt{3}/2a\right) \approx 0.07°$ for literature YH_y and YO_xH_y lattice parameters of 5.3–5.4 Å [12, 33]. In polycrystalline solids the diffraction peaks are however broadened as a whole distribution of slightly rotated or expanded crystallites also contribute to scattering. This generally results in a single broad diffraction peak.

To distinguish between the Kα$_1$ and Kα$_2$ components the scattering intensity $I(2\theta) = I_1(2\theta) + I_2(2\theta)$ is fitted as the sum of two pseudo-Voigt peak functions, each consisting of a linear combination of a Lorentzian and a Gaussian component:

$$I_i(2\theta) = A_i\left[m_L\frac{2}{\pi}\frac{w}{4(2\theta - 2\theta_i^c)^2 + w^2} + (1 - m_L)\frac{\sqrt{4\ln 2}}{\sqrt{\pi}w}e^{-\frac{4\ln 2}{w^2}(2\theta - 2\theta_i^c)^2}\right],$$

where m_L is the Lorentzian–Gaussian weight parameter, w is the width of the distributions, $2\theta^c$ is the peak centre position, and A is an intensity scale factor. Each separate peak

is assigned to a single Kα component and is thus centred around a different $2\theta^{c}$ value, i.e. $2\theta_2^c - 2\theta_1^c = \delta 2\theta_{111}$. As both curves are a result of scattering from the same crystal their shapes are identical, hence m_L and w are shared. The intensity ratio between Kα1 and Kα2 is 1:0.518 so $A_1 = 1.93A_2$ [54]. This leaves four independent variables A_1, m_L, w and θ_1^c to fit the curve. The resulting value of θ_1^c is set as θ_{111} in equation 3.1 to obtain a new approximation for the lattice parameter a from $\lambda_{Cu}^{K\alpha_1}$ radiation. From this new a an updated value of $\delta 2\theta_{111}$ is computed and reincorporated into the fit constraints to obtain a new $2\theta_1^c$ peak centre position. This iterative process is continued until the lattice parameter a is determined to within 0.001 Å accuracy, obtained within one or two iterations.

The GIXRD refractive error at an incidence angle $\omega = 2.0°$ yields an offset of +0.005° in the measured 2θ values with respect to their actual values. Due to an axial divergence of the X-ray beam 2θ values in the range 29°–30° are offset by approximately –0.019°. The obtained (1 1 1) diffraction peak position is therefore corrected by a shift of +0.014°.

The main error sources are the goniometer, accurate to within 0.001°, and the fit itself. By changing the fitting data range a spread of $2\theta^{c}$ values of up to ~0.02° are obtained, and an uncertainty of $\Delta\theta_{111} \approx 0.01°$ is therefore used. This results in a lattice constant margin of error of

$$\Delta a = \left|\frac{\partial a}{\partial \theta_{111}}\right| \Delta\theta_{111} = \frac{n\lambda\sqrt{3}}{2} \frac{\cos\theta_{111}}{\sin^2\theta_{111}} \Delta\theta_{111},$$

yielding $\Delta a = 0.014$ Å for $2\theta_{111}$ values of 29°–30°.

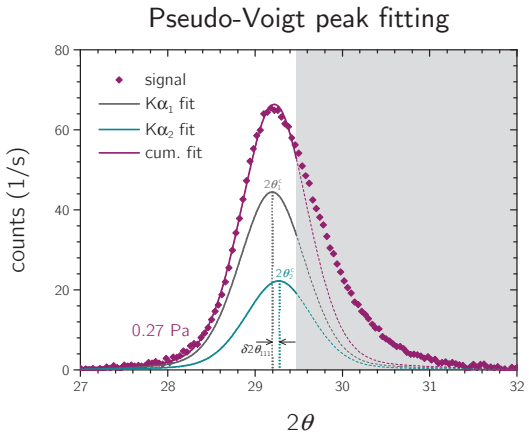

Figure 3.10. GIXRD (1 1 1) diffraction peak for a 100 nm-thick untransformed YH_y film sputter-deposited at 0.27 Pa. To determine the lattice parameter the peak is fitted as a linear combination of two separate pseudo-Voigt functions (of the same shape), resulting from scattering of Cu Kα1 and Kα2 radiation. The peak centres are displaced by $\delta 2\theta_{111}$ and the mutual intensity ratio is set to 1:0.518. The lattice parameter is calculated from the $2\theta_1^c$ peak position and equation 3.1. Due to asymmetry of the diffraction peak only the blank θ range is used for fitting.

3.3 Photospectrometry

The optical properties of the sputter-deposited samples are quantified by measurement of the transmittance and reflectance of EM radiation as a function of wavelength, referred to as photospectrometry. From the spectral transmittance $T(\lambda)$ and reflectance $R(\lambda)$ the absorption coefficients $\alpha(\lambda)$ are obtained from which film band gaps are determined using the Tauc plot method. The average transmittance under UV illumination is monitored to study photochromic darkening. UV transparencies are used to quantify oxidation susceptibility using the two-layer Y_2O_3–YO_xH_y film model.

3.3.1 PHOCS setup

Uniform samples

Photospectrometry studies are conducted using the PHOCS 2.0 setup shown in Figure 3.11, designed and built by dr. Steffen Cornelius. An Ocean Optics DH-2000-BAL deuterium–halogen UV–VIS–NIR light source emits a beam of intensities $I_0(\lambda)$ towards the sample. A 50%–50% beam splitter is inserted between the light source and the sample stage for reflectance measurements. As a result the sample is subjected to an incident beam $I_\mathrm{i}(\lambda) \approx 0.5 I_0(\lambda)$. A fraction $I_T(\lambda)$ is transmitted through the sample and recorded by an Ocean Optics HR4000 detector. Another fraction $I_R^\circ(\lambda)$ is reflected by the film surface, and in part diverted by the beam splitter towards a second identical detector where a signal $I_R(\lambda)$ is recorded. All spectra are recorded with a resolution of at least 0.5 nm.

The spectral transmittance $T(\lambda)$ is computed from the recorded intensity $I_T(\lambda) = T(\lambda) I_0(\lambda)$ relative to the $I_\mathrm{ref}^T(\lambda) = I_0(\lambda)$ reference in the absence of a sample (i.e. 100% transmittance). To correct for any stray light, a *dark* spectrum $I_\mathrm{d}^T(\lambda)$ is also recorded with the $I_0(\lambda)$ beam blocked. The spectral transmittance $T(\lambda)$ is thus

$$T(\lambda) = \frac{I_T(\lambda) - I_\mathrm{d}^T(\lambda)}{I_\mathrm{ref}^T(\lambda) - I_\mathrm{d}^T(\lambda)}. \tag{3.2}$$

The spectral reflectance $R(\lambda)$ is obtained in a similar manner, yet different configurations are required to obtain the dark and reference spectra $I_\mathrm{d}^R(\lambda)$ and $I_\mathrm{ref}^R(\lambda)$. As zero reflectance implies no detected signal from the light source, $I_\mathrm{d}^R(\lambda)$ is recorded by blocking the beam I_T between the sample and the top detector using a black diffuse surface. Not blocking the beam would result in reflectance from the transmittance detector which would in turn be recorded by the reflectance detector, not quite corresponding to zero reflectance. The reflectance reference spectrum $I_\mathrm{ref}^R(\lambda)$ is recorded by inserting a reference mirroring surface at the sample position. Although no surface is a perfect mirror over entire such wavelength ranges, the reflectance $R_\mathrm{ref}(\lambda)$ of the reference mirror is known such that a 100%

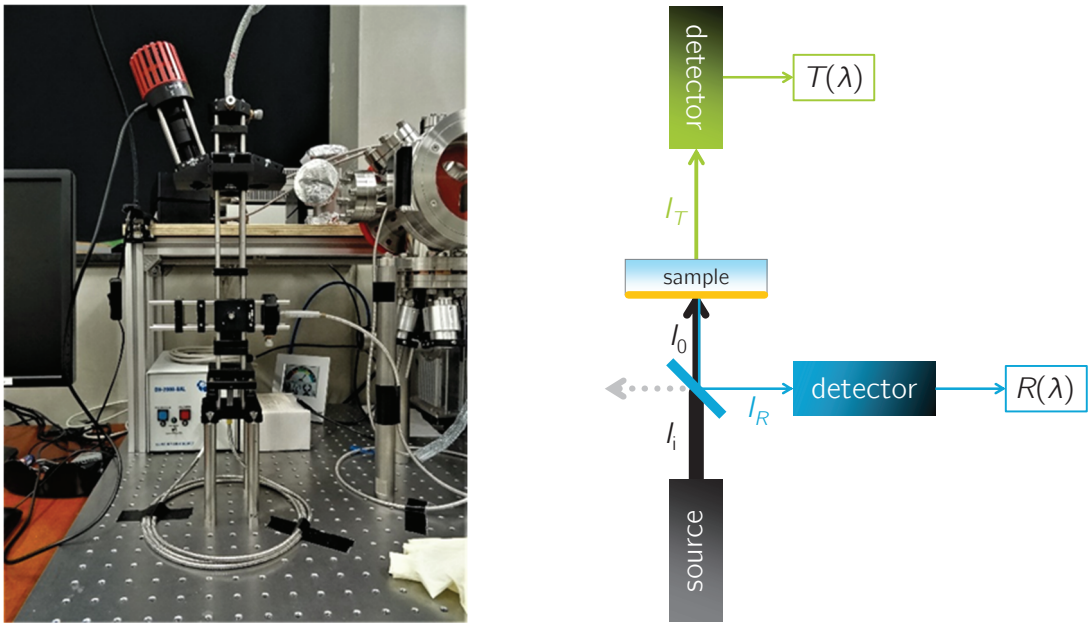

Figure 3.11. PHOCS 2.0 photospectrometry setup to measure transmittance and reflectance of a sample. The sample is illuminated by radiation covering a broad wavelength range. The incident beam I_0 is partly transmitted (I_T) and converted to the spectral transmittance $T(\lambda)$. The reflected beam is diverted to a detector by a beam splitter to obtain the spectral reflectance $R(\lambda)$.

reflectance is given by $I^R_{100\%}(\lambda) = I^R_{\text{ref}}(\lambda)/R_{\text{ref}}(\lambda)$. The spectral film reflectance is therefore given by

$$R(\lambda) = \frac{I_R(\lambda) - I^R_{\text{d}}(\lambda)}{I^R_{\text{ref}}(\lambda)/R_{\text{ref}}(\lambda) - I^R_{\text{d}}(\lambda)}.$$

All measurements are conducted in a dark room. Data acquisition is executed using LabVIEW-based PHOCS software programmed by Bart Boshuizen, and data is analysed with IE OriginPro 9.0.

Repetitive measurements of $T(\lambda)$ on the same sample, manually repositioning the sample and renewing the reference spectra $I^T_{\text{d}}(\lambda)$ and $I^T_{\text{ref}}(\lambda)$, yield absolute variations in $T(\lambda)$ of up to $u(T) \lesssim 0.5\%$. Similar measurements of $R(\lambda)$ result in much higher absolute deviations of up to $u(R) \lesssim 15\%$. This is mainly due to sensitive focusing of the reflected beam—slight angular deviations of the reflected beam may result in substantial deviations as it arrives at the detector. As the same accounts for the acquisition of $I^R_{\text{ref}}(\lambda)$, the resulting uncertainties are unfortunately large. Reflectance measurements are considered reasonable if the resulting $T(\lambda) + R(\lambda) < 1$, i.e. $A(\lambda) > 0$ for all wavelengths, generally yielding an uncertainty of $u(R) \lesssim 5\%$.

Gradient samples

Due to the 76 mm × 26 mm size of the gradient samples these cannot be analysed using the PHOCS 2.0 setup as the rods surrounding the sample stage are too narrowly-spaced.

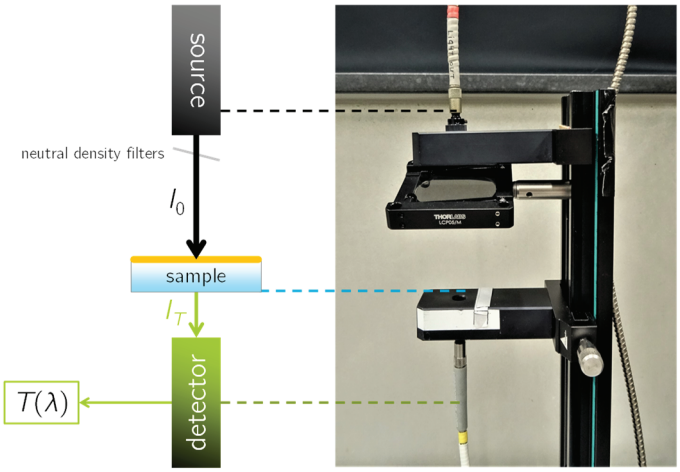

Figure 3.12. PHOCS 1.0 photospectrometry setup. The spectral transmittance $T(\lambda)$ of a sample is computed from the measured transmitted intensity I_T.

Instead, the old PHOCS 1.0 setup is used, pictured in Figure 3.12. This setup is only equipped with a single detector to measure the spectral transmittance. For determination of the band gap and monitoring of the darkening behaviour this is generally sufficient. Neutral density filters are placed beneath the light source to reduce the light intensity and prevent photodarkening of the samples during measurement.

$T(\lambda)$ is also obtained using equation 3.2, with $I_{\mathrm{d}}^{T}(\lambda)$ the measured signal with the light source blocked and $I_{\mathrm{ref}}^{T}(\lambda)$ with the light source completely unblocked.

To obtain reproducible measurements on well-defined positions on the gradient films the samples are embedded in a sliding holder as depicted in Figure 3.13a. The sliding holder is inserted into a cartridge (Figure 3.13b) mounted onto the sample stage, in which it can freely move along the sample length direction. A marker on the sliding holder moves with respect to a 0.5 mm scale to allow for accurate positioning and reproducibility of the measurements. Yet, the spatial resolution is limited by the beam spot size of ~0.5 cm.

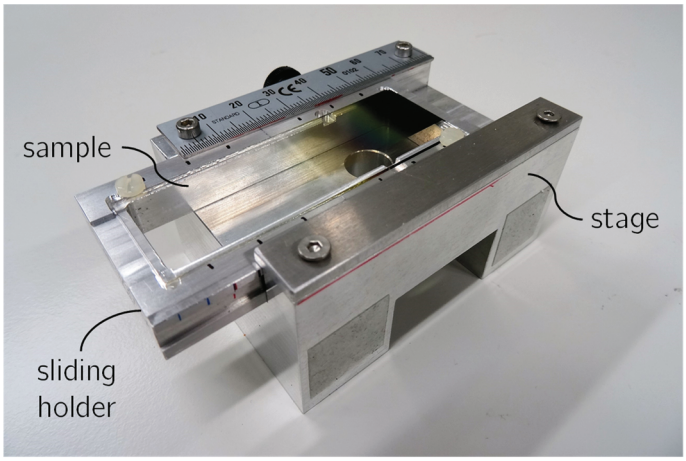

Figure 3.13. Sliding holder and stage used in addition to the PHOCS 1.0 setup (Figure 3.12) for transmittance measurements on the gradient samples, allowing for accurate positioning of the sample along the sample length direction.

3.3.2 Photodarkening

The extent of photochromic darkening of the samples in response to UV illumination is quantified using the average transmittance $\bar{T}$, i.e. $T(\lambda)$ averaged over 450–1000 nm VIS–NIR wavelengths. Lower wavelengths are excluded as absorption of lower wavelengths is high and transmittance is low, independent of the state of the films. $\bar{T}(t)$ is monitored *ex situ* as a function of UV illumination time t by briefly interrupting film illumination to measure $T(\lambda)$ and, if possible, $R(\lambda)$, at 5–30 min intervals.

Two-sided LW–LW UV illumination

The uniform samples are illuminated using two Herolab UV hand lamps of type UV-12 L labelled HL-2 and HL-3, each fitted with two 6 W long-wavelength (LW) elongated gas discharge tubes. The lamps are positioned as depicted in Figure 3.14, facing each other and separated by 4.0 cm. The sample holder is inserted between the lamps and allows for two-sided illumination of the samples from front and back. Two rulers are used for accurate positioning and alignment of the sample holder. Up to two samples are placed in the sample holder as indicated by the blue circles, at equal distances (2.0 cm) from the lamps' centres to obtain (roughly) equal intensities. The films are facing the top HL-3 lamp.

The spectral lamp intensities at the position of the samples are measured using an Ocean Optics USB2000+ detector, and given in Figure 3.15. As the top light bulbs are newer than the bottom bulbs their intensities are considerably higher. The corresponding absolute irradiances are 5.3 mW/cm^2 and 2.1 mW/cm^2, respectively, comparable to 300–400 nm AM1.5 solar irradiance of 4.6 mW/cm^2 [66].

The intensity–depth profiles corresponding to two-sided illumination of the pressure series samples are computed from the absorption coefficients at 350 nm, and shown

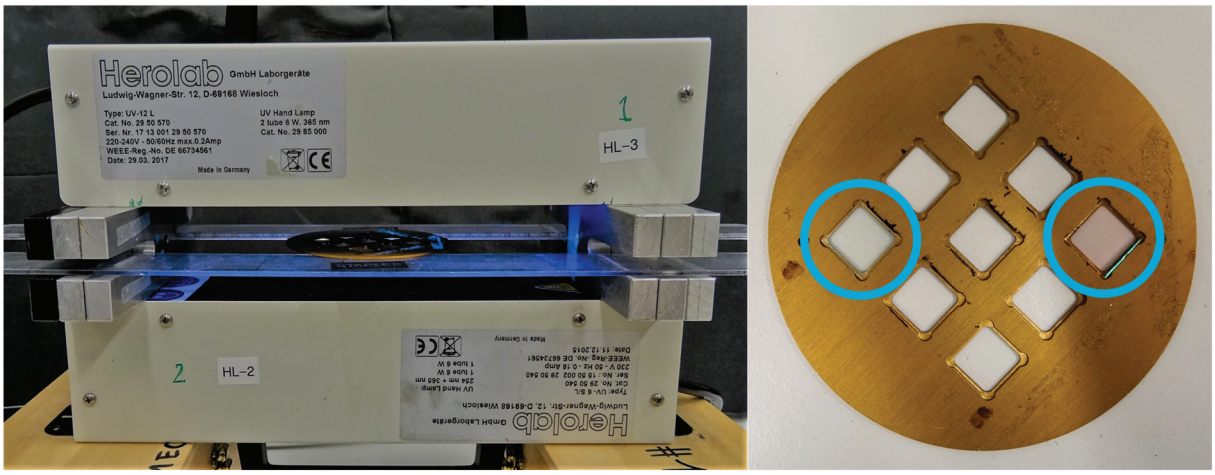

Figure 3.14. Setup used for two-sided (front and back) UV illumination of the 10 mm × 10 mm uniform samples. Up to two samples are inserted at the sample holder positions indicated by the blue circles (right) such that they are at equal distances from the centre of the lamps (coinciding with the centre position on the holder), with the films facing upwards. This way the samples are subjected to roughly equal UV intensities (see Figure 3.17b). The sample holder is positioned between the lamps on two linear scales.

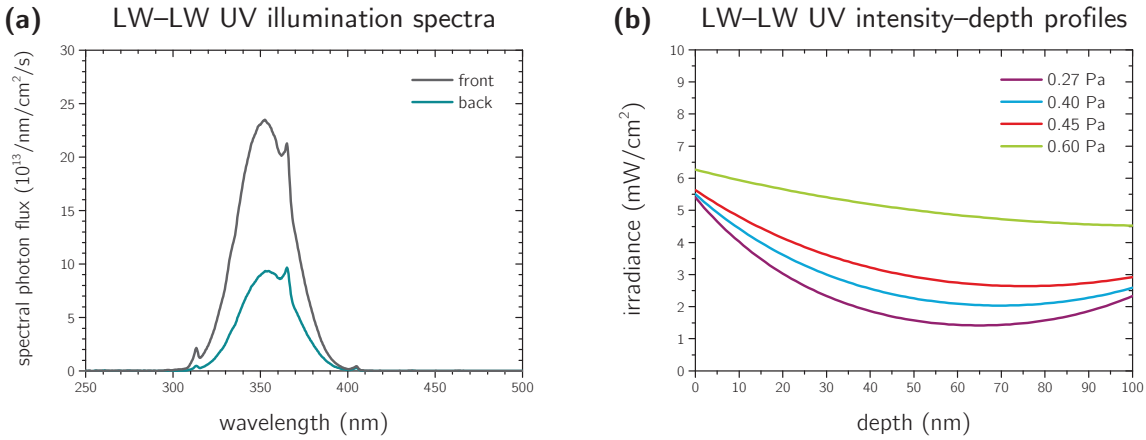

Figure 3.15. UV intensities corresponding to the two-sided illumination setup of Figure 3.14.
(a) Spectral irradiances $I(\lambda)$ incident on the samples. As the films are faced upwards, the *front* spectrum corresponds to the top lamp (HL-3), and the *back* spectrum to the bottom lamp (HL-2) irradiating the substrates.
(b) Resulting intensity–depth profiles for each of the films deposited at varying pressures, computed from the spectral irradiances of figure (a) and the absorption coefficients at 350 nm corresponding to the maximum intensities.

in Figure 3.15b. Contrary to single-sided illumination, the specific setup allows for a somewhat uniform intensity profile such that the entire films are subjected to photodarkening, potentially increasing contrast and darkening speed.

Single-sided MW–MW UV illumination

Elongated 76 mm × 26 mm gradient samples are photodarkened using a single Herolab UV-12 L hand lamp labelled HL-1, fitted with two medium-wavelength (MW) tubes (Figure 3.16). The vertical lamp–sample distance is 2.5 cm, resulting in a spectral irradiance as depicted in Figure 3.17a. A single sample is positioned along the length axis centred

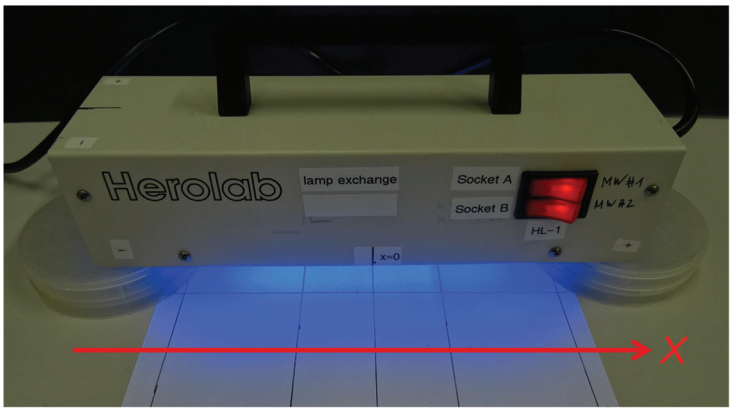

Figure 3.16. Setup used for single-sided MW–MW UV illumination of elongated 76 mm × 26 mm gradient samples. A single sample is placed along the x-axis at 2.5 cm underneath the lamp, centred around $x = 0$ with the film facing the lamp.

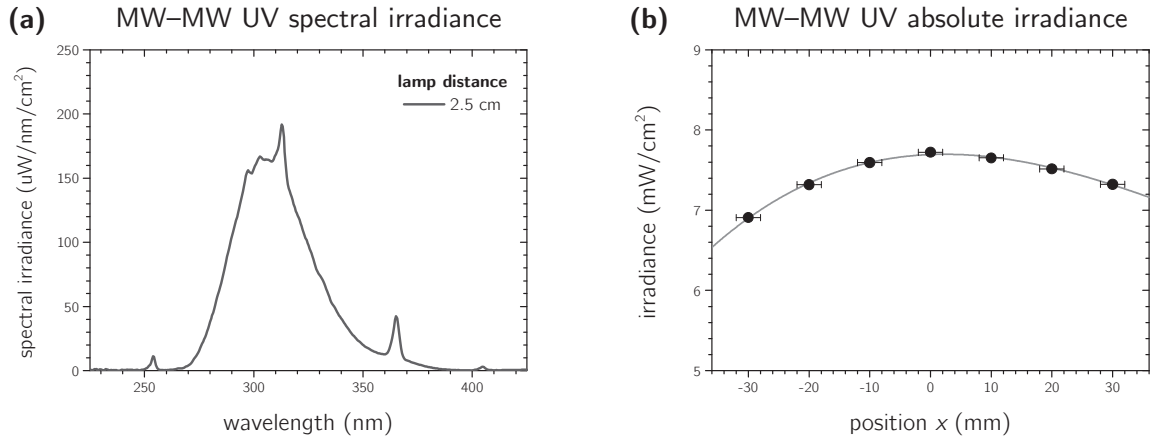

Figure 3.17. (a) Spectral MW–MW UV irradiance $I(\lambda)$ at $x = 0$ in the setup of Figure 3.16, and **(b)** the absolute irradiance I as a function of sample position x.

around $x = 0$ with the film upwards. The intensities encountered at varying sample positions vary over the length axis and are shown in Figure 3.17b.

3.3.3 Tauc plot method

A conventional technique for the determination of the band gap of semiconducting thin films is through a *Tauc plot* [55]. It has been established that the optical absorption edge of a semiconductor is of the form

$$\alpha h\nu \propto \left(h\nu - E_\mathrm{g}\right)^m,$$

with $m = 1/2$ for a direct band gap and $m = 2$ for an indirect band gap material [45, 55]. Plotting $(\alpha h\nu)^{1/m}$ as a function of photon energy $h\nu$ thus yields a linear curve at the absorption edge as $(\alpha h\nu)^{1/m} \propto \left(h\nu - E_\mathrm{g}\right)$. By extrapolating the linear absorption edge towards $(\alpha h\nu)^{1/m} \to 0$, the band gap is obtained from the intersect with the energy axis as $h\nu - E_\mathrm{g} \to 0$. All that is required for band gap determination are thus the absorption coefficient as a function of photon energy $\alpha(h\nu)$—i.e. $\alpha(\lambda)$—and m. For photochromic $\mathrm{YO}_x\mathrm{H}_y$, $m = 2$ as it has an indirect band gap [13, 17].

$\alpha(\lambda)$ is determined from the spectral transmittance $T(\lambda)$ and reflectance $R(\lambda)$ using a rearrangement of the Lambert–Beer law (equation 2.2):

$$\alpha(\lambda) = \frac{1}{d}\ln\left(\frac{I_{1-R}(\lambda)}{I_T(\lambda)}\right).$$

As the incident intensity is $I_{1-R}(\lambda) = \big(1 - R(\lambda)\big)I_0(\lambda)$ and the transmitted intensity is $I_T(\lambda) = T(\lambda)I_0(\lambda)$, this yields a spectral absorption

$$\alpha(\lambda) = \frac{1}{d}\ln\left(\frac{1 - R(\lambda)}{T(\lambda)}\right).$$

An example is given for a day-old 100 nm-thick YO_xH_y film on f-SiO_2 sputter-deposited at a pressure of 0.45 Pa. The spectral transmittance $T(\lambda)$ and reflectance $R(\lambda)$ are shown in Figure 3.18a. The calculated absorption coefficients $\alpha(\lambda)$ are converted to $\alpha(h\nu)$ to generate the Tauc plot $(\alpha h\nu)^{1/2}$ as a function of photon energy $h\nu$ shown in Figure 3.18b. Extrapolation of the linear part of the Tauc plot yields an intercept with the energy axis of 2.39(3) eV, i.e. the band gap.

Statistical errors from the linear fit are generally of the order of several 0.001 eV, but can also be larger. Additional uncertainties associated with variations between chosen fitting data ranges are some 0.01 eV. The resulting error margin are thus at least 0.01 eV.

As no $R(\lambda)$ data is acquired for the gradient samples, band gaps are determined by assuming $R = 0$. To illustrate the influence of $R(\lambda)$ on band gap determination, the Tauc plot of Figure 3.18b is compared to a Tauc plot obtained from solely $T(\lambda)$ (Figure 3.19). The difference between resulting band gap values is approximately 0.005 eV for this particular film thickness. Although it is *coincidentally* rather low, one can observe the influence of interference shifts on the linear part of the Tauc plot—it is at lower energies and the slope is considerably steeper. For more inconvenient interference configurations the difference could well be over 0.1 eV, as observed in the band gap gradient of Figure C-2d. The drop between the band gaps of two neighbouring positions $x = -30$ mm and $x =$

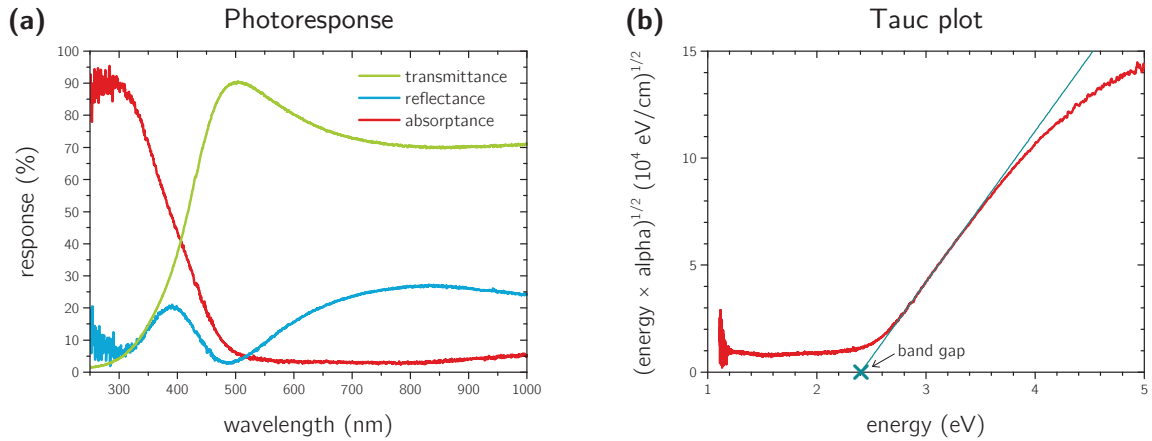

Figure 3.18. Band gap determination using the Tauc plot method for a day-old 100 nm-thick YO_xH_y film sputter-deposited at 0.45 Pa.
(a) Measured spectral transmittance $T(\lambda)$ and reflectance $R(\lambda)$, and resulting absorptance $A(\lambda) = 1 - T(\lambda) - R(\lambda)$.
(b) Associated Tauc plot. The intersect with the energy axis of the extrapolated linear part of the plot corresponds to the band gap.

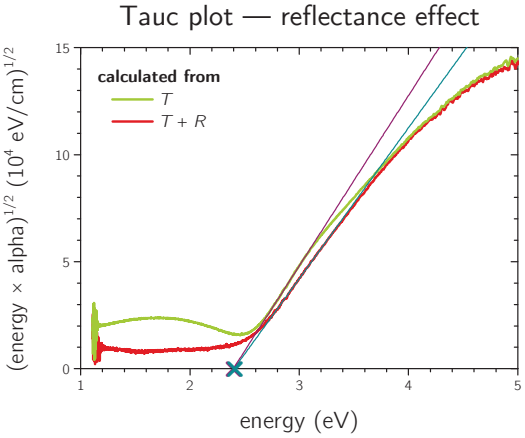

Figure 3.19. Effect of reflectance on the Tauc plot. For absorption coefficients computed solely from the transmittance $T(\lambda)$ the resulting Tauc plot displays interference oscillations which are absent when considering the reflectance $R(\lambda)$. This may influence the determined band gap. Although for this specific sample the resulting band gaps are coincidentally very similar, large errors may arise for more inconvenient interference fringes.

−20 mm is 0.16 eV, whereas the general trend would suggest it to be only several 0.01 eV. Although arbitrary, the minimum band gap uncertainties for the gradient samples are therefore determined as to accommodate for fluctuations between neighbouring positions. For the DyO_xH_y–YO_xH_y gradient sample (Figure 4.10b) this results in band gap uncertainties of at least 0.15 eV.

3.3.4 Two-layer film model

As most materials, the surface of YO_xH_y readily oxidises in air to form a non-photochromic oxide layer, i.e. yttria (Y_2O_3). Due to its band gap of 5.6 eV yttria is transparent to UV radiation. Oxidation of YO_xH_y to form yttria thus yields an increase in UV transparency.

To quantify the extent of yttria growth at the expense of photochromic YO_xH_y the films are modelled as a two-layer film—a UV-absorbing YO_xH_y film covered by a UV-transparent yttria layer. UV absorption is then solely characterised by the YO_xH_y layer of some thickness $d°$. The transmitted intensity I_T° of incident UV radiation of intensity I_0 (or rather $(1-R)I_0$, see section 2.4.2) is given by the Lambert–Beer law (equation 2.2):

$$I_T^\circ = I_0 e^{-\alpha d^\circ},$$

where $\alpha = \alpha(\lambda)$ is the absorption coefficient. The corresponding intensity–depth profile is shown in Figure 3.20a. Upon oxidation of YO_xH_y, the yttria layer grows while the YO_xH_y thickness is reduced by some Δd_{ox} (Figure 3.20b). Assuming that α remains unaffected, this yields a transmitted intensity $I_T = I_0 e^{-\alpha(d^\circ - \Delta d_{ox})} = I_T^\circ e^{\alpha \Delta d_{ox}}$ such that $\Delta d_{ox} =$

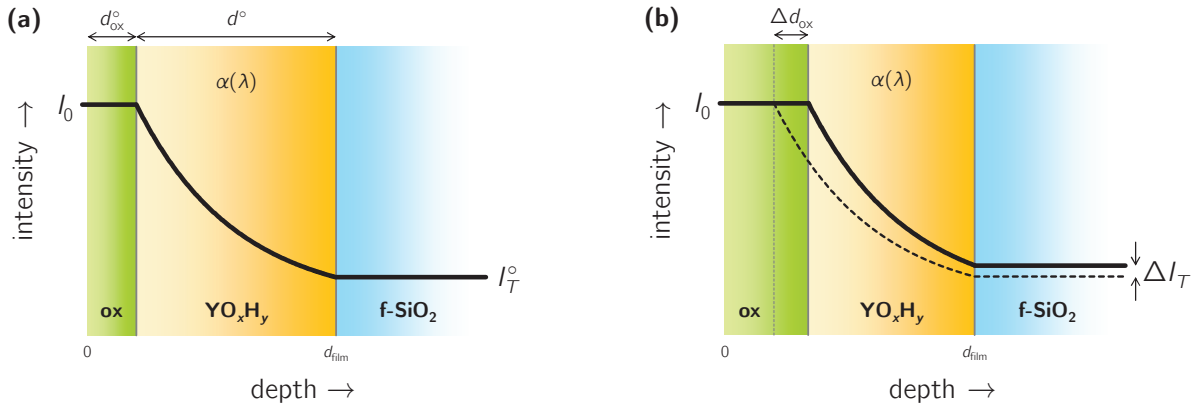

Figure 3.20. Determination of the extent of oxide layer growth $\Delta d_{ox}/d^\circ$ using the two-layer film model.
(a) The initial YO_xH_y thickness d° and oxide layer thickness d°_{ox} (within half an hour of post-deposition oxidation) yield a transmitted intensity I°_T.
(b) Yttria growth Δd_{ox} due to ageing leads to an YO_xH_y thickness reduction of $\Delta d = -\Delta d_{ox}$, resulting in an increased transmitted intensity $\Delta I_T = I_T - I^\circ_T$. $\Delta d_{ox}/d^\circ$ is computed from $T = I_T/I_0$ and $T^\circ = I^\circ_T/I_0$ using equation 3.3.

$\ln(I_T/I^\circ_T)/\alpha$. Reorganising the Lambert–Beer law gives $\alpha = -\ln(I^\circ_T/I_0)/d^\circ$ and therefore $\Delta d_{ox}/d^\circ = -\ln(I_T/I^\circ_T)/\ln(I^\circ_T/I_0)$. Considering that the transmittance is given by $T = I_T/I_0$ the relative oxide layer thickness increase is given by $\Delta d_{ox}/d^\circ = -\ln(T/T^\circ)/\ln(T^\circ) = -\ln(T)/\ln(T^\circ) + \ln(T^\circ)/\ln(T^\circ)$. This yields a relative oxide layer growth

$$\frac{\Delta d_{ox}}{d^\circ} = 1 - \frac{\ln T}{\ln T^\circ}. \tag{3.3}$$

Although it is impossible to determine the initial oxide layer thickness d°_{ox} using this procedure, further yttria formation at the expense of photochromic YO_xH_y is quantified as a function of the YO_xH_y thickness d° immediately after post-deposition oxidation.

3.4 Surface profilometry

Film thickness measurements are conducted using surface profilometry, whereby the surface profile of a moving surface is measured by displacement of a stylus. The film thickness is obtained by measuring the difference between the surface height of the partly uncovered substrate and the film. The used profilometer is a Veeco Dektak 3 with supporting software, with an instrumental accuracy of $\Delta d_{inst} = 10$ Å.

Due to substantial roughness of the interface between the bare substrate and the coating, individual thickness measurements d_i show significant mutual fluctuations. To increase the accuracy of film thickness determination, several thickness measurements d_i

Table 3.1. $t(N)$ distribution table for 97.5% confidence levels, for statistical error calculations corrected for sample size N [57].

$\boldsymbol{N}$	2	3	4	5	6	7	8	9	∞
$\boldsymbol{t(N)}$	12.706	4.303	3.182	2.776	2.571	2.447	2.365	2.306	1.960

are conducted for each specimen to obtain an averaged film thickness $d = \bar{d} = \sum_{i=1}^{N} d_i/N$, where N is the number of measurements.

Due to small sample sizes (N) and unknown standard deviations the thickness distribution is modelled as a t distribution [56]. The associated statistical uncertainty Δd_{stat} is calculated from the standard deviation $\sigma^2 = \sum_{i=1}^{N}\left(d_i - \bar{d}\right)^2/N$, corrected for the limited number of measurements by a sample size factor $t(N)$ for 97.5% confidence levels (Table 3.1). Combining both instrumental and statistical errors Δd_{inst} and Δd_{stat} yields a thickness uncertainty

$$\Delta d^2 = \Delta d_{\text{inst}}^2 + \Delta d_{\text{stat}}^2 = \Delta d_{\text{inst}}^2 + \frac{t(N)}{N}\sum_{i=1}^{N}\left(d_i - \bar{d}\right)^2,$$

generally of the order of ~10% of the film thickness for $N = 3$.

4 Results

4.1 Film growth optimisation

4.1.1 Dihydride–oxyhydride transition

To determine the effect of deposition pressure and the resulting film microstructure on the affinity of reactively sputtered YH_y films to transform to photochromic YO_xH_y upon air exposure, series of 100(3) nm-thick YH_y films were sputter-deposited onto 0.5 mm-thick f-SiO_2 substrates for varying pressures in the range 0.27–0.60 Pa. The resulting air-exposed samples are depicted in Figure 4.1. For the lowest pressure of 0.27 Pa the films are dark opaque, resembling metallic YH_y, whereas for higher pressures 0.40 Pa, 0.45 Pa, and 0.60 Pa, respectively, the films are yellowish and increasingly transparent, thus appearing to have transformed to YO_xH_y.

The as-deposited spectral transmittances $T°(\lambda)$ of the films obtained within half an hour of post-deposition oxidation (Figure 4.2a) support the observations that the low-pressure remains (mostly) YH_y whereas the three transparent high-pressure samples have transformed to YO_xH_y. The optical spectrum of the 0.27 Pa sample shows a low overall transmittance and a transmittance window around 700–750 nm that is typical of YH_y [8, 33], albeit a substantially higher transmittance than reported before due to the low film thickness. The transparent samples show rather high VIS–NIR transmittances, and strong absorption of UV–violet/blue wavelengths below 500 nm which explains their yel-

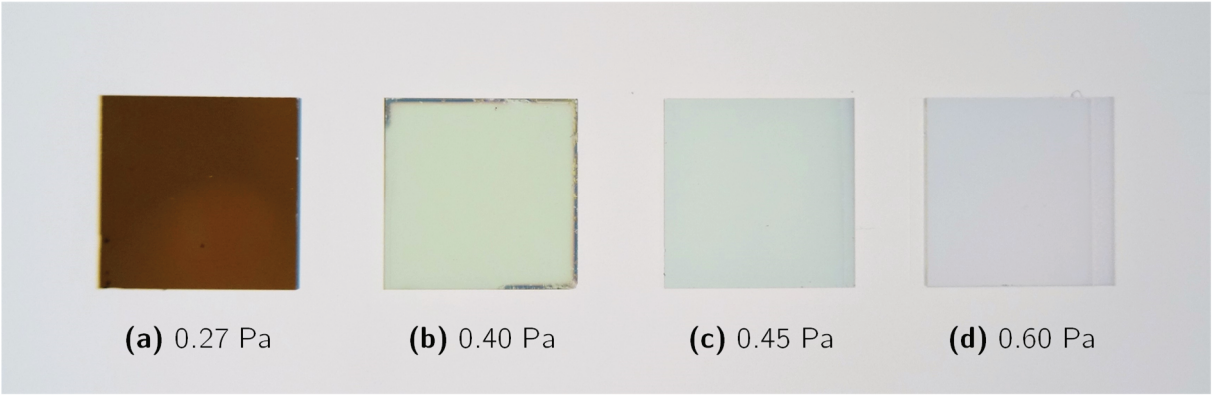

Figure 4.1. Month-old air-exposed 100 nm-thick YH_y films on f-SiO2 substrates, reactively sputtered under pressures of 0.27–0.60 Pa. Sample (a) has a dark opaque appearance resembling that of YH_y. Samples (b–d) are yellowish transparent and have oxidised to form YO_xH_y.

lowish colour and indicates the presence of a band gap as in YO_xH_y. Striking is the significantly lower transmittance of the transparent film grown at 0.40 Pa compared to the higher-pressure samples, a manifestation of the presence of both untransformed dark YH_y and transformed transparent YO_xH_y phases.

The maxima and minima observed around 500 nm and 850 nm wavelengths for the two highest-pressure samples are due to thin-film interference (section 2.4.3).

To further distinguish between metallic YH_y and semiconducting YO_xH_y, film band gaps are determined using the Tauc plot method, of which the resulting values are displayed in Table 4.1 and Figure 4.2b. For the transparent 0.40–0.60 Pa samples the band gaps are in the range 2.25(3)–2.55(3) eV, respectively. The 2.55(3) eV band gap obtained for the 0.60 Pa sample is consistent with earlier observed YO_xH_y band gaps of 2.5–2.7 eV [7, 12, 17], but for the 0.40 Pa and 0.45 Pa samples the band gaps are slightly lower. This may indicate an incomplete YH_y–YO_xH_y transition, especially for the 0.40 Pa sample.

The observed slightly widening YO_xH_y band gaps with deposition pressure indicate increased oxygen content in the transformed YO_xH_y lattice. This is ascribed to facile oxygen penetration for increasingly porous films as the YH_y–YO_xH_y transition is accompanied by widening of the band gap.

The transmittance spectrum of the low-pressure opaque sample (Figure 4.2c) shows two transmittance onsets, indicating the presence of two absorption edges and hence two band gaps as apparent from the Tauc plot in Figure 4.2d. The band gap associated with the YH_y transmittance window at higher wavelengths is substantially lower than those of the transparent samples, as expected for better-conducting material. It is rather high for a metal, though, suggesting that the phases may contain some oxygen. The higher-energy edge is only slightly lower than those of the transparent YO_xH_y samples and fits in the observed band-gap–pressure trend. It appears that the opaque film consists of both YH_y and YO_xH_y phases, evidence that film interiors remain YH_y whereas surface regions have transformed to YO_xH_y.

Air exposure of the half-transparent 0.40 Pa sample for three more days yields an increase of VIS–NIR transmittances, marking a continuation of the YH_y–YO_xH_y transition (Figure 4.3a). For the sample to fully transform therefore takes at least two orders of magnitude longer than for the 0.45 Pa and 0.60 Pa samples, which had (almost) completely transformed within half an hour. The optical properties of the dark low-pressure film are unaffected, thus indicating that this sample remains (mainly) YH_y and oxygen penetration is limited.

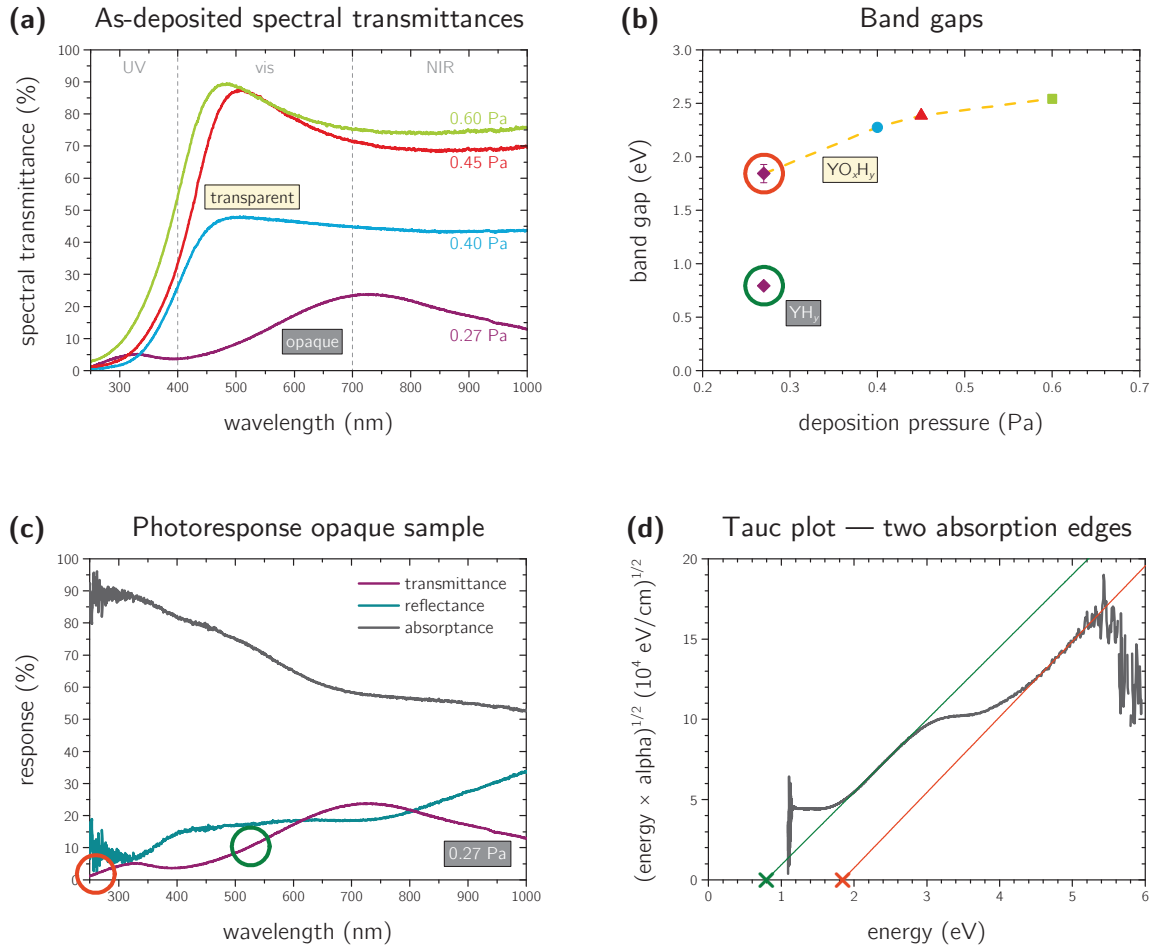

Figure 4.2. As-deposited optical film properties for each of the samples shown in Figure 4.1, obtained within half an hour of post-deposition oxidation. The three yellowish transparent samples are semiconducting and have band gaps resembling those of YO_xH_y. The dark opaque sample appears to consist of YH_y and YO_xH_y, due to its lower overall transmittance and the manifestation of two absorption edges corresponding to semiconducting YO_xH_y and an YH_y transmittance window.

(a) Transmittance spectra $T^\circ(\lambda)$ for varying growth pressures. The three transparent samples show strong UV absorption, and increasing transmittances with pressure due to increased film porosities. The lowest-pressure sample shows a low overall transmittance and a maximum around 700–750 nm wavelengths, typical for metallic YH_y [33].

(b) The band gaps obtained using the Tauc plot method for each of the samples. The dashed yellow line indicates the observed increasing band-gap–pressure trend for semiconducting YO_xH_y. The two band gaps observed for the 0.27 Pa sample indicate the presence of both semiconducting YO_xH_y and metallic YH_y phases.

(c) Transmittance $T^\circ(\lambda)$, reflectance $R^\circ(\lambda)$, and resulting absorptance spectra $A^\circ(\lambda) = 1 - T^\circ(\lambda) - R^\circ(\lambda)$ of the lowest-pressure dark opaque sample. The two transmittance onsets marked by the orange and green circles indicate the presence of two absorption edges.

(d) Tauc plot of the dark opaque sample acquired from the absorptance spectrum of (b). The two linear regions match the two absorption edges, and their extrapolated intersects with the energy axis designate the corresponding indirect band gap values.

The proceeding YH_y–YO_xH_y transition for the 0.40 Pa sample is accompanied by a slight band gap increase from 2.25(3) eV to 2.36(2) eV (Figure 4.3b, Table 4.1), indicating that the band gap is widened by oxygen uptake by the crystal lattice. The slight band gap widening from 2.39(3) eV to 2.41(3) eV observed for the 0.45 Pa sample indicates that it too had not yet fully transformed to YO_xH_y.

To determine the effect of deposition pressure on air-exposed lattice sizes, the 0.27 Pa, 0.40 Pa, and 0.60 Pa films are analysed using GIXRD after several weeks of ageing. The resulting X-ray diffractogram in the range 27°–32° covering known (1 1 1) reflections of YH_y and Y_2O_3 films [12, 22, 33] is shown in Figure 4.4a. One can clearly observe a shift towards lower Bragg angles for increasing pressures and thus increasing lattice sizes. The coloured lines indicate the fitted $2\theta_{111}$ values of the (1 1 1) reflections for Cu Kα_1 radiation. Using Bragg's law and a wavelength of $\lambda = 1.5406$ Å the associated lattice parameters are computed from equation 3.1 and given in Table 4.1 and Figure 4.4b.

The lattice parameters are in the range 5.288(14)–5.413(14) Å, consistent with earlier data on sputter-deposited YH_y and YO_xH_y films with lattice parameters ranging between 5.26–5.39 Å [12, 17]. The crystal lattice is expanded for increasing deposition pressures, and band gaps increase with lattice size. Data on photochromic DyO_xH_y indicates

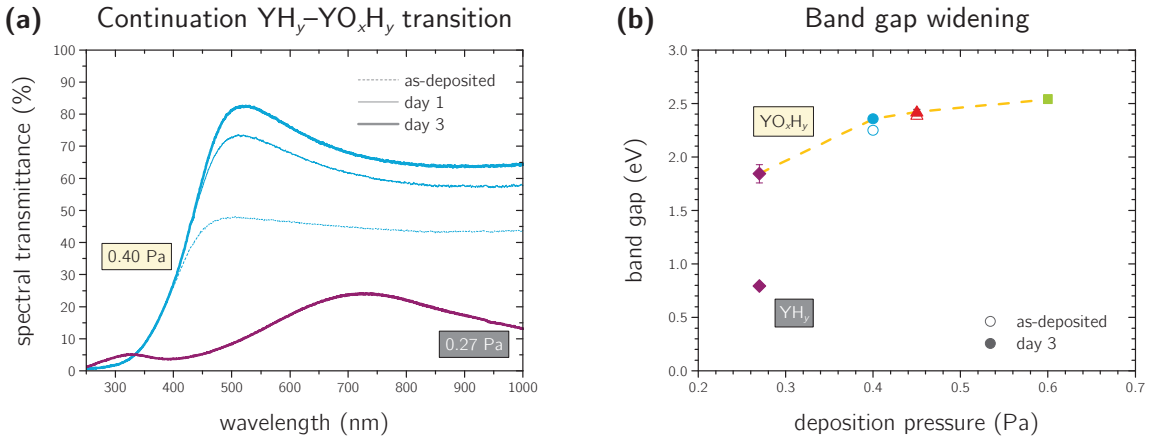

Figure 4.3. Effects of three days of continued air exposure, revealing a continuation of the YH_y–YO_xH_y transition for the 0.40 Pa sample and, to a lesser extent, the 0.45 Pa sample.
(a) The semi-transparent 0.40 Pa sample exhibits a strong increase in VIS–NIR transmittances, marking a proceeding YH_y–YO_xH_y transition. The absence of any transmittance changes for the opaque 0.27 Pa indicates that it remains (predominantly) YH_y.
(b) The continuing YH_y–YO_xH_y transition of the 0.40 Pa sample is accompanied by a widening of the band gap, indicating that oxygen uptake by the lattice yields a larger band gap. The 0.45 Pa sample also exhibits a slight band gap increase, indicating that it had initially not yet fully transformed to YO_xH_y. The 0.60 Pa remains unaffected so it is concluded that it had already fully transformed to YO_xH_y.

Table 4.1. Determined Cu Kα_1 K $2\theta_{111}$ peak centre positions from the GIXRD patterns and computed lattice parameters. Reference values for β-YH_2 and Y_2O_3 are obtained from PDF reference patterns #04-006-6953 and #01-071-0049, respectively. The as-deposited and three-days-old band gaps of Figure 4.3 are also included.

	p_{dep} (Pa)	$2\theta_{111}$ (°)	$\delta\theta_{111}$ (°)	a (Å)	E_g° (eV)	$E_g^{3\,d}$ (eV)	ref.
β-YH_2		29.684		5.2085			[22]
	0.27	29.23(7)	0.0744	5.288(14)	0.80(2) 1.84(9)	0.80(2) 1.84(9)	
Y_2O_3		29.173		5.2979*	5.6		[30, 32]
	0.40	28.85(7)	0.0734	5.356(14)	2.25(3)	2.36(2)	
	0.45				2.39(3)	2.41(2)	
	0.60	28.54(7)	0.0725	5.413(14)	2.55(3)	2.55(3)	

that the larger crystal lattice is due to enhanced oxygen content as the lattice constant increases upon ageing [17]. This indicates that the band gap is widened by increasing oxygen content in the lattice. Whether the crystal lattice is also expanded as a direct result of increasing deposition pressures remains to be seen, but is not expected as the lattice parameters of untransformed DyH_y seem unaffected by deposition pressure [17].

Notable is the lattice of the dark 0.27 Pa sample being slightly smaller than the literature Y_2O_3 lattice while the transparent lattices are larger [30]. This might indicate that Y_2O_3 has the smallest majority-oxygen-containing lattice of the Y–O–H system.

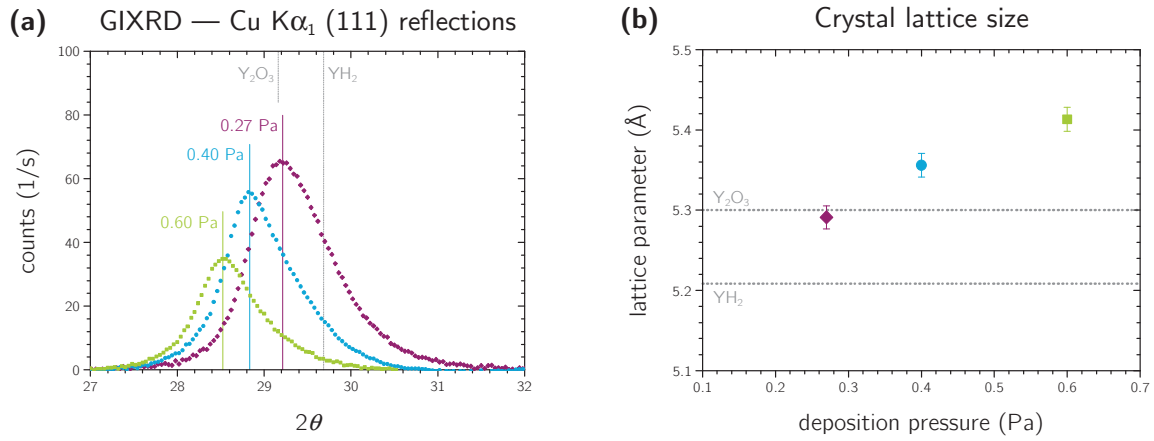

Figure 4.4. Determination of the lattice parameters using GIXRD patterns for three films grown at varying pressures.
(a) GIXRD (1 1 1) reflections and indications of the literature values for β-YH_2 and Y_2O_3. Higher deposition pressures result in a lowering of the Bragg angles. Peak centre positions are determined using pseudo-Voigt peak fitting (section 3.2.3).
(b) Computed lattice parameters, indicating increasing lattice sizes with deposition pressures.

* The bixbyite unit cell of Y_2O_3 actually consists of $2^3 = 8$ cells of $a = 5.30$ Å such that $a = 2 \times 5.30$ Å $= 10.60$ Å (see section 2.1.2).

The asymmetry of the GIXRD curves showing somewhat elongated tails towards higher Bragg angles indicates the presence of smaller crystallites in all three samples. This may point to reduced oxygen content in grain interiors. It appears that oxygen uptake by the lattice is limited to grain exteriors and is therefore facilitated by film porosity and limits to grain size.

The GIXRD intensity reduction with increasing pressures is ascribed to increasing presence of voids and grain boundaries, lacking crystal symmetry and therefore not contributing to the detected signal.

For reactively sputtered metallic YH_y films to exhibit the YH_y–YO_xH_y transition upon air exposure, some minimum critical deposition pressure is required for sufficient film porosity allowing for oxygen penetration into the film. The higher the pressure, the higher the porosity, and the faster the transition. For deposition pressures at or just above the critical pressure the process can take at least several days, whereas for only slightly higher pressures the majority YH_y–YO_xH_y transformation appears to occur instantaneously. This is ascribed to enhanced oxygen penetration in increasingly porous films, exposing larger surface areas to oxygen and increasing the volume fraction of transformed material.

Oxygen uptake by the crystal lattice is accompanied by widening of the band gap, and appears to be responsible for the observed lattice expansion with increasing deposition pressures.

4.1.2 Photochromic contrast

To quantify the effect of deposition pressure and microstructure on the photochromic performance of sputtered YH_y films, the samples of Figure 4.1 are illuminated using the UV irradiance spectra specified in section 3.3.2 whilst tracking their optical response. Four-hour illumination of the 0.45 Pa sample yields a lowering of its VIS–NIR spectral transmittance $T(\lambda)$ as depicted in Figure 4.5a. Figure 4.5b shows the associated intermediate averaged VIS–NIR transmittances $\bar{T}(t)$ over 450–1000 nm wavelengths, as well as those corresponding to the other samples. To eliminate the effects of varying initial transmittances the average values are normalised with respect to their initial average transmittances $\bar{T}_0$ to obtain the normalised photodarkening curves $\bar{T}(t)/\bar{T}_0$ in Figure 4.5c. The resulting normalised contrasts $\Delta\bar{T}/\bar{T}_0$ after four hours of illumination are depicted in Figure 4.5d for each of the samples.

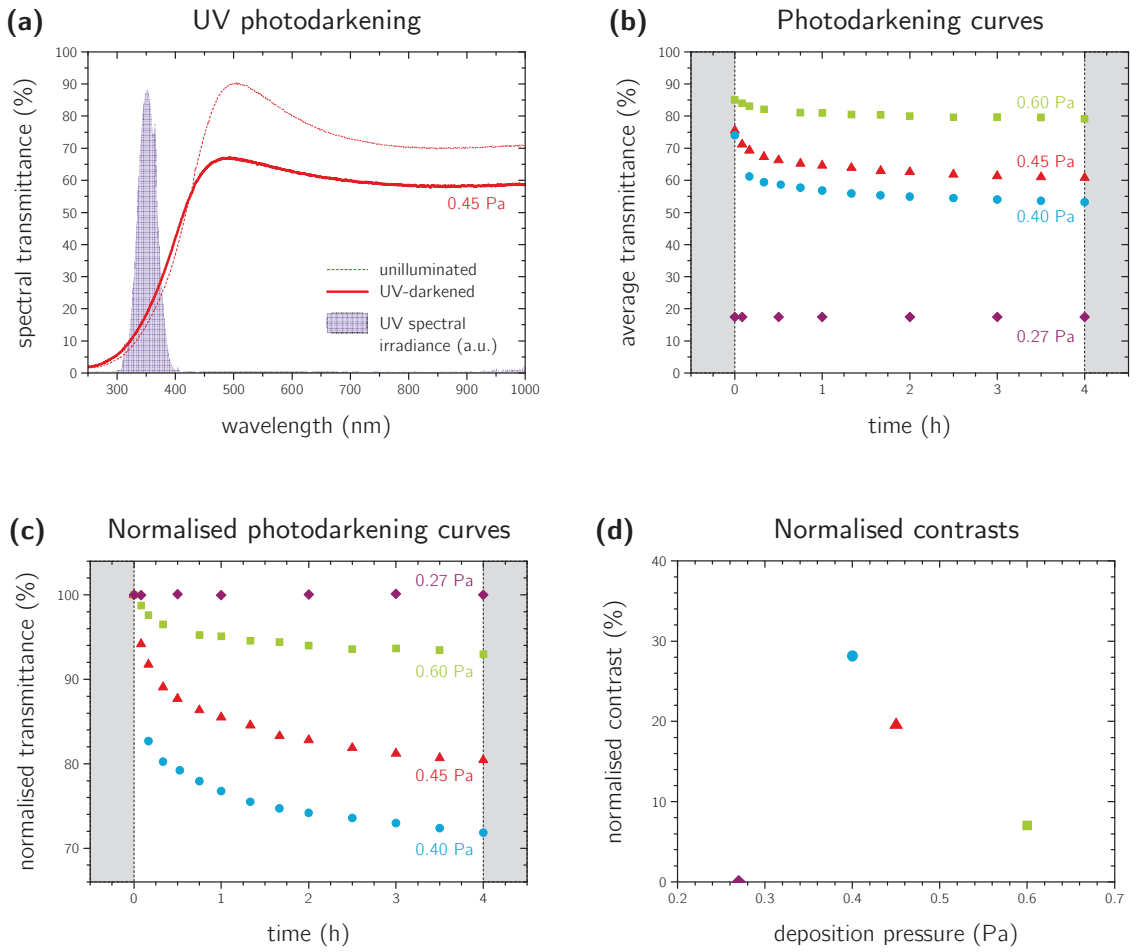

Figure 4.5. Effect of four-hour UV illumination on the optical properties of the exposed films. The low-pressure YH_y sample does not darken upon UV exposure and is therefore not photochromic, while the three transparent YO_xH_y samples are. The photochromic response is strongest for the 0.40 Pa sample, just above the critical deposition pressure, and weakens substantially as the deposition pressure is increased.
(a) Spectral transmittance change of the 0.45 Pa sample after four hours of illumination by the UV irradiance spectrum $I(\lambda)$ as indicated in the figure. Transmittance of VIS–NIR regions above 700 nm wavelengths is significantly reduced in a uniform manner resulting in a darker appearance of the film. UV transparency has slightly increased, marking yttria formation (section 4.1.3).
(b) Effect of illumination on the averaged 450–1000 nm transmittances $\bar{T}(t)$ of the four samples, including that of (a). The three transparent YO_xH_y samples darken upon UV illumination and are therefore photochromic whereas the dark low-pressure YH_y sample does not appear to be affected.
(c) Normalised average transmittance with respect to their initial values $\bar{T}(t)/\bar{T}_0$, to eliminate the effect of varying initial transmittances $\bar{T}^\circ$ and allow for better comparison of the extent of darkening between the films.
(d) The normalised amounts of photodarkening $\Delta\bar{T}/\bar{T}_0$ of the samples after four hours of illumination. No contrast is recorded for the YH_y sample, whereas the three YO_xH_y samples darken upon UV exposure with a strong contrast reduction with increasing pressure.

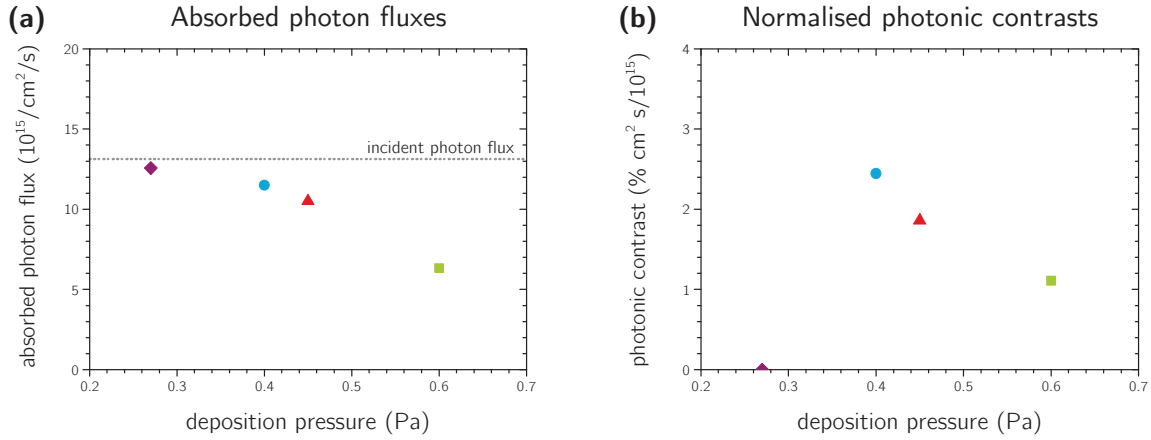

Figure 4.6. Correction of the photochromic contrasts of Figure 4.5 for the absorbed UV photon fluxes. The resulting photonic contrasts (contrast per absorbed UV photon per unit time per unit area) are used to quantify the photochromic performance.
(a) Absorbed photon fluxes $\Phi_{\mathrm{p}}^{\mathrm{abs}}$ of the darkened states of the films, indicating a reduced absorption of UV for higher pressures due to higher film porosities. Reflectance is not included in the calculation meaning that $\Phi_{\mathrm{p}}^{\mathrm{abs}}$ is somewhat overestimated, especially for the opaque 0.27 Pa sample with a larger reflectance than the transparent films. As this film is not photochromic, it is irrelevant for the photonic contrast.
(b) Photonic contrasts $\Delta\bar{T}/\Phi_{\mathrm{p}}^{\mathrm{abs}}\bar{T}_0$ as a function of deposition pressure. The contrast per absorbed UV photon is substantially reduced for increasing pressures and film porosities.

The opaque sample exhibits no observable darkening in response to UV illumination, confirming that this sample is indeed (mainly) non-photochromic YH_y. The VIS–NIR transmittances of the three transparent $\mathrm{YO}_x\mathrm{H}_y$ samples all decrease upon illumination and these samples are thus photochromic, with the strongest effect for the 0.40 Pa sample just above the critical pressure. Further increase of the deposition pressure has a severe negative effect on the observed contrast.

One could argue that the contrast reduction with pressure is linked to higher UV transparencies corresponding to the higher-pressure samples (Figure 4.2a), hence fewer photons being prone to photoexcitation of valence electrons across the band gap and therefore less photons contributing to the photochromic effect. To compensate for this reduced UV absorption, the *absorbed photon fluxes* $\Phi_{\mathrm{p}}^{\mathrm{abs}} = \int \Phi_{\mathrm{p}}(\lambda)A(\lambda)d\lambda = \int I(\lambda)A(\lambda)\lambda\, d\lambda/hc$ of each of the darkened films are determined from the spectral absorptances $A(\lambda)$ and the incident spectral irradiance $I(\lambda)$ (Figure 3.15a), and shown in Figure 4.6a. When the normalised contrasts of Figure 4.5d are compensated for absorbed photons this results in the *photonic contrasts* $\Delta\bar{T}/\Phi_{\mathrm{p}}^{\mathrm{abs}}\bar{T}_0$ of Figure 4.6b—i.e. the normalised contrasts per number of absorbed photons per unit area per unit time. This seems a good measure to quantify the photochromic performance. There is still a strong trend of reduced photodarkening for higher deposition pressures, albeit it somewhat weaker when considering the effect of reduced UV absorption.

There is a substantial contrast reduction of the UV-illuminated films with increasing deposition pressure and porosity. It appears that photochromic darkening is negatively affected by increasing film porosity, possibly due to smaller grain sizes. For optimisation of the photochromic darkening potential of reactively sputtered YH_y films, sputter deposition pressures should therefore be minimised whilst exceeding the minimum critical pressure to allow for the full YH_y–YO_xH_y transition to proceed.

4.1.3 Film stability

Beside inducing the YH_y–YO_xH_y transition, air exposure leads to oxidation of YO_xH_y to form an yttria (Y_2O_3) layer covering the samples. Yttria is non-photochromic and formation of yttria at the expense of YO_xH_y therefore reduces the darkening potential of the films. Although yttria formation is unavoidable—dense, α-Y and β-YH_y also oxidise [31]—further oxidation is to be limited.

Following the two-layer film model described in section 3.3.4, the transparent samples are represented as a UV-absorbing YO_xH_y layer covered by a UV-transparent oxide. The extent of oxide layer growths at the expense of absorbing YO_xH_y over some time interval is estimated from the UV transmittances $T(\lambda)$ and their initial values $T^\circ(\lambda)$ at 350 nm wavelengths (equation 3.3):

$$\frac{\Delta d_{\mathrm{ox}}}{d^\circ} = 1 - \left.\frac{\ln T(\lambda)}{\ln T^\circ(\lambda)}\right|_{\lambda=350\ \mathrm{nm}}$$

where $\Delta d_{\mathrm{ox}}/d^\circ$ is the oxide layer growth as a fraction of the initial YO_xH_y layer thickness d°. Note that since it is not possible to obtain the value of $T^\circ(\lambda)$ in the absence of any oxide due to immediate oxidation of the samples, nor to determine the absolute value of d° using these methods, oxide thicknesses are computed as a fraction of d° at the time of measuring $T^\circ(\lambda)$ (within half an hour of air exposure).

The effects of ageing under ambient conditions on the optical properties of the films are most apparent for the two highest-pressure samples, as seen from the spectral transmittance development over time (Figure 4.7a). Both show slight increases in VIS–NIR transmittances, but also significant gains in UV transmittances, marking yttria formation rather than a continuation of the YH_y–YO_xH_y transition. This is supported by a lack of notable changes in film band gaps (Figure 4.3). The shift of thin-film interference fringe peak positions to lower wavelengths is further evidence for these observations, indicating a reduction of optical path lengths in the samples and hence lower absorbing film thicknesses [45].

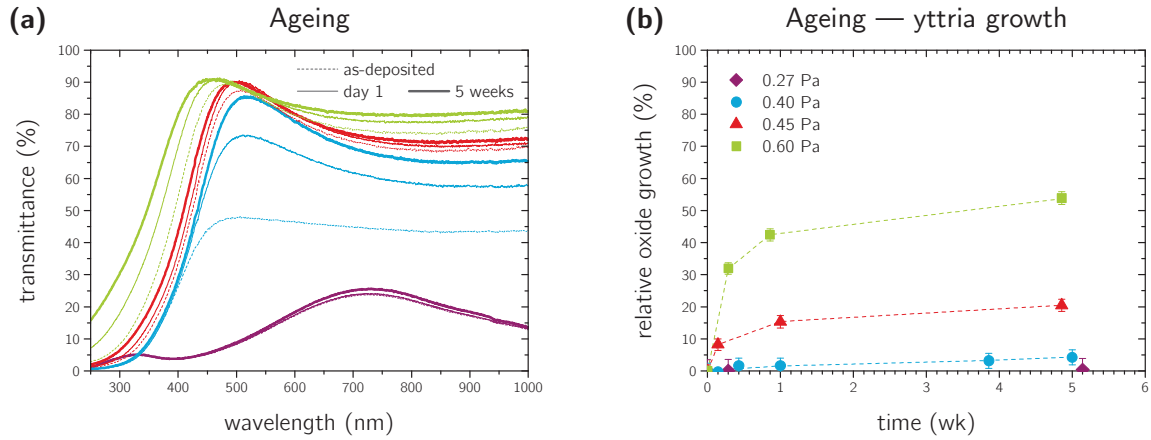

Figure 4.7. The effects of five weeks of ageing for varying deposition pressures. The two highest-pressure samples exhibit sustained growth of their oxide layers at the expense of YO_xH_y, the effect of which is strongest for the highest-pressure sample†. The 0.40 Pa sample shows a sustained YH_y–YO_xH_y transition and modest oxide layer growth. The opaque sample exhibits limited transformation of YH_y phases to YO_xH_y and no apparent yttria formation.

(a) Transmittance spectra after one month of air exposure. All samples show increased VIS–NIR transmittances, particularly for the 0.40 Pa sample, as well as UV transparency gains for the three transparent samples, increasing with pressure.

(b) Oxide layer growths relative to their initial YO_xH_y thicknesses, computed using equation 3.3 and absorption coefficients at 350 nm. One month of air exposure yields further Y_2O_3 formation at the expense of YO_xH_y, with enhanced oxidation for higher pressures. The oxide layer thickness of the dark sample seems unaffected.

The associated relative oxide layer growths $\Delta d_{\mathrm{ox}}/d^\circ$ as a function of sample age are given in Figure 4.7b. Yttria growth is strongest for the highest-pressure 0.60 Pa sample, with an YO_xH_y thickness reduction of over 40% within one week of air exposure. At deposition pressures of 0.45 Pa this effect is already substantially reduced to some 15%, and for the 0.40 Pa sample the effects of ageing are limited with no more than 5% oxide growth after five weeks. Yttria growth on the 0.27 Pa sample is negligible.

The enhanced yttria formation for increasing deposition pressures is due to higher film porosities and possibly expanded crystal lattices—both enhance oxidation susceptibility through increased oxygen penetration in the film.

The extent of oxide layer growth at the expense of photochromic YO_xH_y due to ageing is strongly correlated to film deposition pressures. Oxidation susceptibility increases substantially as the deposition pressure is increased above the critical pressure of roughly 0.40 Pa for the YH_y–YO_xH_y transition, due to higher film porosity. At or just above the

† Especially considering that its initial oxide layer thickness d° is probably already substantial due to oxidation within half an hour of air exposure.

critical pressure the extent of yttria formation is limited. For durability purposes in smart window applications, film deposition pressures should therefore be minimised to increase film density and hence oxidation resistance.

4.2 Band gap tuning

An issue concerning the potential application of photochromic YO_xH_y in commercial smart windows is its yellowish appearance. Favourable are colourless coatings, or ultimately the prospect of any colour of choice. YO_xH_y owes its yellowish colour to its 2.6 eV band gap and the consequential absorption of higher-energy blue and violet photons. Engineering of the band gap would therefore allow for altering the visual appearance of YO_xH_y-based photochromic films. To achieve colourless transparency, light of all visible wavelengths must be transmitted—i.e. photons of wavelengths above 400 nm or energies up to 3.1 eV. A band gap of at least 3.1 eV is thus to be pursued, yet exploration of the possibilities of tuning the band gap at all seems an appropriate first attempt for proof of concept.

4.2.1 Pressure-induced band gap widening

It has been (mistakenly‡) claimed that band gaps of sputter-deposited YO_xH_y can be widened up to 3.8 eV by increasing pressure–distance products [58]. The slightly growing

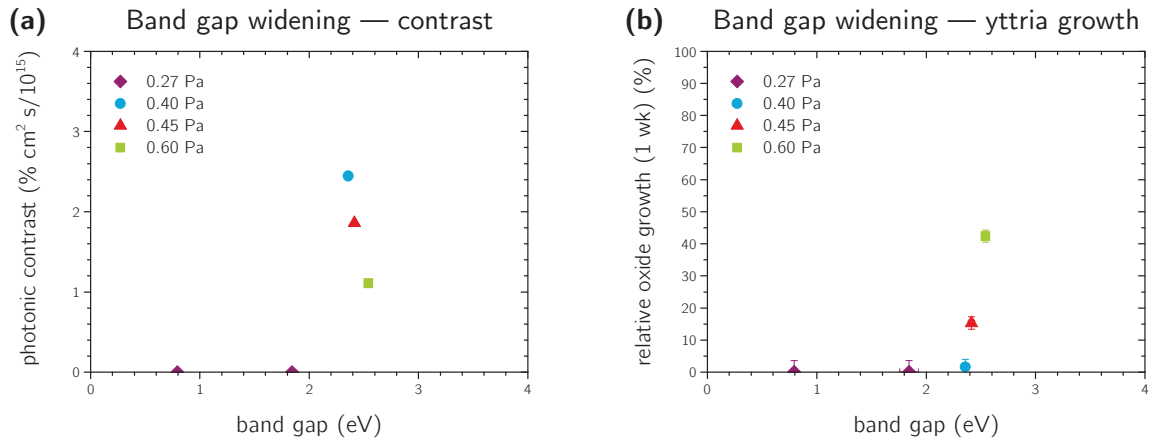

Figure 4.8. The detrimental effects of pressure-induced band gap widening on photochromic performance and film stability.
(a) The photonic contrasts decrease substantially with marginally widened band gaps for higher deposition pressures.
(b) Oxide layer growths at the expense of photochromic YO_xH_y due to one week of ageing are significantly enhanced for pressure-induced band gap increases.

‡ Due to the Menzel glass substrate, see Appendix B.

band-gap–pressure trend of Figure 4.3b indicates that YO_xH_y band gaps are indeed somewhat widened from 2.36(3) eV to 2.54(3) eV by increasing deposition pressures from 0.40 Pa to 0.60 Pa. Similar observations have been reported for DyO_xH_y, where band gaps of 2.26(3) eV $\leq E_g \leq$ 2.38(2) eV were obtained for deposition pressures between the near-critical pressure of 0.7 Pa and higher pressures up to 1.1 Pa [17]. As observed before and especially clear from Figure 4.8, however, the pressure-induced band-gap widening is accompanied by (a) a stark reduction in photochromic contrast, as well as (b) a greatly enhanced loss of photochromic material due to a single week of ageing. As the considered band gaps do not even approach 3.1 eV values and yet desirable film properties as contrast and durability are severely depressed, widening of the band gap through increasing deposition pressures and thereby film porosities is considered unsuitable for smart window applications.

4.2.2 Dysprosium–yttrium co-sputtering

Historically countless materials and materials properties have been optimised or created through e.g. alloying of metals or doping of semiconductors. The prospect of including elements other than Y in the sputtering of YO_xH_y films offers a wide range of possibilities in altering film properties, including the band gap, while maintaining film densities for photodarkening potential. Two main criteria for potential co-sputtering candidates are the availability of sputtering targets, and chemical resemblance to Y for crystal integrity purposes.

Dysprosium (Dy) is a trivalent lanthanide element with atomic number 66 (Figure 2.1) and is, like all rare earth elements, chemically similar to Y. Earlier studies have shown that DyH_y films sputtered at deposition pressures of 0.7 Pa oxidise in air to form transparent, photochromic, semiconducting DyO_xH_y with band gaps in the range 2.26–2.38 eV [17, 33]. Its fcc crystal structure with a lattice parameter of 5.40(2) Å is similar to the YO_xH_y crystal structure with lattice constants of 5.36–5.41 Å (Table 4.1). It therefore seems a promising candidate for co-sputtering with Y, ultimately forming a DyO_xH_y–YO_xH_y compound with a lower band gap than YO_xH_y.

Figure 4.9. Air-exposed DyO_xH_y–YO_xH_y gradient film, co-sputtered at a pressure of 0.72 Pa. The composition changes gradually from mostly DyO_xH_y (left) to mainly YO_xH_y (right). The greenish–yellowish colour of the predominantly DyO_xH_y end is due to its 2.36 eV band gap. The apparent transparency of the Y-rich end is due to high film porosity associated with the 0.72 Pa deposition pressure, far above the critical pressure of ~0.4 Pa for the YH_y–YO_xH_y transition.

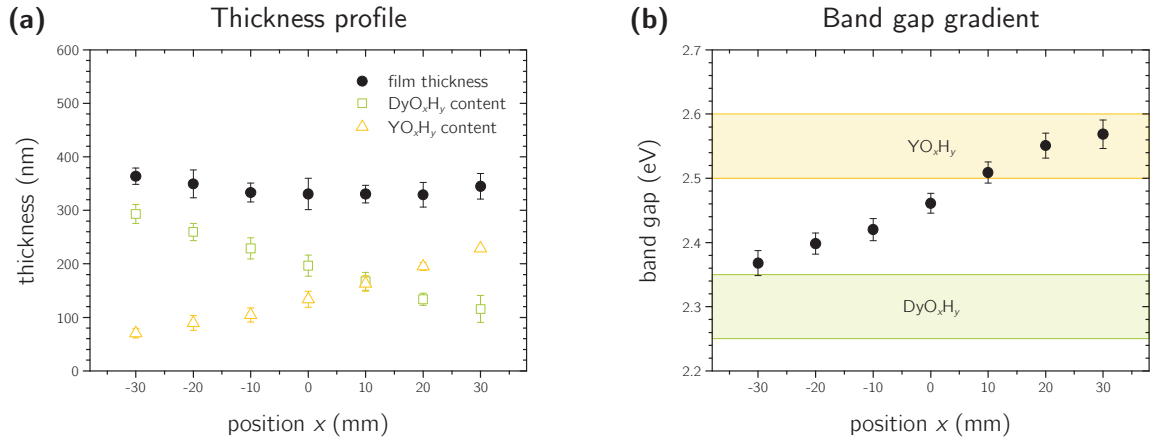

Figure 4.10. Thickness profile and band gap gradient of the co-sputtered DyO_xH_y–YO_xH_y gradient film. The band gap seems directly correlated to the relative DyO_xH_y–YO_xH_y composition.
(a) Film thickness profile and thickness profiles corresponding to separate, non-co-sputtered DyO_xH_y and YO_xH_y films using the same configuration. The relative thickness ratios are a good indicator of the DyO_xH_y–YO_xH_y composition profile, marking a roughly linear composition gradient from predominantly DyO_xH_y at $x = -30$ mm to mostly YO_xH_y at $x = +30$ mm.
(b) The film band gap gradient shows a roughly linear band gap increase from 2.36(2) eV at the Dy-rich end to 2.58(2) eV at the Y-rich end of the film.

To investigate the effect of relative DyO_xH_y–YO_xH_y concentrations on film band gap, a DyO_xH_y–YO_xH_y gradient film was reactively co-sputtered under a pressure of 0.72 Pa onto a 1 mm-thick 76 mm × 26 mm Menzel glass substrate. Because the Dy and Y targets are pointed towards opposite ends of the substrate the composition gradually changes from mainly DyO_xH_y on one film end to mostly YO_xH_y at the other end, hypothetically leading to a band gap gradient. The resulting sample is a greenish–yellowish transparent film as depicted in Figure 4.9.

To eliminate thickness effects in band gap determination using the Tauc plot method for Menzel glass substrates (see Appendix B) the film is of substantially high and reasonably uniform thickness (Figure 4.10a). The obtained film band gaps are shown in Figure 4.10b. One can clearly observe a band gap gradient in the range 2.36(2)–2.58(2) eV, varying between earlier reported band gap values of DyO_xH_y and YO_xH_y [13, 17]. The linearity of the curve indicates that film band gaps are directly correlated to the relative DyO_xH_y–YO_xH_y concentrations of the film.

4.3 Darkening model — yttrium dihydride domain growth?

In the introduction, several observations have been outlined regarding darkening of photochromic YO_xH_y. Solid-state NMR studies indicate the presence of highly mobile hydrogen species in the vicinity of oxygen in transparent YO_xH_y which disappear upon illumination, and it has been speculated that this is related to the formation of YH_y clusters in the transparent matrix [14]. XRD studies show a reversible lattice contraction upon photodarkening, which might also be related to the formation of YH_y phases [15]. Raman spectroscopy studies and effective medium approximations show that the formation of YH_y clusters is consistent with the observed optical properties [16]. These observations all seem to indicate a darkening mechanism involving the formation of metallic YH_y phases in a transparent YO_xH_y matrix.

To further elaborate on this hypothesis, an opaque domain growth darkening model is introduced. Observations on the influence of film porosity on photochromic contrast, the memory effect, and darkening and bleaching kinetics are linked to this model, providing additional (speculative) evidence for YH_y-domain-growth-induced photochromism.

Photochromic YO_xH_y is modelled as darkened, opaque phases D (YH_y) dispersed in a bleached, transparent matrix B (YO_xH_y), as depicted in Figure 4.11. The larger the concentration of darkened phases $x_D = 1 - x_B$, the higher the absorption and the darker the material appears. The absorption of a completely bleached material (i.e. $x_D = 0$) is equal to the bleached absorption cross section σ_B and the cross section of the darkened phase is σ_D. The resulting net absorption of the material is a superposition of phases B and D and is given by

$$\alpha = (1 - x_D)\sigma_B + x_D\sigma_D = \sigma_B + (\sigma_D - \sigma_B)x_D, \tag{4.1}$$

where $\sigma_B = \alpha_0$, i.e. the absorption of virgin, transparent YO_xH_y.

UV-induced photodarkening is considered to consist of two processes; i.e. (i) photoexcitation of valence electrons across the band gap, and (ii) nucleation and subsequent *grain coarsening* of opaque D phases in a transparent matrix B. The first process could

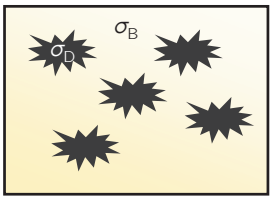

Figure 4.11. Representation of dark YH_y phases D dispersed in a bleached, transparent YO_xH_y matrix B. The corresponding absorption cross sections are σ_D and σ_B, respectively.

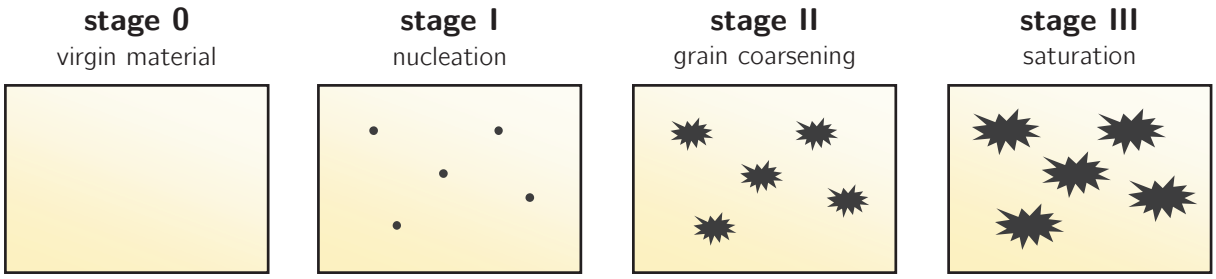

Figure 4.12. The stages of YH_y-domain-growth-induced darkening of transparent YO_xH_y. Stage 0 represents the transparent phase B prior to illumination. Illumination of the film yields stage I nucleation of D phases at high-energy sites such as grain boundaries or voids, followed by stage II grain coarsening of D phases at the expense of B. At some point D phases can no longer expand, referred to as stage III saturation.

well obey the multivalent defect model (section 2.3.3) and is not considered in this section. The second process is characterised by domain growth dynamics.

Similar to grain coarsening in metals and alloys [59], the B–D phase transformation is modelled as initial stage I nucleation with the appearance of D nuclei at energetically favoured sites such as grain boundaries (Figure 4.12). Proceeding UV illumination yields stage II grain coarsening of nucleated D phases at the expense of B, with D the energetically favourable phase under illumination. Stage II grain coarsening is curvature-driven growth, i.e. as to minimise the interfacial free energy between neighbouring domains. Depending on the system it may be constrained by transformation requirements such as diffusion of species within binary alloys [60]. It is typically *slow* growth, which does not tend to saturate at intermediate time scales. As D continues to grow, though, growth constraints such as the presence of dislocations, depletion of species, or growth of competing domains may impose stage III saturation.

As illumination ceases, thermal bleaching yields the transformation of D phases to form B (Figure 4.13).

To test the YH_y domain growth darkening model, several observations regarding photochromic behaviour of YO_xH_y are discussed. The effect of film porosity on photochromic contrast is addressed to link the contrast to domain growth potential. The

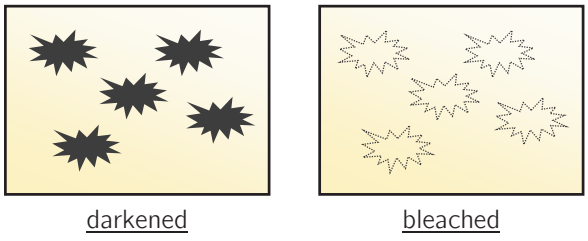

Figure 4.13. Bleaching of darkened films is represented as the disappearance of darkened phases D to form B.

memory effect (i.e. progressively faster darkening upon repetitive illumination) might be explained considering residual stresses arising from the lattice expansion associated with bleaching. Stress development due to UV-induced lattice contractions could be related to progressively slower bleaching for larger contrasts and repetitive cycling. Irreversible darkening of the YH_y–YO_xH_y interface may be coupled to partly irreversible YH_y domain growth. Darkening kinetics are analysed and linked to dynamically constrained grain coarsening.

4.3.1 Film porosity

As reported in section 3.1.3, increasing deposition pressures and associated film porosities have a profound negative effect on photochromic contrast (Figure 4.5d). This could be ascribed to limits to domain growth. Stage II grain coarsening is inhibited by dislocations such as grain boundaries and precipitates, as well as voids and surfaces. As film porosity involves the presence of voids and a lamellar type microstructure, this limits the grain size and therefore domain growth. The observed behaviour regarding reduced contrast with increasing porosity is thus in accordance with the YH_y domain growth model.

4.3.2 Memory effect

It has been reported that repetitive darkening and bleaching results in increasingly faster darkening, i.e. the *memory effect* [17, 18]. To illustrate this, a 91–428 nm-thick YO_xH_y gradient film (Figure 4.14) sputter-deposited at a pressure of 0.52 Pa is subjected to two illumination cycles using the MW–MW UV irradiance spectrum of Figure 3.17.

The resulting photodarkening curves $\bar{T}(t)$ of the purple and yellow sample positions of 335(15) nm and 428(51) nm thicknesses are shown in Figure 4.15a, and the corresponding normalised transmittances $\bar{T}(t)/\bar{T}_0$ are displayed in Figure 4.15b. The first cycle shows a modest initial drop in transmittances, followed by a long, elongated tail. The initial strong transmittance drops observed for the second cycle are substantially extended, i.e. down to the final transmittances after the first round of illumination. The purple curve seems to be saturated whereas the thicker, denser part of the film (yellow curve) continues to exhibit slow further darkening.

Figure 4.14. 91–428 nm-thick YO_xH_y gradient film (see section 3.1.4) sputter-deposited onto f-SiO_2 at a pressure of 0.52 Pa. The black circle corresponds to the thin, porous end of the film and the yellow circle marks the thick, dense end.

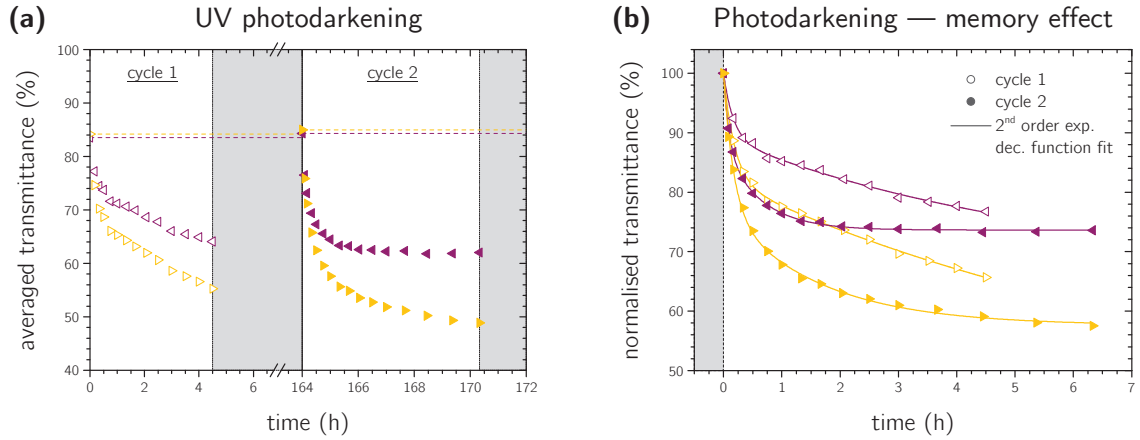

Figure 4.15. (a) Averaged VIS–NIR transmittance $\bar{T}(t)$ and **(b)** normalised transmittances $\bar{T}(t)/\bar{T}_0$ during repetitive photodarkening (and intermediate bleaching) of the purple and yellow sample positions of Figure 4.14. The first darkening curve shows an initial quick, modest transmittance drop, followed by an elongated, slowly darkening tail. A second curve shows fast darkening down to the final transmittance of the first cycle, after which it either saturates (purple) or continues slow further darkening (yellow). The higher contrast of the yellow curve is due to the higher film density and larger film thickness compared to the purple sample position.

The observations could be explained using the YH_y domain growth model. Photodarkening is accompanied by a reversible lattice contraction [15]. This is ascribed to a smaller lattice of the darkened YH_y phases, which is in turn expanded upon bleaching. To compensate for this lattice expansion, residual compressive stresses are developed at the previously darkened phases (Figure 4.16). Consequently, UV illumination now yields preferential stage I nucleation at these pre-stressed high-energy sites. Furthermore, resistance to stage II grain coarsening is considerably lowered as the growing, contracted D domains are readily accommodated for by the compressed surrounding matrix—the crystal has a *memory*. As a result, the prior constraints of stage II coarsening have been diminished, enhancing photodarkening rates.

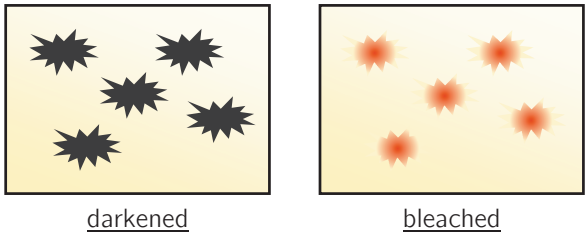

Figure 4.16. Residual compressive stresses arising from bleaching of darkened phases. Upon bleaching, the compressed darkened phases D expand, which is resisted by the surrounding matrix. As a result the newly formed bleached phases B are subjected to compressive stresses, which may remain in the crystal.

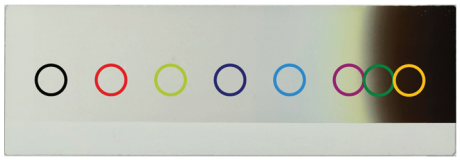

Figure 4.17. 27–119 nm-thick YH_y–YO_xH_y gradient film sputter-deposited onto f-SiO_2 at a pressure of 0.31 Pa. The transparent parts of the film have fully transformed to YO_xH_y upon air exposure, whereas the dark end marked by the yellow circle remains (mostly) YH_y. The sample positions indicated by the purple and green circles consist of a superposition of both untransformed YH_y and transformed YO_xH_y phases.

4.3.3 Pre-existing yttrium dihydride domain growth

A better insight into UV-induced growth of YH_y phases is gained by studying the growth of pre-existing YH_y phases in a YO_xH_y matrix. To track the photochromic behaviour of a superposition of YH_y and YO_xH_y phases, a 27–119 nm-thick gradient film was sputter-deposited at a pressure of 0.31 Pa. The resulting film contains both YH_y and YO_xH_y phases as shown in Figure 4.17 confirmed by the spectral transmittances of Figure 4.18b prior to

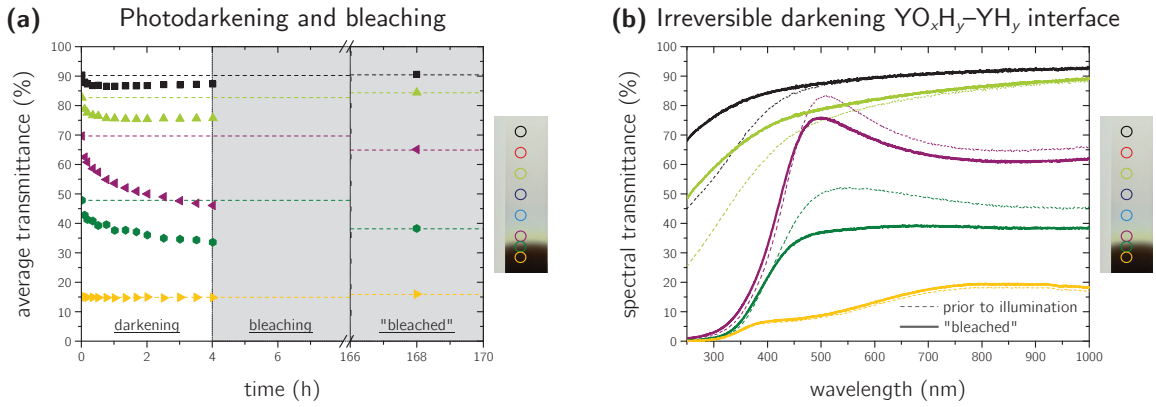

Figure 4.18. Partly irreversible photodarkening of the green and purple sample positions surrounding the YH_y–YO_xH_y phase boundary, possibly due to irreversible growth of pre-existing YH_y phases.
(a) Spectral transmittances of several sample positions, prior to four-hour UV illumination and after seven days of bleaching. The yellow line shows hardly any changes in transmittance, as it is mostly stable YH_y. The black and lime lines corresponding to the porous film ends mainly show a large increase in UV transmittance, indicating oxidation to form yttria. The purple and green curves are somewhere in between, marking a mixture of YH_y and YO_xH_y. They show a permanent lowering of VIS–NIR transmittances after illumination and subsequent bleaching.
(b) Averaged VIS–NIR transmittances of the film during photodarkening and subsequent bleaching for seven days. The black and lime sample positions exhibit limited photodarkening due to their high porosity. Bleaching allows them to return to their transparent states. The yellow curve does not darken at all as it is mainly YH_y. The purple and green curves show higher contrasts,§ but do not return to their initial averaged transmittances upon bleaching.

§ The light blue curve shows the highest (reversible) contrast as it consists of fully transformed YO_xH_y while lacking high porosity, but has been omitted from the figure for clarity.

illumination. The position indicated by the yellow line (dense microstructure) is mostly YH_y (see section 4.1.1), whereas the black and lime lines are (highly porous) YO_xH_y. The purple and green lines surrounding the YH_y–YO_xH_y boundary are somewhere in between, indicating a mixture of both YO_xH_y and untransformed YH_y phases.

Illumination of the sample using the spectral irradiance of Figure 3.17 yields darkening of all but the opaque YH_y sample position (Figure 4.18a). Subsequent bleaching for a week results in full bleaching of the fully transparent parts of the film (Figure 4.18b). The positions surrounding the YH_y–YO_xH_y phase boundary have, however, not fully bleached, and have remained so since. An irreversible YO_xH_y–YH_y transition appears to have occurred.

This too could point to UV-induced YH_y domain growth. As YH_y domains exceed some critical size their interiors may be 'shielded' from any tensile stresses by the surrounding YH_y phases, and relax to their unstressed, compact lattice. As the YH_y domain grows, a larger part of the domain is relieved from any stresses, expanding the size of the YH_y interior. Were YH_y phases to bleach by incorporation of oxygen to form YO_xH_y, a sufficiently large lattice is required. Contracted grain interiors might be unsusceptible to oxygen incorporation once irradiation is stopped and therefore inhibit the YH_y–YO_xH_y bleaching process.

4.3.4 Kinetics

Thermal bleaching

Considering an absorption coefficient $\alpha = \alpha_0 + (\sigma_D - \alpha_0)x_D$ (equation 4.1), rearrangement of the Lambert–Beer law (equation 2.2) yields a normalised transmittance for a film of thickness d

$$\frac{\bar{T}(x_D)}{\bar{T}_0} = \frac{e^{-\alpha(x_D)d}}{e^{-\alpha_0 d}} = e^{-(\sigma_D-\alpha_0)x_D d}.$$

The resulting concentration of darkened phases as a function of the normalised transmittance is then given by

$$x_D\left(\frac{\bar{T}}{\bar{T}_0}\right) = -\frac{1}{(\sigma_D - \alpha_0)d}\ln\left(\frac{\bar{T}}{\bar{T}_0}\right). \tag{4.2}$$

As illumination ceases, thermal bleaching yields the transformation of D phases to form B (Figure 4.13). Since it is a thermal process first-order kinetics are assumed, i.e. a transformation rate directly related to x_D such that $\partial x_D(t)/\partial t = -k_b t$, with $k_b = 1/\tau_b$ the bleaching reaction constant and τ_b the characteristic bleaching time. This results in a time-dependent concentration of darkened phases upon bleaching

$$\frac{x_{\mathrm{D}}(t)}{x_{\mathrm{D}}(0)} = e^{-t/\tau_{\mathrm{b}}},$$

with $x_{\mathrm{D}}(0)$ the fraction of D of the UV-darkened state. Plugging into equation 4.2 yields

$$e^{-t/\tau_{\mathrm{b}}} = -\frac{1}{x_{\mathrm{D}}(0)(\sigma_{\mathrm{D}} - \alpha_0)d} \ln\left(\frac{\bar{T}(t)}{\bar{T}_0}\right),$$

such that

$$\ln\left(-\ln\left(\frac{\bar{T}(t)}{\bar{T}_0}\right)\right) = -\frac{t}{\tau_{\mathrm{b}}} + \ln(x_{\mathrm{D}}(0)(\sigma_{\mathrm{D}} - \alpha_0)d)\,. \tag{4.3}$$

After the four-hour LW–LW UV exposures of the pressure series of Figure 4.5, their normalised VIS–NIR transmittances $\bar{T}(t)/\bar{T}_0$ are monitored during thermal bleaching of the samples. The PHOCS setup (section 3.3.1) allows for automated transmittance measurements at set time intervals, the results of which are shown in Figure 4.19a. One can clearly observe a strong decrease of bleaching rates with deposition pressures, i.e. film porosities.

The characteristic bleaching times τ_{b} are determined from equation 4.3 and the corresponding slopes of Figure 4.19b. The curves indeed indicate first-order kinetics as the majority portions of the curves are linear. The initial faster bleaching could be due to a temperature drop as the samples are removed from the lamps. The irregularities in the bleaching tails are possibly caused by light source fluctuations after hours of measurement. The resulting bleaching time constants as a function of deposition pressure (i.e. film porosity) are shown in Figure 4.19d, and exhibit a very strong increase in bleaching rates with increasing pressures, and therefore film porosity.

Beside longer bleaching times for lower film porosities, a second, identical illumination cycle for the 0.45 Pa sample also yields considerably slower bleaching than the first cycle (Figure 4.19c). As the associated contrasts are comparable, there appears to be a bleaching memory effect with a progressively reduced affinity to bleaching as the film is been subjected to repetitive illumination, an effect also observed for photochromic $\mathrm{DyO}_x\mathrm{H}_y$ and $\mathrm{ErO}_x\mathrm{H}_y$ [17, 39].

As both contrast and bleaching time constants decrease with film porosity, characteristic bleaching times increase with contrast (Figure 4.20). Apparently bleaching rates are diminished by increasing contrast, as well as repetitive illumination.

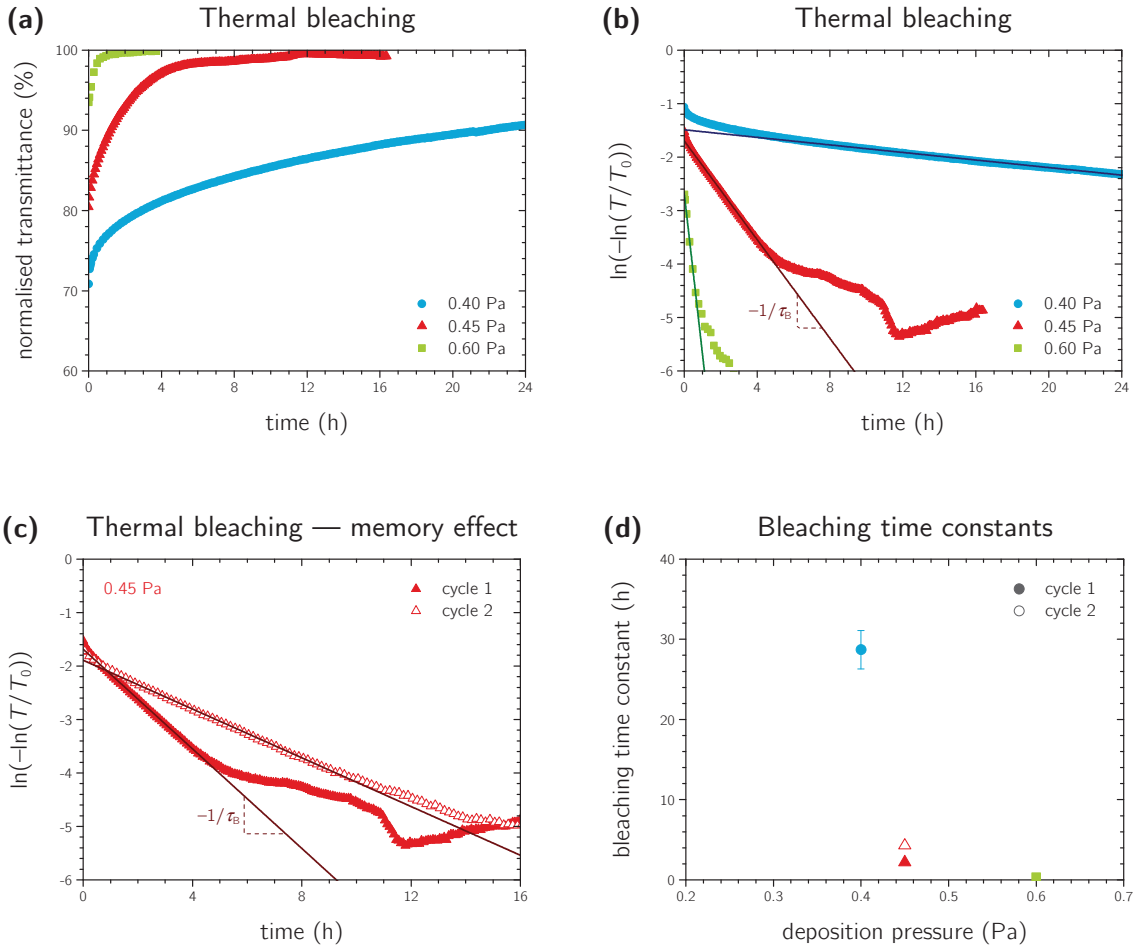

Figure 4.19. Bleaching kinetics of 100 nm-thick YO_xH_y films grown at varying pressures, revealing increased bleaching time constants for lower film porosity and repetitive illumination.
(a) Normalised average VIS–NIR transmittances $\bar{T}(t)/\bar{T}_0$ during bleaching after four-hour UV illumination of the samples grown at varying pressures.
(b) The normalised transmittances $\bar{T}(t)/\bar{T}_0$ shown in (a) are converted to $\ln(-\ln(\bar{T}(t)/\bar{T}_0))$ to obtain the characteristic bleaching time constants τ_b from equation 4.3. A clear increase of bleaching rates is observed with increasing pressures and, therefore, reducing contrasts.
(c) A second identical illumination cycle of the 0.45 Pa sample yields substantially slower bleaching than the first cycle. As the normalised transmittances of the darkened films at $t = 0$ are very similar, this is not a contrast effect but solely the effect of repetitive illumination.
(d) Characteristic bleaching time constants τ_b obtained from (b) and (c), showing a very strong reduction of bleaching time constants with deposition pressure (i.e. porosity), and a substantial bleaching time increase for repetitive illumination.

The responsible mechanism could be similar to the proposed suggestion regarding the irreversible YO_xH_y–YH_y transition (Figure 4.18). As the YH_y domains grow upon darkening, the domain interiors are increasingly relieved from tensile stresses as they are shielded from the larger YO_xH_y matrix. As such an expanding grain interior is allowed to relax to its preferred compact lattice, inhibiting oxygen incorporation upon bleaching. The larger the contrast, the smaller the lattice of the YH_y domain interior and the slower the

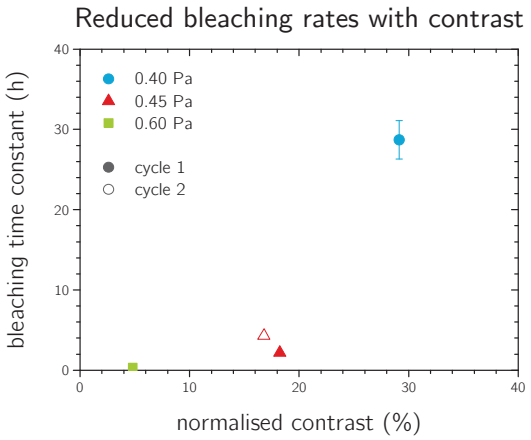

Figure 4.20. Bleaching time constants as a function of normalised contrast $\Delta\bar{T}(t)/\bar{T}_0$ for varying film deposition pressures, showing reduced bleaching rates for higher contrasts, as well as for repetitive illumination. The slightly reduced contrast for the second illumination cycle of the 0.45 Pa sample is ascribed to reduced YO_xH_y content due to UV-enhanced oxidation (see Appendix A).

bleaching. Repetitive illumination may also result in smaller lattices, as illumination cycling increasingly relieves the YH_y domains from tensile stresses imposed by the surrounding lattice.

Photodarkening

Stage II grain coarsening is quantified using time-dependent *characteristic length scales* $L(t)$ of expanding phases, which are typically of a power-law type growth

$$L(t) \propto t^n,$$

where e.g. $n = \frac{1}{2}$ for Lifshitz–Allen–Cahn (unconstrained curvature-driven) domain growth involved in diffusion-driven phase transformations, and $n = \frac{1}{3}$ for Lifshitz–Slyozov (spinodal decompositional) growth associated with phase transformations in quenched binary alloys [59, 60].

Other dynamically constrained coarsening models such as the three-dimensional Ising model for ferromagnetic domain growth [60, 61, 62] and the one- and two-dimensional diffusion-driven three-constituent ABC model [63, 64] have been reported to exhibit logarithmic growth, where growth constraints reduce with $L(t)$:

$$L(t) \propto \ln t\,.^{**}$$

Depending on the correlation between x_D and L, the normalised transmittance as a function of illumination time may be then of the forms

** As $\ln t$ is not an actual physical quantity it may be normalised by $\ln(t/t_0)$, with $t_0 \neq 0$.

$$\ln\left(\frac{\bar{T}(t)}{\bar{T}_0}\right) \propto -(\sigma_D - \alpha_0) d t^n,$$

where $n = \frac{1}{2}$ or $n = \frac{1}{3}$, or

$$\ln\left(\frac{\bar{T}(t)}{\bar{T}_0}\right) \propto -(\sigma_D - \alpha_0) d \ln t\,. \tag{4.4}$$

The logarithmic normalised transmittances of the pressure series of Figure 4.5 are plotted versus the logarithmic time in Figure 4.21, appearing to exhibit logarithmic growth. This may point to stage II domain growth of an Ising- or ABC-model type, i.e. growth with reducing growth constraints for expanding phases [60, 62, 63].

These same models also exhibit increasing characteristic relaxation times (i.e. bleaching time constants) with increasing characteristic length scales (i.e. contrast?) [60, 64], consistent with the observed reducing bleaching rates with increased contrast (Figure 4.19).

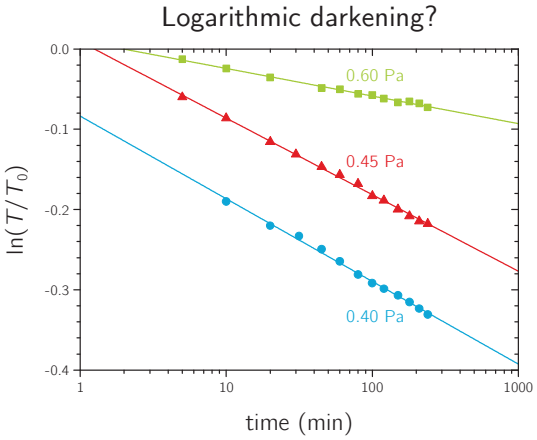

Figure 4.21. Logarithmic normalised transmittance $\ln(\bar{T}(t)/\bar{T}_0)$ during UV illumination of the transparent uniform samples of Figure 4.5, apparently following the time dependence of equation 4.4. The gentle slope of the 0.60 Pa sample compared to the 0.40 Pa and 0.45 Pa samples could be due to its lower thickness d. Note that the horizontal axis displays $\log t$ rather than $\ln t$ for clarity, not affecting the linearity of the curve as $\log t = \ln t / \ln 10$.

5 Discussion

The prime objective of this research is to optimise the deposition conditions for reactively sputtered photochromic YO_xH_y films for smart window applications, and relate these to film microstructure. By varying deposition pressures the resulting microstructures are linked to the YH_y–YO_xH_y transition, the photochromic contrast, and oxidation resistance for film stability.

Additionally, the yellowish appearance of YO_xH_y films is addressed and possibilities for tuning of the band gap are explored as a first step towards achieving colourless transparency.

An YH_y domain growth darkening model is introduced to explain and speculate on the observed photochromic behaviour regarding reducing contrast with film porosity, the memory effect, irreversible darkening of pre-existing YH_y phases, and darkening and bleaching kinetics.

Film growth optimisation

By increasing the deposition pressure of reactively sputtered, non-photochromic, dark YH_y films, the film porosity is increased. Under the specified conditions a critical deposition pressure of 0.40 Pa yields sufficient porosity to accommodate for spontaneous oxygen uptake by the lattice upon air exposure. The resulting YH_y–YO_xH_y transition leads to the formation of a photochromic film, supporting earlier observations [13, 17, 33]. For (near-)critical pressures the full transformation takes several days, whereas for higher pressures of 0.45 Pa and 0.60 Pa the process occurs instantaneously due to enhanced oxygen penetration by increased film porosity.

The YH_y–YO_xH_y transition is accompanied by a band gap widening up to 2.6 eV, indicating that increased oxygen content results in a larger band gap.

XRD data reveals an expanded crystal lattice for increasing deposition pressures. The crystal lattice of untransformed YH_y is slightly smaller than that of yttria, whereas the transformed YO_xH_y films have larger lattices. As it has been reported that oxygen uptake is accompanied by a lattice expansion of photochromic DyO_xH_y, and that DyH_y lattice parameters are independent of pressure [17], it appears that an expanded YO_xH_y crystal lattice is a sole result of enhanced oxygen uptake due to increased porosity. Once the po-

rosity is sufficiently large, oxygen can (slowly) penetrate shallow grain interiors and initiate the YH_y–YO_xH_y transition. For higher porosities the grains are smaller and oxygen-exposed surface areas are larger, hence the YH_y–YO_xH_y is transition is accelerated.

Besides increased affinity for the YH_y–YO_xH_y transition upon air exposure, high-pressure films are especially vulnerable to further oxidation comprising the growth of non-photochromic yttria at the expense of photochromic YO_xH_y. Ambient ageing of a 100 nm-thick film grown at a pressure of 0.60 Pa leads to a reduction of over 40% of photochromic material within a single week, whereas YO_xH_y losses of a film deposited at 0.40 Pa are no more than 5% over five weeks. This, too, is attributed to facile oxygen penetration and larger exposed surface areas in increasingly porous films. For film durability purposes, deposition pressures are therefore to be minimised to obtain a densest possible structure, retarding film deterioration through oxidation.

UV irradiance leads to a reduction of VIS–NIR transmittances of YO_xH_y, darkening the films, as reported before [7, 17, 33]. Four-hour UV illumination of intensities of the order of AM1.5 solar irradiance on 100 nm-thick films results in normalised photochromic contrasts of up to 28%. Films grown at near-critical deposition pressures exhibit a far superior contrast to higher-pressure films, even when corrected for greater photochromic YO_xH_y content due to better oxidation resistance. It appears that the photochromic effect is negatively affected by either increased film porosity, reduced grain sizes, an expanded crystal lattice, higher oxygen content, or a combination of these. Either way, a high-density film grown at low deposition pressures is to be pursued for maximum contrast.

Regarding both film stability and photochromic darkening potential of reactively sputtered YO_xH_y films for smart window applications, deposition pressures should be minimised to obtain a maximum contrast, whilst exceeding the critical pressure to allow for the full YH_y–YO_xH_y transition to proceed.

Further optimisation of film properties could be achieved by incorporating oxygen in the sputtering process. Meticulous control of the oxygen, hydrogen, and argon flows, as well as the Y target power supply, could result in both optimum film structure and composition without the need for post-deposition oxidation. As such an even denser, fully photochromic YO_xH_y film might be obtained, potentially improving both contrast and stability, as well as film homogeneity and reproducibility. One might also heat the chamber during sputter-deposition, resulting in higher adatom mobilities and enhanced surface and grain boundary diffusion to further increase film density and grain sizes.

Additionally, the films could be capped or covered by an oxidation-resistant, UV-transparent layer to prevent oxidation-induced film deterioration, although this would

not improve the photochromic contrast. Perhaps the application of a photochromic tungsten oxide (WO_3) layer covering the YO_xH_y film could be considered, as it has been observed that this specific combination of films leads to a substantial increase of both photochromic darkening rates and contrast compared to the separate YO_xH_y and WO_3 layers [65].

Band gap tuning

Due to its band gap of roughly 2.6 eV, photochromic YO_xH_y strongly absorbs higher-energy blue and violet photons and thus has a yellowish appearance [7]. For commercial applications in smart windows, however, colourless transparency would be preferential, and perhaps essential. This could be achieved by widening the band gap to at least 3.1 eV, extending photon transmittance to the entire visible spectrum.

By increasing the deposition pressure the band gap of photochromic YO_xH_y is slightly widened by increased oxygen content due to increased film porosity. Its effect is however limited to 0.1–0.2 eV band gap gains in the considered pressure ranges of 0.40–0.60 Pa. As increasing deposition pressures have a severe and negative effect on the photochromic contrast as well as further oxidation susceptibility, it is concluded that widening of the band gap by increasing deposition pressures is not feasible for smart window applications.

Band gap widening by increasing oxygen content while retaining a dense film might, however, be possible through e.g. reactive sputtering with oxygen.

Another option for band gap tuning is through alloying of YO_xH_y by co-sputtering with Dy. Due to the chemical similarities between Y and Dy the resulting film forms a stable DyO_xH_y–YO_xH_y compound upon air exposure. A DyO_xH_y–YO_xH_y gradient film with a roughly linear composition gradient between predominantly DyO_xH_y to mainly YO_xH_y has band gaps varying linearly in the range 2.36(2)–2.58(2) eV, in between earlier reported values of DyO_xH_y and YO_xH_y, respectively [13, 17, 33]. This indicates that the band gap of a DyO_xH_y–YO_xH_y compound is directly related to the relative DyO_xH_y–YO_xH_y concentrations, and that the band gap of YO_xH_y is tuneable by co-sputtering with materials of different band gaps.

Although co-sputtering with Dy narrows the band gap of YO_xH_y rather than widening it, it raises the potential of co-sputtering with larger-band-gap materials. With YO_xH_y having the largest band gap of the known photochromic REO_xH_ys [13, 17, 33], other materials could be considered for band gap widening. Candidates include magnesium or aluminium, of which the oxides have band gaps of 7.0–9.9 eV and 7.4–7.8 eV, respectively, significantly higher than that of yttria at 5.6 eV [32]. Potential alloying effects on photochromic behaviour of the resulting films must of course be kept in mind.

YH_y domain growth darkening model

Darkening of YO_xH_y is modelled as the formation and growth of opaque, contracted YH_y phases dispersed in a transparent YO_xH_y matrix. Several observations regarding the photochromic behaviour of YO_xH_y support this model.

The observed contrast reduction with deposition pressure could be explained by limits to YH_y domain sizes for increasingly porous films.

The memory effect, i.e. increasingly faster darkening for repetitive illumination, is ascribed to enhanced YH_y domain growth at previously darkened sites. Residual compressive stresses arising from lattice expansion of YH_y phases to form YO_xH_y during bleaching may induce preferential nucleation at these pre-stressed, high-energy sites upon illumination. Subsequent stage II grain coarsening constraints are diminished as the stressed lattice readily accommodates for lattice contractions associated with expanding YH_y domains.

Additionally, increasing characteristic bleaching times with increased contrast for higher-density films could be due to enhanced lattice contractions associated with larger YH_y domain sizes, impeding oxygen uptake by the lattice to form YO_xH_y upon bleaching. This could also explain the observed decreasing bleaching rate for repetitive illumination, progressively relieving YH_y domains from tensile stresses imposed by the surrounding matrix as the surrounding matrix increasingly accommodates for contracted YH_y phases.

The (partly) irreversible darkening of pre-existing YH_y could be ascribed to irreversible YH_y domain growth, as expanding YH_y phases result in increasingly large, contracted and stress-free domain interiors which are not susceptible to transform back to YO_xH_y upon bleaching.

As for the apparent logarithmic time-dependence regarding stage II grain coarsening, it seems worthwhile to study dynamically constrained domain growth models exhibiting logarithmic growth. Such models include the Ising model for ferromagnetic domain growth [60, 61, 62] and the one- and two-dimensional diffusion-driven ABC model [63, 64]. These models also exhibit increased relaxation times with domain size. They might provide better insights into the darkening and bleaching mechanisms involved in photochromic REO_xH_ys.

Although speculative, further investigation of the YH_y domain growth darkening model looks promising. It remains unclear whether the proposed YH_y–YO_xH_y bleaching phase transformation is similar to the as-deposited YH_y–YO_xH_y transition upon air exposure, i.e. due to the incorporation of external oxygen species by the YH_y lattice. This could be

verified by studying the photochromic behaviour of YO_xH_y in an oxygen-deprived environment. One could think of darkening and subsequent bleaching in a nitrogen-flushed glove box or in vacuum—is oxygen required for bleaching? This also raises the question whether darkening could be faster in the lack of oxygen, due to enhanced depletion of oxygen species in YO_xH_y to form YH_y and the absence of the bleaching reaction from YH_y to YO_xH_y.

XRD studies may support the proposed mechanism of irreversible growth of pre-existing YH_y phases by an irreversible lattice contraction.

For the development of photochromic smart windows, the YH_y domain growth model could introduce possibilities of limiting bleaching time scales by limitations to domain sizes, e.g. by annealing and subsequent quenching of the films to obtain smaller grains, or by the addition of pinning dislocations in the matrix impeding domain growth.

6 Conclusions

It has been shown that for reactively sputtered YH_y films to fully transform to photochromic YO_xH_y upon air exposure, a minimum critical deposition pressure is required to obtain a sufficiently porous microstructure which allows for spontaneous oxygen uptake by the crystal lattice. The lower the deposition pressure, the denser the resulting microstructure and the slower the YH_y–YO_xH_y transition. Lower pressures than the critical pressure result in the transformation of only a limited fraction of YH_y to form YO_xH_y. Higher pressures result in enhanced oxidation susceptibility to form non-photochromic yttria at the expense of photochromic YO_xH_y. Moreover, the photochromic contrast per absorbed UV photon is strongly reduced for increasing deposition pressures and associated film porosities. Reactively sputtered, post-deposition-oxidised YO_xH_y films for smart window applications should therefore be grown at or just above the critical deposition pressure for optimum stability and photochromic contrast.

In an attempt to widen YO_xH_y band gaps to over 3.1 eV to obtain colourless transparency, it is concluded that increasing deposition pressures widen the band gap due to increased oxygen content resulting from increased film porosity. Its effect is however limited to 0.1–0.2 eV and has a severely negative impact on film stability and photochromic contrast. Alternatively, the band gap can be lowered by co-sputtering with DyO_xH_y to obtain band gap values ranging between that of DyO_xH_y (2.3 eV) and YO_xH_y, depending on the relative DyO_xH_y–YO_xH_y concentrations. This advances the prospect of co-sputtering with larger-band-gap materials to widen the band gap to over 3.1 eV.

An YH_y domain growth darkening model involving grain coarsening of dark, contracted YH_y phases dispersed in a transparent YO_xH_y matrix has been introduced which may explain the observed photochromic behaviour of YO_xH_y. Reduced contrast with film porosity could be due to limits to YH_y domain sizes in increasingly porous films. Increasingly faster darkening for repetitive illumination might be related to residual compressive stresses at previously darkened sites, reducing YH_y growth constraints. Progressively slower bleaching rates for higher contrasts *and* repetitive illumination may be caused by enhanced lattice contractions impeding the YH_y–YO_xH_y bleaching transformation. Irreversible darkening of pre-existing YH_y phases could be due to irreversible domain growth. The observations seem to support the model.

Acknowledgements

The studies have been conducted as part of ongoing research on photochromism of rare earth oxyhydrides by the Materials for Energy Conversion and Storage (MECS) research group at the Department of Chemical Engineering (ChemE) at Delft University of Technology.

Within the photochromics group in particular I have had a wonderful and rewarding time. I would like to thank dr. Steffen Cornelius for his supervision on the research, close collaboration, advice, and fun and fruitful discussions, prof. dr. Bernard Dam for his critical thinking, clear approach, and general enthusiasm on the topic, ing. Herman Schreuders for his technical assistance and good laughs, and PhD candidate Fahimeh Nafezarefi for proof reading, her lovely company, the fresh air, and free coffee.

I would like to thank dr. Amarante Böttger for organising and chairing the assessment committee, and dr. Steffen Cornelius, prof. dr. Bernard Dam and dr. Tom Savenije for willing to be part of it.

I wish you all the best.

Bibliography

[1] L. Pérez-Lombard, J. Ortiz and C. Pout, "A review on buildings energy consumption information," *Energy Build.* **40**: pp. 394–98, 2008.

[2] D. Ürge-Vorsatz, L. F. Cabeza, S. Serrano, C. Barreneche and K. Petrichenko, "Heating and cooling energy trends and drivers in buildings," *Renew. Sustainable Energy Rev.* **41**: pp. 85–98, 2015.

[3] L. W. Davis and P. J. Gertler, "Contribution of air conditioning adoption to future energy use under global warming," *Proc. Natl. Acad. Sci. U.S.A.* **112** (19): pp. 5962–67, 2015.

[4] S. D. Rezaei, S. Shannigrahi and S. Ramakirshna, "A review of conventional, advanced, and smart glazing technologies and materials for improving indoor environment," *Sol. Energ. Mat. Sol. Cells* **159**: pp. 26–51, 2017.

[5] Y. Wang, E. L. Runnerstrom and D. J. Milliron, "Switchable materials for smart windows," *Annu. Rev. Chem. Biomol. Eng.* **7:** pp. 283–304, 2016.

[6] R. J. Araujo, "Photochromic glasses," in *Encyclopedia of Physical Science and Technology*, 3rd ed., R. A. Meyers (ed.), Academic Press, pp. 46–56, 2002

[7] T. Mongstad, C. Platzer-Björkman, J. P. Mæhlen, L. P. A. Mooij, Y. Pivak, B. Dam, E. S. Marstein, B. C. Hauback and S. Z. Karazhanov, "A new thin film photochromic material: oxygen-containing yttrium hydride," *Sol. Energ. Mat. Sol. Cells* **95**: pp. 3596–99, 2011.

[8] A. T. M. van Gogh, D. G. Nagengast, E. S. Kooij, N. J. Koeman, J. H. Rector, R. Griessen, C. F. J. Flipse and R. J. J. G. A. M. Smeets, "Structural, electrical, and optical properties of $La_{1-z}Y_zH_x$ switchable mirrors," *Phys. Rev. B.* **63** (19): p. 5105, 2001.

[9] A. F. T. Hoekstra, A. S. Roy, T. F. Rosenbaum, R. Griessen, R. J. Wijngaarden and N. J. Koeman, "Light-induced metal–insulator transition in a switchable mirror," *Phys. Rev. Lett.* **86** (23): pp. 5349–52, 2001.

[10] J. N. Huiberts, R. Griessen, J. H. Rector, R. J. Wijngaarden, J. P. Dekker, D. G. de Groot and N. J. Koeman, "Yttrium and lanthanum hydride films with switchable optical properties," *Nature* **380**: pp. 231–34, 1996.

[11] A. Ohmura, A. Machida, T. Watanuki and K. Aoki, "Photochromism in yttrium hydride," *Appl. Phys. Lett.* **91** (15): p. 1904, 2007.

[12] T. Mongstad, C. Platzer-Björkman, S. Z. Karazhanov, A. Holt, J. P. Mæhlen and B. C. Hauback, "Transparent yttrium hydride thin films prepared by reactive sputtering," *J. Alloys Compd. S* **509**: pp. 812–16, 2011.

[13] T. Mongstad, A. Thøgersen, A. Subrahmanyam and S. Karazhanov, "The electronic state of thin films of yttrium, yttrium hydrides and yttrium oxide," *Sol. Energ. Mat. Sol. Cells* **128**: pp. 270–74, 2014.

[14] C. V. Chandran, H. Schreuders, B. Dam, J. W. G. Janssen, J. Bart, A. P. M. Kentgens and P. J. M. van Bentum, "Solid-state NMR studies of the photochromic effects of thin films of oxygen-containing yttrium hydride," *J. Phys. Chem. C* **118**: pp. 22935–42, 2014.

[15] J. P. Mæhlen, T. T. Mongstad, C. C. You and S. Z. Karazhanov, "Lattice contraction in photochromic yttrium hydride," *J. Alloys Compd. S* **580**: pp. 119–21, 2013.

[16] J. Montero, F. A. Martinsen, M. García-Tecedor, S. Z. Karazhanov, D. Maestre, B. Hauback and E. S. Marstein, "Photochromic mechanism in oxygen-containing yttrium hydride thin films: An optical perspective," *Phys. Rev. B* **20**: p. 1301, 2017.

[17] E. F. E. ten Have, *Investigation of the photochromic properties of dysprosium oxyhydride*, Delft University of Technology, MSc thesis, 2016.

[18] M. J. Retera, *Investigation of the photochromic properties of gadolinium oxyhydride and erbium oxyhydride*, Delft University of Technology, BSc thesis, 2017.

[19] A. Miniotas, B. Hjövarsson and L. Douysset, "Gigantic resistivity and band gap changes in GdO_yH_x thin films," *Appl. Phys. Lett.* **76** (15): p. 2056, 2000.

[20] CRC, *CRC Handbook of Chemistry and Physics*, 95th ed., W. M. Haynes, D. R. Lide and T. J. Bruno (eds.), Boca Raton, CRC Press, 2014.

[21] IUPAC, "IUPAC periodic table of the elements," 2016. [Online] available: www.iupac.org/cms/wp-content/uploads/2015/07/IUPAC_Periodic_Table-28Nov16.pdf [accessed 1/6/2017].

[22] P. Vajda, "Hydrogen in rare-earth metals, including RH_{2+x} phases," in *Handbook on the Physics and Chemistry of Rare Earths*, K. A. Gschneider (ed.), Amsterdam, Elsevier, 1995.

[23] P. Vajda, J. N. Daou, A. Lucasson and J. P. Burger, "Defect study of yttrium–hydrogen solid solutions," *J. Phys. F.: Met. Phys.* **17**: pp. 1029–41, 1987.

[24] Y. Fukai, *The Metal–Hydrogen System*, 2nd ed., Berlin, Springer, 2004.

[25] V. K. Fedotov, A. E. Antonov, I. O. Bashkin, T. Hansen and I. Natkaniec, "Displacive ordering in the hydrogen sublattice of yttrium trihydride," *J. Phys.: Condens. Matter* **18**: pp. 1593–99, 2006.

[26] A. Remhof, *Hydrogen in yttrium films—structure and phase formation*, Ruhr-Universität Bochum, PhD dissertation, 1999.

[27] N. F. Miron, V. I. Scherbak, V. N. Bykov and V. A. Levdik, *Kristallografiya* **17**: p. 404, 1972.

[28] Y. N. Xu, Z. Q. Gu and W. Y. Ching, "Electronic, structural, and optical properties of crystalline yttria," *Phys. Rev. B* **56** (23): pp. 14993–15000, 1997.

[29] N. Sarmadian, R. Saniz, B. Partoens, D. Lamoen, K. Volety, G. Huyberechts and J. Paul, "High throughput first-principles calculations of bixbyite oxides for TCO applications," *Phys. Chem. Chem. Phys.* **16** (33): pp. 17724–33, 2014.

[30] G. Baldinozzi, J. F. Bérar and G. Calvarin, "Rietveld refinement of Zr-doped Y_2O_3," *Mater. Sci. Forum* **278–81**: pp. 680–85, 1989.

[31] T. Mongstad, C. Platzer-Björkman, J. P. Mæhlen, B. C. Hauback, S. Z. Karazhanov and F. Cousin, "Surface oxide on thin films of yttrium hydride studied by neutron reflectometry," *Appl. Phys. Lett.* **100** (19): p. 1604, 2012.

[32] W. H. Strehlow and E. L. Cook, "Compilation of energy band gaps in elemental and binary compound semiconductors and insulators," *J. Phys. Chem. Ref. Data* **2** (1): pp. 163–99, 1973.

[33] F. Nafezarefi, H. Schreuders, B. Dam and S. Cornelius, "Photochromism of rare-earth metal oxyhydrides," *App. Phys. Lett.* **111** (10): pp. 3903, 2017.

[34] J. R. Hook and H. E. Hall, *Solid State Physics*, 2nd ed., Chichester, John Wiley & Sons, 1991.

[35] M. Irie, "Photochromism: memories and switches—Introduction," *Chem. Rev.* **100** (5): pp. 1683–84, 2000.

[36] J. Fritzsche, *C. R. Acad. Sci.* **69**: p. 1035, 1867.

[37] A. S. Matharu and P. S. Ramanujam, "Photochromic polymers for optical data storage: azobenzenes and photodimers," in *Photochemistry and photophysics of polymeric materials*, N. S. Allen (ed.), Hoboken, John Wiley & Sons, 2010.

[38] S. Cornelius, private correspondence, 2016.

[39] M. Carrer, private correspondence, 2017.

[40] R. J. Araujo, "Photochromism in glasses containing silver halides," *Contemp. Phys.* **21** (1): pp. 77–84, 1980.

[41] K. A. Willets and R. P. van Duyne, "Localized surface plasmon resonance spectroscopy and sensing," *Annu. Rev. Phys. Chem.* **58**: pp. 267–97, 2007.

[42] T. P. Seward, "Coloration and optical anisotropy in silver-containing glasses," *J. Non-Cryst. Solids* **40**: pp. 499–513, 1980.

[43] C. L. Marquardt, J. F. Giuliani and R. T. Williams, "Darkening mechanisms in silver-halide photochromic glasses: flash photolysis and ESR studies," *J. Appl. Phys.* **40** (11): pp. 4915–25, 1976.

[44] D. J. Griffiths, *Introduction to Electrodynamics*, 3rd ed., A. Reeves and K. Dellas (eds.), San Francisco, Pearson Benjamin Cummings, 2008.

[45] O. Stenzel, *The Physics of Thin Film Optical Spectra—An Introduction*, 2nd ed., R. Carr, G. Ertl, H. Freund, H. Lüth and M. A. Rocca (eds.), Springer, 2016.

[46] R. Behrisch and W. Eckstein, "Sputtering by particle bombardment," in *Topics in applied physics*, vol. 110, C. E. Ascheron and W. Skolaut (eds), Heidelberg, Springer–Verlag, 2007.

[47] D. Depla and S. Mahieu, "Reactive sputter deposition," in *Springer Series in Materials Science*, vol. 109, R. Hull, R. M. Osgood, J. Parisi and H. Warlimont (eds.), Heidelberg, Springer–Verlag, 2008.

[48] J. A. Thornton, "The microstructure of sputter-deposited coatings," *J. Vac. Sci. Technol. A* **4** (6): pp. 3059–65, 1986.

[49] S. Cornelius, *Charge transport limits and electrical dopant activation in transparent conductive (Ag,Ga):ZnO and Nb:* TiO_2 *thin films prepared by reactive magnetron sputtering*, Technischen Universität Dresden, PhD dissertation, 2013.

[50] P. B. Barna and M. Adamik, "Fundamental structure forming phenomena of polycrystalline films and the structure–zone models," *Thin Solid Films* **317**: pp. 27–33, 1998.

[51] J. H. Keller and R. G. Simmons, "Sputtering process model of deposition rate," *IBM J. Res. Develop.* **23** (1): pp. 24–32, 1979.

[52] D. Brandon and W. D. Kaplan, *Microstructural Characterization of Materials*, 2nd ed., Chichester, John Wiley & Sons, 2008.

[53] B. L. Henke, E. M. Gullikson and J. C. Davis, "X-ray interactions: photoabsorption, scattering, transmission, and reflection at $E = 50$–$30{,}000$ eV, $Z = 1$–92," *Atom. Data Nucl. Data* **54**: pp. 181–342, 1993.

[54] A. J. Illig, C. T. Chantler and A. T. Payne, "Voigt profile characterization of copper Kα," *J. Phys. B: At. Mol. Opt. Phys.* **46**, 2013.

[55] J. Tauc, R. Grigorovici and A. Vancu, "Optical properties and electronic structure of amorphous germanium," *Phys. Stat. Sol.* **15**: pp. 627–37, 1966.

[56] R. V. Hogg and A. T. Craig, *Introduction to Mathematical Statistics*, New York: Macmillan, 1978.

[57] NIST, *Engineering Statistics Handbook*, 2012.

[58] C. C. You, T. Mongstad, J. P. Mæhlen and S. Z. Karazhanov, "Engineering of the band gap and optical properties of thin films of yttrium hydride," *App. Phys. Lett.* **105** (3): 2015.

[59] D. A. Porter, K. E. Easterling and M. Y. Sherif, *Phase Transformations in Metals and Alloys*, 3rd ed., Boca Raton, CRC Press, 2009.

[60] J. D. Shore, M. Holzer and J. P. Sethma, "Logarithmically slow domain growth in nonrandomly frustated systems: Ising models with competing interactions," *Phys. Rev. B* **46** (18): pp. 11376–404, 1992.

[61] F. C. Zhang, O. T. Valls and G. F. Mazenko, "Growth of order in order–disorder transitions: tests of universality," *Phys. Rev. B* **31** (3): p. 1579, 1985.

[62] R. Paul, S. Puri and H. Rieger, "Domain growth in Ising systems with quenched disorder," *Phys. Rev. E* **71** (6): p. 1109, 2005.

[63] M. R. Evans, "Anomalous coarsening and glassy dynamics," *J. Phys.: Condens. Matter,* vol. 14, pp. 1397–422, 2002.

[64] M. O. Brown, R. H. Galyean, X. Wang and M. Pleimling, "Relaxation processes in a system with logarithmic growth," *Phys. Rev. E* **91** (5): p. 2116, 2015.

[65] M. La, N. Li, R. Sha, S. Bao and P. Jin, "Excellent photochromic properties of an oxygen-containing yttrium hydride coated with tungsten oxide (YH_x: O/WO_3)," *Scripta Mater.* **142**: pp. 36–40, 2018.

[66] ASTM, "Standard tables for reference solar spectral irradiances: direct normal and hemispherical on 37° tilted surface," *ASTM G173–03*, 2012.

Appendix A UV-enhanced oxidation

A closer look at the spectral transmittance of the UV-darkened 0.45 Pa sample after four hours of illumination (Figure 4.5a) reveals an increased UV transmittance with respect to its initial state. Leaving the sample unexposed to light to return to its bleached state reveals that this increased UV transmittance is irreversible (Figure A-1a), with similar observations for the other photochromic samples. Furthermore, a slight interference fringe shift to lower wavelength values is observed, indicating a lower YO_xH_y thickness due to a reduction of the optical path length in the material. Analogous to ageing, these effects are ascribed to oxide growth at the expense of absorbing YO_xH_y (see section 3.3.4). The extent of this UV-induced yttria formation is quantified using the two-layer film model and equation 3.3, the results of which are displayed in Figure A-1b.

Each of the samples exposed to four-hour UV illumination show significant oxide layer growths with respect to their unilluminated (aged) siblings. The relative UV-induced YO_xH_y thickness losses for the varying deposition pressures are all in the order of 10% of the initial YO_xH_y thickness $d°$, making the effect especially obvious for the 0.40 Pa sample most resistant to ambient ageing. This UV-induced oxide growth is possibly due to enhanced oxidation by *photocatalytic water splitting*—the dissociation of adsorbed atmospheric moisture into hydrogen and oxygen upon absorption of photons of sufficient energy. Tracking the UV transparency gains during UV illumination of a YO_xH_y sample in an inert-gas-flushed environment (e.g. nitrogen) or vacuum could verify this hypothesis.

UV-induced oxidation could, like regular oxidation, be prevented by applying a UV-transparent, oxidation-resistant capping layer over the film, thereby keeping out moisture and oxidising gases.

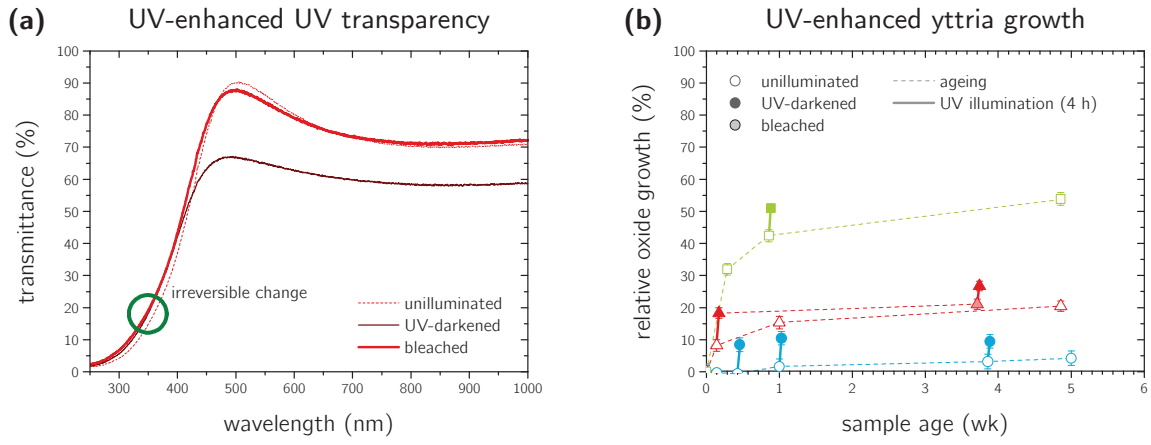

Figure A-1. (a) UV-enhanced UV transparency and **(b)** associated oxide layer growths using the two-layer film model (section 3.3.4).

Appendix B Menzel glass substrate — band gap widening?

It is important to note the necessity for care concerning band gap determination using the Tauc plot method regarding films on substrates other than UV grade f-SiO_2. Band gap values of up to 3.8 eV have been reported for non-uniform YO_xH_y films on Menzel glass substrates, effectively by increasing the pressure–distance product [58]. These values are, however, not to be ascribed to the YO_xH_y film but rather to the film–substrate combination. To illustrate this two identical 91(13)–428(51) nm-thick YH_y gradient films are sputtered under a pressure of 0.52 Pa onto different 76 mm × 26 mm substrates, one on f-SiO_2 and one on Menzel glass. The resulting air-exposed YO_xH_y film on f-SiO_2 is depicted in Figure B-1.

The spectral transmittances corresponding to the sample positions marked by the coloured circles for both samples are given in Figure B-2a–b. For VIS–NIR wavelengths the transmittances of the films are very similar, but not in the UV. The main difference between the two samples is strong absorption of wavelengths below some 350 nm for the film grown on Menzel glass. This effect is especially clear for the black, red and green lines, as UV transmittances on the f-SiO_2 substrate are significant for these sample positions due to low thickness and enhanced yttria formation resulting from high pressure–distance products.

The difference between the Tauc plots of the thinnest ends of the two samples ($x = -30$ mm) is displayed in Figure B-2c, as well as the Tauc plots corresponding to the bare substrates. UV absorptances of these ends of the films are low and substrate absorptances therefore become significant. As observed from the Tauc plot matching the f-SiO_2 sample the linear part of the curve is unambiguous and the corresponding band gap of approximately 2.6 eV is clear. For the film grown on Menzel glass, however, a large portion of the curve is dominated by substrate absorptance and one could readily mistake it for the film absorption edge, obtaining a band gap value of approximately 3.6 eV—almost the 3.8 eV band gap of the Menzel glass substrate itself.

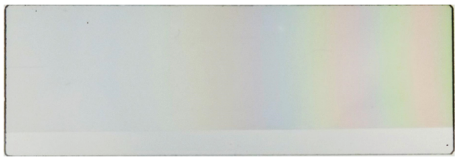

Figure B-1. 91–428 nm-thick YO_xH_y gradient film sputter-deposited at a pressure of 0.52 Pa.

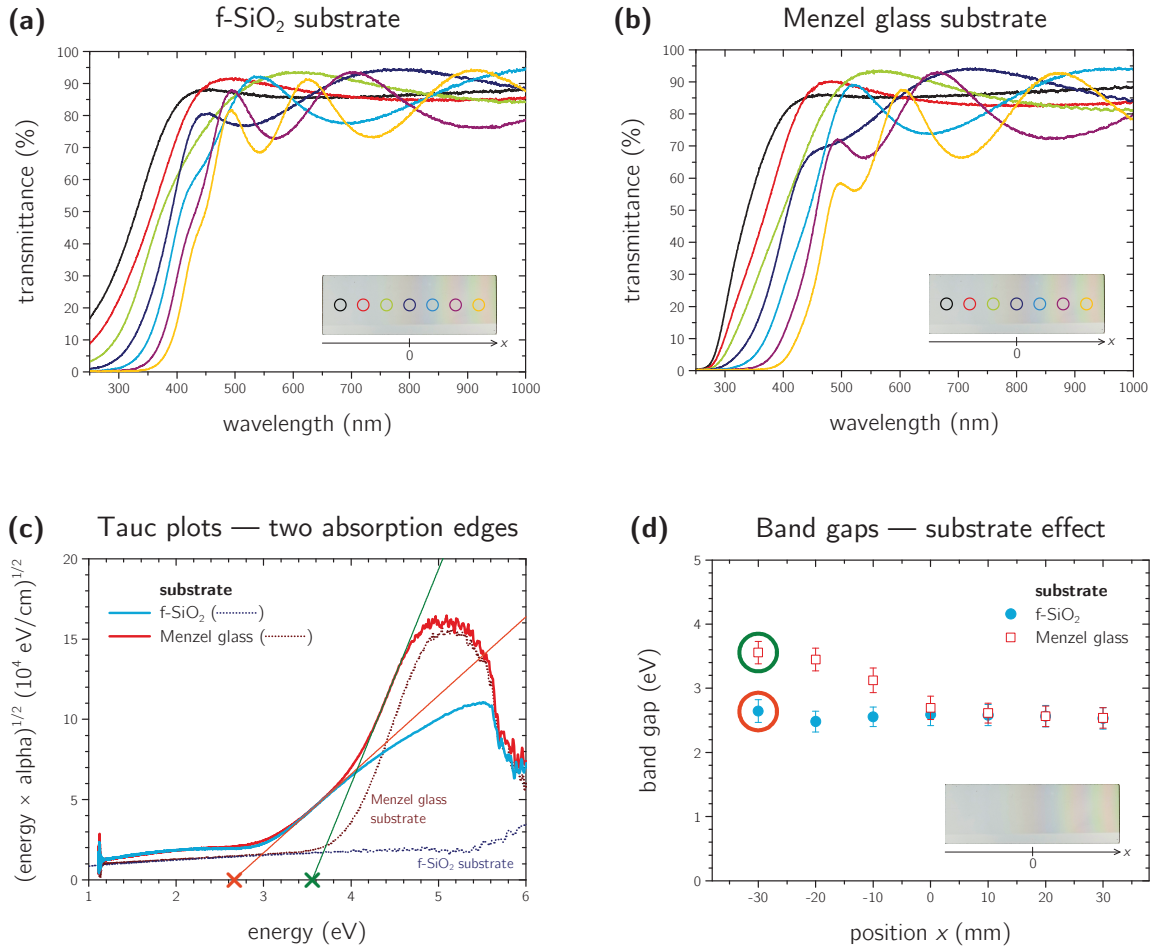

Figure B-2. Spectral transmittances of two identical films deposited onto **(a)** UV grade f-SiO_2 and **(b)** Menzel glass. **(c)** The UV absorption of the Menzel glass substrate greatly influences the Tauc plot of the thin, porous end of the film (indicated by the black circle). **(d)** Depending on the chosen extrapolation range in the Tauc plot the obtained band gaps for different substrates can vary heavily for thin, porous films.

The resulting band gaps for different sample positions are shown in Figure B-2d. One can clearly observe an apparent band gap widening on the Menzel glass substrate as one moves towards lower thicknesses and higher pressure–distance products, approaching the Menzel glass band gap of 3.8 eV. The f-SiO_2 substrate band gaps reveal that these observations are due to the Menzel glass substrate itself and that film band gaps are in fact hardly widened by increasing pressure–distance products. The similar band gaps obtained for both substrates for greater thicknesses and lower pressure–distance products are due to high film absorptance for these sample positions, yielding substrate absorptances insignificant.

Regarding thin, high-pressure, or wide-band-gap films on Menzel glass or comparable soda lime glass substrates, caution must be taken in band gap determination using the Tauc plot method.

Appendix C Photon flux effect

An issue concerning the comparison of multiple UV photodarkening experiments is the effect of irradiation intensities. Beside a variety of available light sources of different spectra and intensities, the positioning of lamps also affects the irradiance. Furthermore, lamp intensities tend to degrade during use and exact reproducibility of irradiation experiments is therefore problematic.

To establish the effect of varying intensities on the photodarkening contrast of photochromic YO_xH_y, identical samples are subjected to UV illumination using the same UV light source but at varying distances from the lamp centre. The light source is single a Herolab MW–MW UV hand lamp as shown in Figure 3.16. The incident spectral photon fluxes at five different lamp distances are given in Figure C-1a, and the corresponding absolute photon fluxes as a function of lamp distance in Figure C-1b.

Three identical 91(12) nm-thick YO_xH_y samples are grown at a pressure of 0.51 Pa and separately illuminated at distances of 4.5 cm, 7.0 cm, and 9.5 cm from the light source, corresponding to absolute incident photon fluxes Φ_p of $5.9 \times 10^{15}/\mathrm{cm}^2/\mathrm{s}$, $3.5 \times 10^{15}/\mathrm{cm}^2/\mathrm{s}$, and $2.3 \times 10^{15}/\mathrm{cm}^2/\mathrm{s}$, respectively. The resulting normalised transmittances $\bar{T}(t)/\bar{T}_0$ averaged over 450–1000 nm wavelengths as a function of illumination time are depicted in Figure C-2a. Larger photon fluxes obviously lead to enhanced darkening. Although the darkening process is slowed down for longer illumination times, there is no sign of saturation for either of the samples and irradiation is ceased after four or five hours. To quantify the darkening potential for the samples the normalised contrast $\Delta\bar{T}/\bar{T}_0$

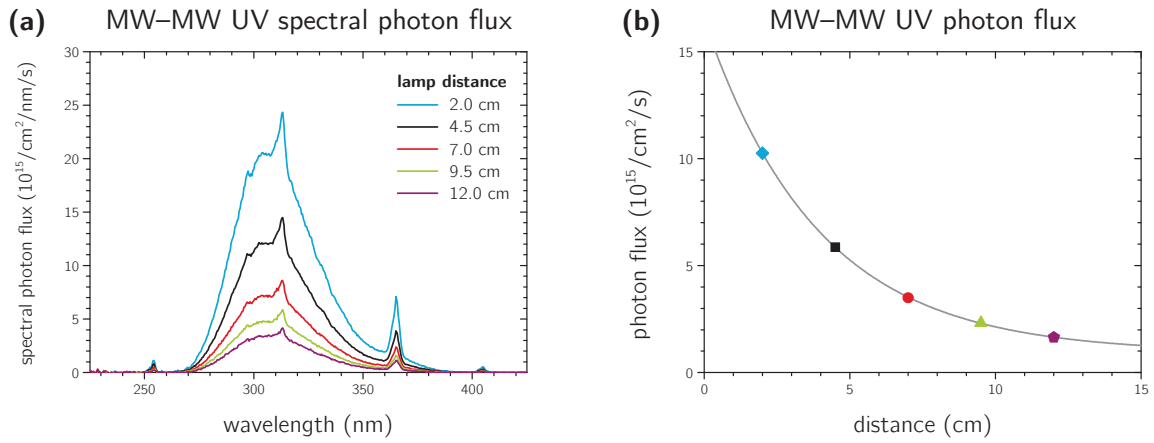

Figure C-1. (a) Spectral photon fluxes $\Phi_p(\lambda)$ at varying distances from a MW–MW UV light source (Figure 3.16), and **(b)** resulting absolute photon fluxes Φ_p.

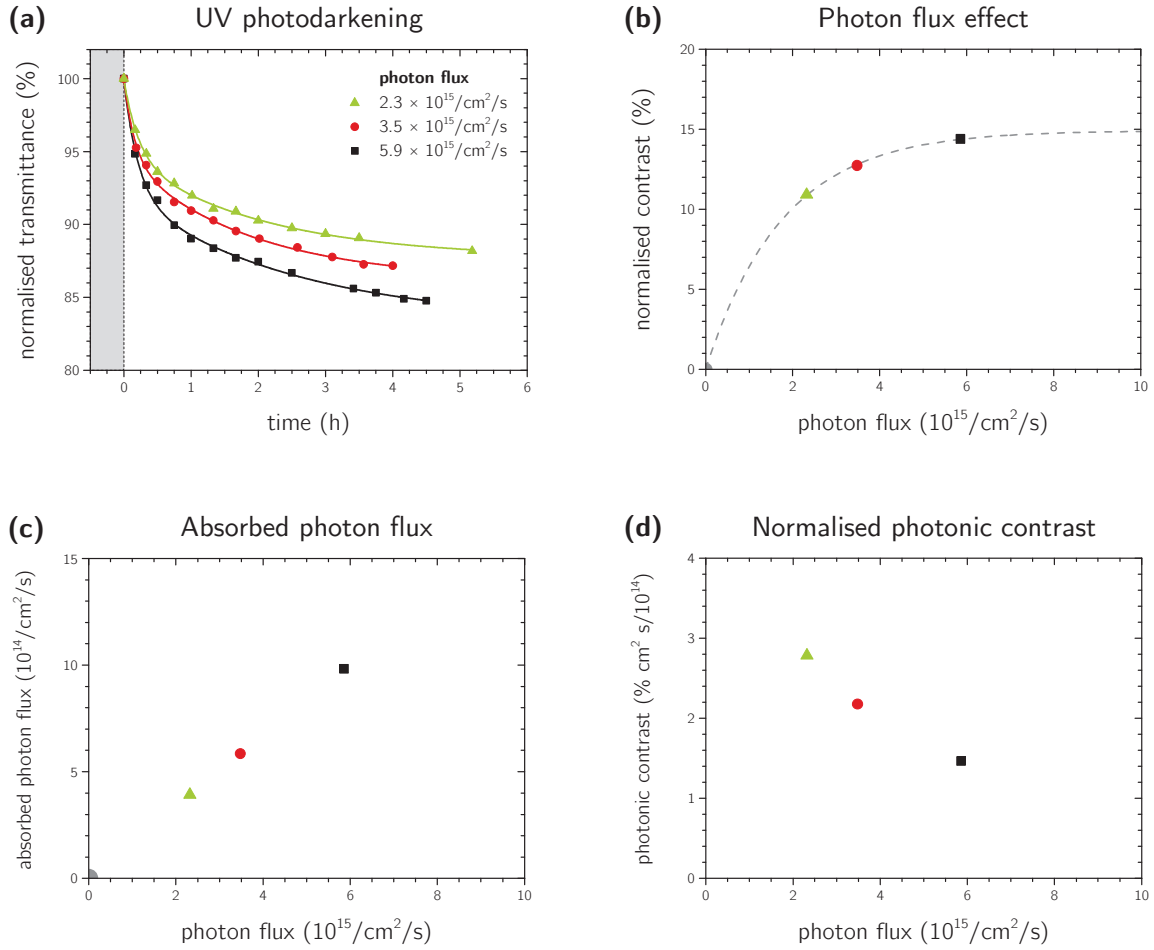

Figure C-2. (a) Normalised transmittances $\bar{T}(t)/\bar{T}_0$ of three identical 91 nm-thick YO_xH_y films subjected to varying UV intensities I and photon fluxes Φ_p, **(b)** the normalised contrasts $\Delta\bar{T}/\bar{T}_0$ after 3.5 h of illumination, **(c)** absorbed photons fluxes Φ_p^{abs} of the darekend films as a function of incident photon flux, and **(d)** the normalised photonic contrasts $\Delta\bar{T}/\Phi_p^{abs}\bar{T}_0$.

after 3.5 hours of UV illumination is computed and shown in Figure C-2b. A normalised contrast of zero is added to the graph for zero photon flux as no illumination does not lead to any darkening. An increasing contrast trend with photon flux is observed, increasing fast for small photon fluxes and levelling off towards larger fluxes.

The latter observation of stabilising contrasts for large photon fluxes can be explained qualitatively by the absorbed photon fluxes $\Phi_p^{abs} = \int \Phi_p(\lambda)A(\lambda)d\lambda$ of the darkened films shown in Figure C-2c. As UV absorption is identical for darkened and bleached YO_xH_y, Φ_p^{abs} is linearly related to the incident photon flux Φ_p and independent of the state of the films. For small fluxes, increasing the photon flux results in enhanced photodarkening as more UV photons are involved in the darkening process. The larger the contrast, however, the more material is susceptible to bleaching, and for larger photon fluxes the

bleaching reaction is therefore also enhanced. Moreover, as a larger fraction of the material is darkened, a larger fraction of incident photons is "wasted" on absorption by darkened material and hence does not contribute to further darkening. As a result, the photonic contrast $\Delta\bar{T}/\Phi_{\mathrm{p}}^{\mathrm{abs}}\bar{T}_0$, i.e. the contrast per instantaneously absorbed photon per unit area, diminishes for increasing photon fluxes, as shown in Figure C-2d. At some point a balance between additional darkening and bleaching is obtained, and further enlargement of the photon flux does not result in higher contrasts. This might be due to depletion of 'darkenable' species, limits to darkened domain sizes, or both.